The Telecommunications and Data Acquisition Progress Report 42-89

January–March 1987

E. C. Posner
Editor

May 15, 1987

NASA

National Aeronautics and
Space Administration

Jet Propulsion Laboratory
California Institute of Technology
Pasadena, California

The Telecommunications and Data Acquisition Progress Report 42-89

January–March 1987

E. C. Posner
Editor

May 15, 1987

NASA

National Aeronautics and
Space Administration

Jet Propulsion Laboratory
California Institute of Technology
Pasadena, California

Preface

This quarterly publication provides archival reports on developments in programs managed by JPL's Office of Telecommunications and Data Acquisition (TDA). In space communications, radio navigation, radio science, and ground-based radio astronomy, it reports on activities of the Deep Space Network (DSN) and its associated Ground Communications Facility (GCF) in planning, in supporting research and technology, in implementation, and in operations. Also included is TDA-funded activity at JPL on data and information systems and reimbursable DSN work performed for other space agencies through NASA. The preceding work is all performed for NASA's Office of Space Tracking and Data Systems (OSTDS).

In geodynamics, the publication reports on the application of radio interferometry at microwave frequencies for geodynamic measurements. In the search for extraterrestrial intelligence (SETI), it reports on implementation and operations for searching the microwave spectrum. The latter two programs are performed for NASA's Office of Space Science and Applications (OSSA).

Finally, tasks funded under the JPL Director's Discretionary Fund and the Caltech President's Fund which involve the TDA Office are included.

This and each succeeding issue of the TDA Progress Report will present material in some, but not necessarily all, of the following categories:

OSTDS Tasks:

    DSN Advanced Systems
        Tracking and Ground-Based Navigation
        Communications, Spacecraft-Ground
        Station Control and System Technology
        Network Data Processing and Productivity
    DSN Systems Implementation
        Capabilities for Existing Projects
        Capabilities for New Projects
        New Initiatives
        Network Upgrade and Sustaining
    DSN Operations
        Network Operations and Operations Support
        Mission Interface and Support
        TDA Program Management and Analysis
    GCF Implementation and Operations
    Data and Information Systems

OSSA Tasks:

    Search for Extraterrestrial Intelligence
    Geodynamics
        Geodetic Instrument Development
        Geodynamic Science

Discretionary Funded Tasks

Contents

OSTDS TASKS
DSN Advanced Systems
TRACKING AND GROUND-BASED NAVIGATION

COMMUNICATIONS, SPACECRAFT-GROUND

STATION CONTROL AND SYSTEM TECHNOLOGY

DSN Systems Implementation
CAPABILITIES FOR NEW PROJECTS

PRECEDING PAGE BLANK NOT FILMED

DISCRETIONARY FUNDED TASKS

B. D. Metscher
NASA Code 404-00-73-03-64

DSS 13 Frequency Stability Tests

T. Y. Otoshi and M. M. Franco

Radio Frequency and Microwave Subsystems Section

In a previous article, the results of frequency stability tests at DSS 13 were presented in table form for τ = 1000 s for the test period May 1985 through March 1986. This article is a continuation of that initial report and presents specially selected Allan sigma (square root of variance) plots of each of the subsystem test configurations previously reported. An additional result obtained from tests performed during July 1986 has been included in this article for completeness. The Allan sigma plots are useful in that frequency stability information is not only given for τ = 1000 s, but for τ values in the regions of 1 s, 10 s, 100 s, 500 s, and 2000 s as well.

I. Introduction

In a previous article [1] the frequency stability test results for the X-band uplink and X-band downlink system of the R&D system at DSS 13 were reported. Figures 1 and 2 show the system that was tested and also the test output ports. The results for τ = 1000 s were tabulated for various subsystems as well as end-to-end system configurations. The problem of presenting results only for τ = 1000 s is that erroneous conclusions might be drawn concerning the frequency stability of the system being tested. To ensure that the system is functioning properly, it is necessary to examine the test data at small values of τ as well as at the larger values. Therefore, it is the purpose of this article to present Allan sigma plots for the subsystems and end-to-end system test configurations that were previously reported upon. Allan sigma plots give information not only for τ = 1000 s, but also for τ values at 1 s, 10 s, 100 s, 1000 s, and higher (depending on the duration of the test).

The Allan sigma plots were obtained through the use of a computer program written for the Univac 1100 computer by C. Greenhall. An excellent discussion of the Allan Variance theory and the beat frequency measurement technique, as well as the data reduction equations for this computer program, are given by Greenhall in [2]. A possible departure from Greenhall's terminology used in [2] is the term "Allan sigma," which will be used in this article. To be consistent with Greenhall's definition, the Allan sigma plots might have been called Allan deviation plots. More appropriately, these plots might be referred to as fractional frequency stability plots. In as much as the plots from Greenhall's computer program are labeled "sigma" for Y-axis values, these plots will be referred to as Allan sigma plots for purposes of this article. The terms Allan sigma, Allan deviation, and fractional frequency stability have been used interchangeably in various reports by the authors. It is not the intent to confuse the reader, and we hope terminology for frequency stability measurements will be standardized in the near future.

For the purpose of making this article concise without sacrificing the transfer of knowledge or information, many symbols and abbreviations will be employed throughout in the main text, figures, and tables. These symbols and abbreviations are defined in the Appendix A. It is the intention of the authors to use symbols that are logical and self-defining.

II. Test Configurations and Test Results

A discussion and description of the instrumentation and test procedures for the different configurations previously tested were given in [1]. Except for the EEOLS configuration test procedure, which was not correctly described in [1], descriptions of test setups and test procedures will be omitted in this article. The current article should be considered as a supplement to the earlier article and thus only the Allan sigma plots for each of the different configurations tested at DSS 13 are presented. The Allan sigma plot presented here for each configuration is intentionally selected to be the best of all of the plots for each configuration. However, with the exceptions of the XLTRX, MMRX, XLTRS, and MMRS test configurations, the selected best plots are nearly representative of the typical result obtained most frequently for the particular test configuration. It should be mentioned that most of the tests were performed during the coolest part of the day or whenever the outside air temperature did not vary greatly. The temperature variations during the tests are shown on the Allan sigma plots. It is not known how much degradation would have occurred had the tests been conducted under less favorable weather conditions.

Figures 3 through 6 are Allan sigma plots for test configurations involving only the X-band uplink frequencies. Figures 7 through 10 are for test configurations involving only DSN X-band uplink and DSN X-band downlink frequencies, and Figs. 11 through 14 are for test configurations involving only X-band uplink and S-band downlink frequencies.

In the following presentation of test results, the nomenclature and symbols defined in Appendix A will be used extensively. The results that one should look for in an Allan sigma plot are (1) the σ value at $\tau = 1$ s, (2) linearity as a function of τ up to about $\tau = 500$ s, and (3) the value of σ at about $\tau = 1000$ s. For regions of $\tau > 3000$ s, the curve may continue in a downward trend or it may begin to rise depending upon long-term drifts [2]. Observe to see that there are no humps or sudden jumps in the curve between 1 s and 500 s. Any humps or jumps in the curve below about $\tau = 500$ s may indicate subsystem problems.

The value of σ at $\tau = 1000$ s is of most interest to Radio Science experimenters for the Gravity Wave Detection Experiment [3]. Therefore, for quick reference purposes, the σ values at $\tau = 1000$ s for each of the test configuration results shown in the Allan sigma plots are tabulated in Tables 1 through 3. Any difference between the tabulated results and the interpolated values obtained from the plots at $\tau = 1000$ s can be explained by the fact that for the plots, the computed data points do not lie exactly at $\tau = 1000$ s, while the results

for Tables 1 through 3 were computed exactly at $\tau = 1000$ s through the use of a separate computer program.

Figures 3 and 4 show Allan sigma plots for tests made on EXCCL configurations using two-mixer and one-mixer methods, respectively. The X-band uplink frequency for test results in Figs. 3 and 4, respectively, were 7166.9 and 7200 MHz. The output test port for both results was port 4 (shown in Fig. 1). Note that the Dana synthesizer, $\times 16$ multiplier, 36.6 m (1,200 ft) of uncompensated cable, as well 36.6 m of phase-stabilized cable carrying 100 MHz from the control room into the cone are all part of the EXCCL configuration being tested. The two-mixer method was described previously in [1] and is a new method developed to enable tests to be made at test frequencies that are not integer multiples of 100 MHz. The one-mixer method is the more familiar method that is used to make tests when the test frequency is an integer multiple of 100 MHz. This one-mixer method does not require an additional frequency synthesizer and mixer as part of the test setup as does the two-mixer method, but is not as versatile.

Figures 5 and 6 are Allan sigma plots for tests made on the XMTCL and XMTOL configurations, respectively. In addition, XTIME and YFREQ plots are shown. These latter plots are useful for providing a measure of stability versus time. They are also helpful for diagnostic purposes and isolating bad data points. Sometimes the bad points can be related to non-typical station events. The output test port for the XMTCL and XMTOL configurations is port 5 (Fig. 1). Note that this test configuration includes the X-band transmitter as well as the EXCCL test configuration described previously. The X-band uplink frequency for both test configurations was 7200 MHz.

Figure 7 is an Allan sigma plot for tests made on the XLTRX configuration. The test output port for this configuration was port 6 (Fig. 1). Note that the exciter subsystem and the X-band UL to X-band DL frequency translator are parts of the system being tested. In order to minimize excessive use of the X-band transmitter for some types of subsystem testing, the X-band transmitter was intentionally bypassed and not included in the test configuration for this particular test result. The X-band uplink and X-band downlink frequencies for this test were 7162.3 MHz and 8415.0 MHz, respectively.

Figure 8 is an Allan sigma plot for tests made on the MMRX configuration where the output port is port 7 (Fig. 1). The X-band uplink and X-band downlink frequencies for this test were 7162.3 MHz and 8415.0 MHz, respectively. The subsystems included in the test configuration are the exciter subsystem, X-band UL to X-band DL frequency translator,

X-band maser, X-band MMR, and the 36.6 m (1,200 ft) of cable carrying the 315-MHz IF signal back to the control room. The X-band transmitter was not included in the test configuration for this particular test result. The results for the MMRX test were much better than expected.

Figure 9 is an Allan sigma plot for the EECLX configuration where the output test port is the 1-MHz doppler extractor port 8 (Fig. 1). The X-band uplink and X-band downlink frequencies for this test were 7177.92 MHz and 8433.33 MHz, respectively. The subsystems included in the test configuration are the exciter subsystem, X-band transmitter (in closed-loop mode), X-band UL to X-band DL frequency translator, X-band maser, X-band MMR, 36.6 m of 315-MHz IF cable, X-band system upconverter/downconverter, Block III closed loop receiver, and 1-MHz doppler extractor. In addition, XTIME and YFREQ plots are shown in Fig. 9. These plots are useful for studies of how the stability varied with time during the testing. As discussed in [1], the EECLX results may not be valid due to suspected leakage signals in the closed-loop configuration. These leakage signals were discovered after testing was completed. They cannot be eliminated without major redesign of the receiving system. The results are presented here for reference and future comparison purposes only.

Figure 10 is an Allan sigma plot for end-to-end system tests made on the EEOLX configuration, where the output test port is the phase detector (mixer) output port 11 (Fig. 1). The X-band uplink and X-band downlink frequencies for this test were 7166.94 MHz and 8420.43 MHz, respectively. The subsystems included in the test configuration are the exciter subsystem, X-band transmitter (in closed-loop mode), X-band UL to X-band DL frequency translator, X-band maser, X-band MMR, 36.6 m of IF cable, X-band system upconverter/downconverter, and Block III receiver operating in a modified open-loop configuration.

Figure 10 also shows XTIME and YFREQ plots, which are useful for studies of how the stability varied with time during the testing. The test results are excellent and indicate that end-to-end system stabilities of better than 2.0 E-15 can be achieved for τ = 1000 s. It should be pointed out, as was pointed out in [1], that the results do not include the stability of the H-maser frequency source, and do not include antenna effects above the transmitter coupler output port. For this test result, as for all results in this article, the antenna was stationary at the zenith position.

Figure 11 is an Allan sigma plot for the XLTRS test configuration where the output test port is port 12 (Fig. 2). The X-band uplink and S-band downlink frequencies for this test were 7162.3 MHz and 2295 MHz, respectively. Normally included in this test configuration are the exciter subsystem,

X-band transmitter, and the X-band UL to S-band DL frequency translator. However, the X-band transmitter was not included in this configuration due to a desire to not overuse the X-band transmitter unnecessarily for some types of subsystem testing.

Figure 12 is an Allan sigma plot for the MMRS test configuration where the output test port is port 13 (Fig. 2). The X-band uplink and S-band downlink frequencies for this test were 7162.3 MHz and 2295 MHz, respectively. The subsystems normally included in the test configuration are the exciter subsystem, X-band transmitter, X-band UL to S-band DL frequency translator, S-band maser, S-band MMR, and 36.6 m (1,200 ft) of cable carrying the 295-MHz IF signal back to the control room. The X-band transmitter was not included in the particular tests performed on this configuration.

Figure 13 gives Allan sigma, XTIME, and YFREQ frequency stability plotted results for the EECLS test configuration, where the output test port is the 1-MHz doppler extractor port 14 (Fig. 2). The X-band uplink and S-band downlink frequencies for this test were 7180.0 MHz and 2300.7 MHz, respectively. The subsystems included in the test configuration are the exciter subsystem, X-band transmitter (in closed-loop mode), X-band UL to S-band DL frequency translator, S-band maser, S-band MMR, 36.6 m of 295-MHz IF cable, S-band system upconverter/downconverter, Block III closed-loop receiver, and 1-MHz doppler extractor. As discussed in [1], the EECLS results might not be valid due to suspected leakage signals in the closed-loop configuration. The results are presented here for reference and future comparison purposes only.

Figure 14 gives Allan sigma, XTIME, and YFREQ frequency stability plotted results for EEOLS test configuration where the output test port is the 10-MHz port 16 (Fig. 2). The results at this test port were obtained by mixing the 10 MHz output signal with 10 MHz plus 1 Hz signal from an HP8662A synthesizer that was driven by a reference frequency from the H-maser frequency distribution system. It would have been simpler to test this EEOLS configuration at port 17 (Fig. 2) rather than at port 16. The X-band uplink and S-band downlink frequencies for this test were 7162.3 MHz and 2295 MHz, respectively. The subsystems included in the test configuration are the exciter, X-band transmitter (in closed-loop mode), X-band UL to S-band DL frequency translator, S-band maser, S-band MMR, 36.6 m of 295-MHz IF cable, S-band system up converter/down converter, and Block III receiver operating in a modified open-loop configuration. The results for this test configuration were not as good as expected, but are inconclusive. It is not known whether the S-band maser or the Block III receiver synthesizer was operating properly at the time. Further testing was not performed on this configu-

ration at the time because the interest was primarily in obtaining test data for the X-band downlink configurations. More tests for this configuration need to be made in the future.

III. Concluding Remarks

The conclusions applicable for this article are the same as those given in the previous report [1]. The purpose of this article was to present Allan sigma plots for each of the test configurations whose results were reported previously. The results presented were intentionally selected to be the best of each test configuration. With the exception of the XLTRX, MMRX, XLTRS, and MMRS test configurations, the plots presented were also typical of the results obtained most frequently during the test period from March 1985 through July 1986 at DSS 13 as well as previous test periods, where results were reported on internal JPL reports.

In addition to concluding remarks given in the previous article [1], it can be further stated that Allan sigma plots are useful and necessary for the evaluation of the performance of station stability. Obtaining a σ value only at $\tau = 1000$ s can sometimes lead to an erroneous conclusion that the system is performing well or badly.

It is recommended that as standard procedure, the total data set be saved on tape or diskette so that it can be post-processed for Allan sigma, XTIME, and YFREQ plots with the aid of a computer program similar to that developed by Greenhall. The XTIME and YFREQ plots are useful for study of the time history of station stability during the test period and also for diagnostic purposes. It is also recommended that for station stability tests, a log book be kept of unusual station events. If the bad data points can be correlated to non-typical unusual station events, the test data can be salvaged and edited. For this article, editing was done on the data set for two test configurations as noted in the tables. For the tests performed at DSS 13, the tests were performed with instrumentation [1] that provided real-time visual and audio indications whenever bad data points occurred during the test. This type of real-time bad-data-point warning system proved to be invaluable for station stability testing.

References

[1] T. Y. Otoshi, and M. M. Franco, "DSS 13 Frequency Stability Tests Performed During May 1985 through March 1986," *TDA Progress Report 42-86*, Vol. April–June 1986, pp. 1–14, Jet Propulsion Laboratory, Pasadena, Calif., August 15, 1986.

[2] C. G. Greenhall, "Frequency Stability Review," *TDA Progress Report 42-88*, Vol. October–December 1986, pp. 200–212, Jet Propulsion Laboratory, Pasadena, Calif., Feb. 15, 1987.

[3] A. L. Berman, "The Gravitational Wave Detection Experiment: Description and Anticipated Requirements," *TDA Progress Report 42-46*, Vol. April–June 1986, pp. 100–108, Jet Propulsion Laboratory, Pasadena, Calif., August 15, 1978.

Table 1. Summary of FFS values for τ = 1000 s only[a] for X-band uplink frequency

Test ID	Test Period	Test Port[b]	Test Description	FFS for τ = 1000 s	Comments
EXCCL	Feb. 86	4	Exc closed loop, 7166.94 MHz UL (Galileo Ch 18), two-mixer method, 4096 data pts.	2.51E-16 3 #SDP Test freq = 7166.94 MHz	Used two-mixer method. See Fig. 3 for corresponding Sigma vs Tau plot.
EXCCL	Feb. 86	4	Exc closed loop, 7200 MHz UL, one-mixer method, 11,008 data pts.	7.65E-16 10 #SDP Test freq = 7200 MHz	Used one-mixer method. See Fig. 4 for corresponding Sigma vs Tau plot.
XMTCL	May 85	5	X-band xmtr closed loop, 15 kW saturated, 7200 MHz UL, 4791 data pts.	1.76E-15 3 #SDP Test freq = 7200 MHz	Edited data set. Used only pts 1-4791 of the original data set. See Fig. 5 for corresponding Sigma vs Tau plot.
XMTOL	May 85	5	X-band xmtr open loop, 7200 MHz UL, 14,432 data pts.	1.42E-15 13 #SDP Test freq = 7200 MHz	Good result for open loop xmtr test. See Fig. 6 for corresponding Sigma vs Tau plot.

[a]Test results for other τ values are shown in Figs. 3-6.

[b]See Fig. 1 block diagram for this output signal test port location in the X-band uplink system.

Table 2. Summary of FFS values for $\tau = 1000$ s only[a] for X-band uplink and X-band downlink frequency

Test ID	Test Period	Test Port[b]	Test Description	FFS for τ = 1000 s	Comments
XLTRX	Dec. 85	6	Exciter, X-band xmtr bypassed, X-band xltr, 7162.3 MHz UL, 8415.0 MHz DL, two-mixer method, +3 dBm into second mixer, 14,368 data pts.	1.56E-15 13 #SDP Test freq = 8415 MHz	Note that xmtr not included. Used two-mixer method to get 8415 MHz test signal. Results are as good as 8400 MHz results reported elsewhere. See Fig. 7 for corresponding Sigma vs Tau plot.
MMRX	July 86	7	Exciter, X-band xmtr bypassed, X-band xltr, X-band maser, X-band MMR, 7162.31 MHz UL, 8415.00 MHz DL, 315 MHz IF in control room, 17,024 data pts.	2.90E-16 16 #SDP Test freq = 8415 MHz	Note that xmtr not included. Results better than expected. See Fig. 8 for corresponding Sigma vs Tau plot.
EECLX	Jan. 86	8	End-to-end test with xmtr (15 kW), 7177.92 MHz UL, 8433.33 MHz DL, 1 MHz doppler extractor port, 14,432 data pts.	5.93E-16 13 #SDP Test freq = 8433.33 MHz	This good result might not be valid due to leakage signals in closed loop rcvr. See Fig. 9 for the corresponding Sigma vs Tau plot.
EEOLX	Mar. 86	11	End-to-end test with 15 kW xmtr, 7166.94 MHz UL, 8420.43 MHz DL, modified open loop rcvr output port, 12,032 data pts.	9.51E-16 11 #SDP Test freq = 8420.43 MHz	Better than expected end-to-end system result. See Fig. 10 for corresponding Sigma vs Tau plot.

[a]Test results for other τ values are shown in Figs. 7–10.
[b]See Fig. 1 for this output signal test port location in the X-band uplink and X-band downlink system.

Table 3. Summary of FFS values for τ = 1000 s only[a] for X-band uplink and S-band downlink frequency

Test ID	Test Period	Test Port[b]	Test Description	FFS for τ = 1000 s	Comments
XLTRS	July 85	12	Exciter, X-band xmtr bypassed, S-band xltr, 7162.3 MHz UL, 2295.0 MHz DL, two-mixer method, 14,368 data pts.	2.05E-15 13 #SDP Test freq = 2295 MHz	Note that xmtr not included. Results are reasonable for S-band DL. See Fig. 11 for corresponding Sigma vs Tau plot.
MMRS	July 85	13	Exciter, X-band xmtr bypassed, S-band xltr, S-band maser, MMR, 7162.3 MHz UL, 2295.0 MHz DL, 295 MHz IF in control room, 8000 data pts.	1.02E-15 6 #SDP Test freq = 2295 MHz	Xmtr not included. Edited data set. Used pts 8201-16200 only of original data set. See Fig. 12 for corresponding Sigma vs Tau plot.
EECLS	Nov. 85	14	End-to-end system without xmtr, 7180.0 MHz UL, 2300.7 MHz DL, rcvr closed loop, 1 MHz doppler extractor output, 15,104 data pts.	4.60E-15 14 #SDP Test freq = 2300.7 MHz	These good results might not be valid due to suspected leakage signals in the closed loop rvcr system. See Fig. 13 for corresponding Sigma vs Tau plot.
EEOLS	Nov. 85	16	End-to-end system without xmtr, 7162.3 MHz UL, 2295.0 MHz DL, rcvr in modified open loop, 10 MHz output port, 9472 data pts.	1.52 E-14 8 #SDP Test freq = 2295 MHz	Results not as good as expected for S-band DL freq. See Fig. 14 for corresponding Sigma vs Tau plot.

[a]Test results for other τ values are shown in Figs. 11-14.
[b]See Fig. 2 for this output signal test port location in the X-band uplink and S-band downlink system.

Fig. 1. Output test ports for frequency stability testing on X-band uplink and X-band downlink subsystems at DSS 13 (same as Fig. 1 of [1]). Example frequencies are for channel 14.

FOR OPEN-LOOP RECEIVER OPERATION, THE VCO IS AUTOMATICALLY SWITCHED OUT, AND THE MIXER AND ×50 ASSEMBLY ARE REPLACED BY A ×31.25 MULTIPLIER

NEW DESIGN

f_{XT} (7162.3125)   XPNDR

$f_{SR} = \frac{240}{749} f_{XT}$ (2295)

S-BAND COMBINER
X-BAND POLARIZER
X-BAND FEED

XLTRS (12)

MODIFIED BLK III RCR

X/S TEST SIG TRANSLATOR

X-TRANSMITTER

$f_{SR} = \frac{240}{749} f_{XT}$ (2295)

f_{XT} (7162.3125)

X CPLR   S CPLR

$\frac{509}{749} f_{XT}$ (4867.3125)   MIXER − f_{XT} (7162.3125)

DPLXR   TO X-BAND RCR   S-BAND DPLXR f_{SR}

XMTR P.A.   FROM S-BAND XMTR

LONG FB LOOP

f_{SR} (2295)

X/S DOPPLER EXTRACTOR

× 5 $\frac{8144}{749}$

SHORT FB LOOP

S-BAND TWM

÷ 5   MIXER +   × $\frac{13}{16}$ ϕ-DET AND ϕ-COMP

$\frac{509}{749} f_{XT}$ (4867.3125)

MIXER − f_{XT} (7162.3125)   × 16   MIXER +   × 65   MULTIMISSION RCVR

f_{SR} (2295)

MIXER −   (2000)   × 20   MIXER −

CS RECEIVER

ANTENNA

1200 ft

CONTROL ROOM   20   MMRS (13) f_{SR}-2000 (295)

f_{SR}-2000 (REF) (295)

DCO #1 (41.39453125)   CS XMTR   U.C./D.C.

MIXER − f_{SR}-2000 + 1050 (1345)   MIXER −

(1050)   X-EXCITER   × 50   1050

1 GHz   MIXER −   100 MHz REF   5 MHz REF   100 MHz REF   DCO #3 (47.90)   MIXER −   MIXER −   1 GHz

(50)   (26.90)   50

49/51   MIXER −   MIXER −   45 MHz   BLK III RCVR   21 MHz VCO   MIXER −   60 MHz

(14)   EECLS   (15)   49/ 5 10 45 51 60 1 GHz   EEOLS (16)

$\hat{1}$ MHz $\hat{5}$ MHz   LOOP FILTER   MIXER −   10 MHz

100 MHz H-MASER REF   REF FREQ'S DERIVED FROM H-MASER   EEOLS (17)

X/S DOPPLER MIXER

Fig. 2. Output test ports for frequency stability testing on X-band uplink and S-band downlink subsystems at DSS 13 (same as Fig. 2 of [1]). Example frequencies are for channel 14.
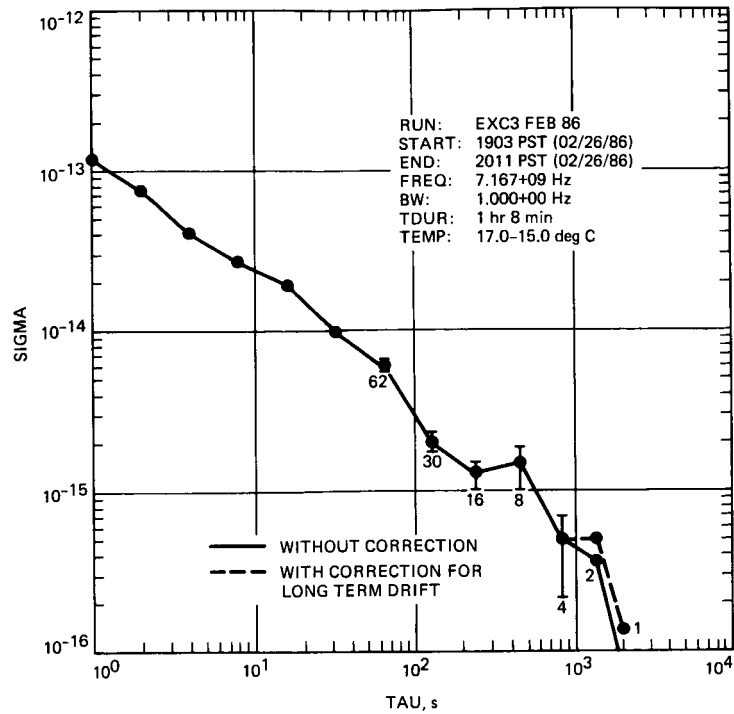
9

Fig. 3. Allan sigma plot for an exciter output test at port 4 (see Fig. 1) using a two-mixer method
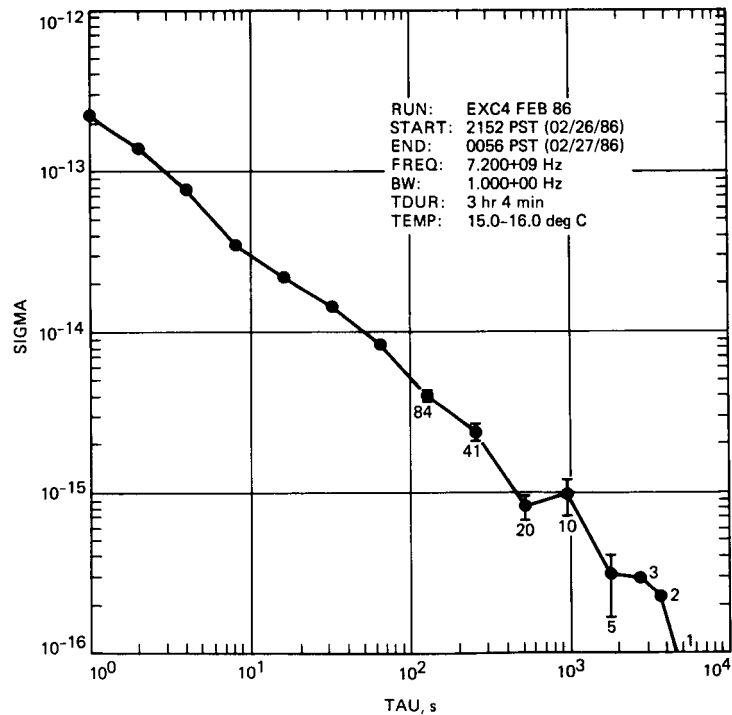

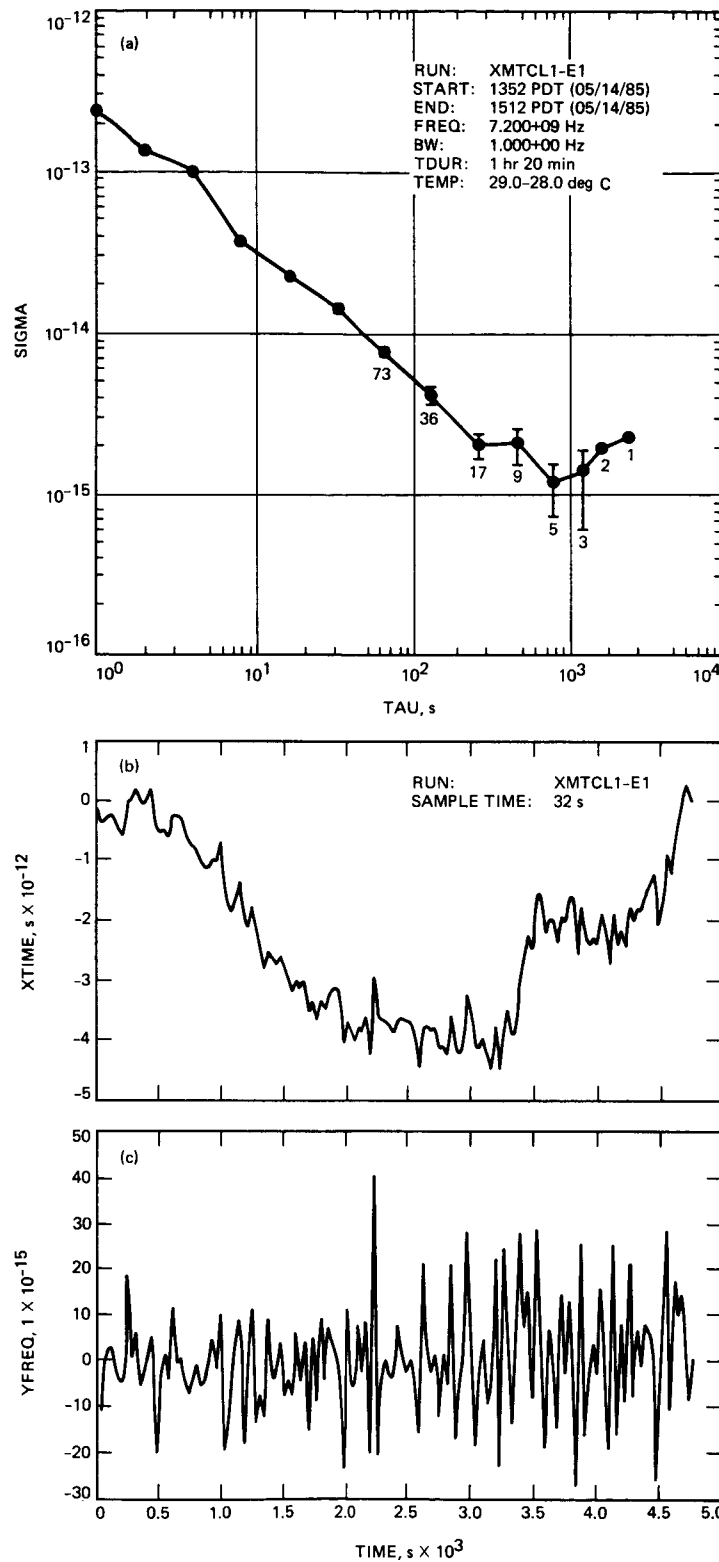**Fig. 4. Allan sigma plot for an exciter output test at port 4 (see Fig. 1) using a single mixer method**

Fig. 5. Frequency stability plots for an X-band transmitter closed loop output test at port 5 (see Fig. 1): (a) Allan sigma, (b) XTIME, and (c) YFREQ
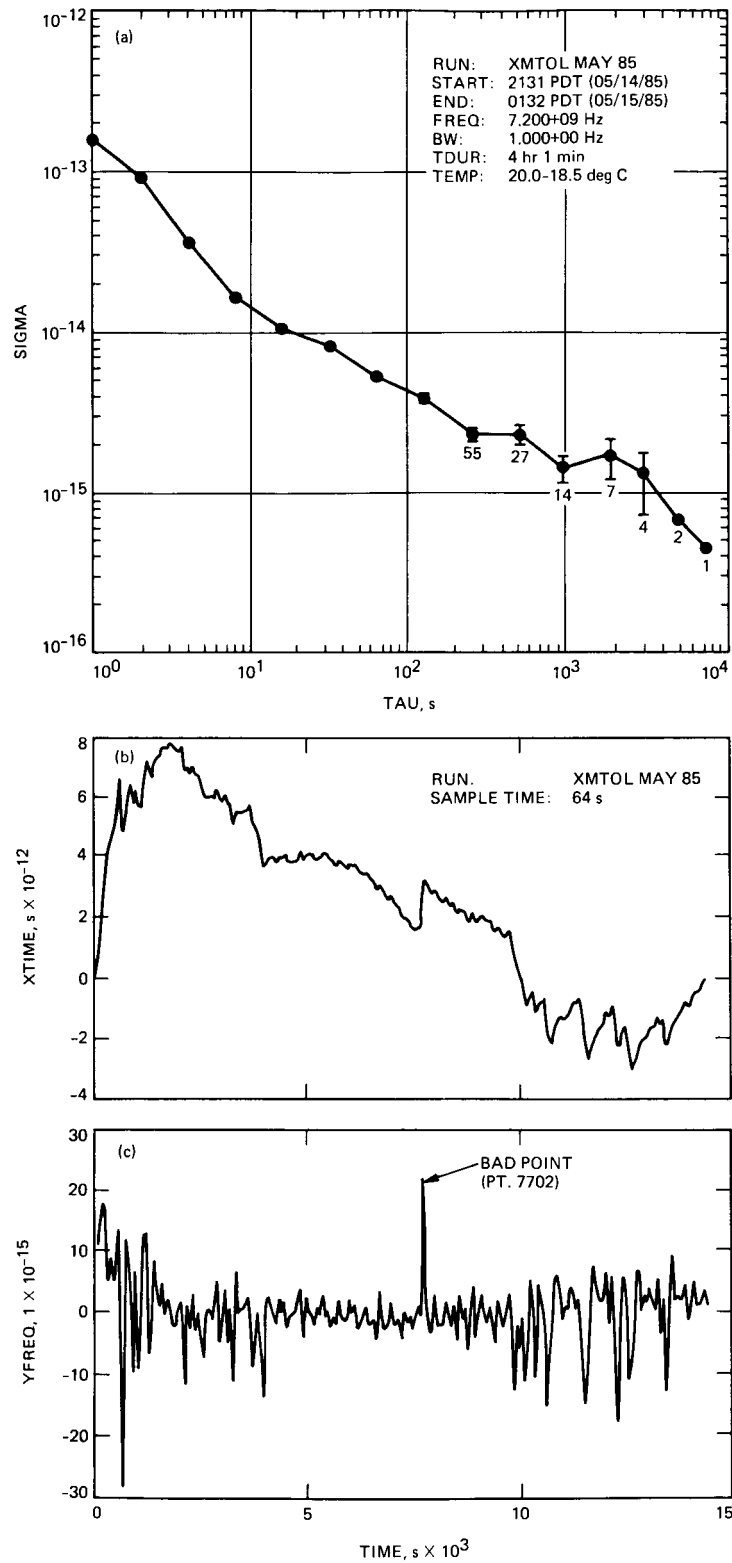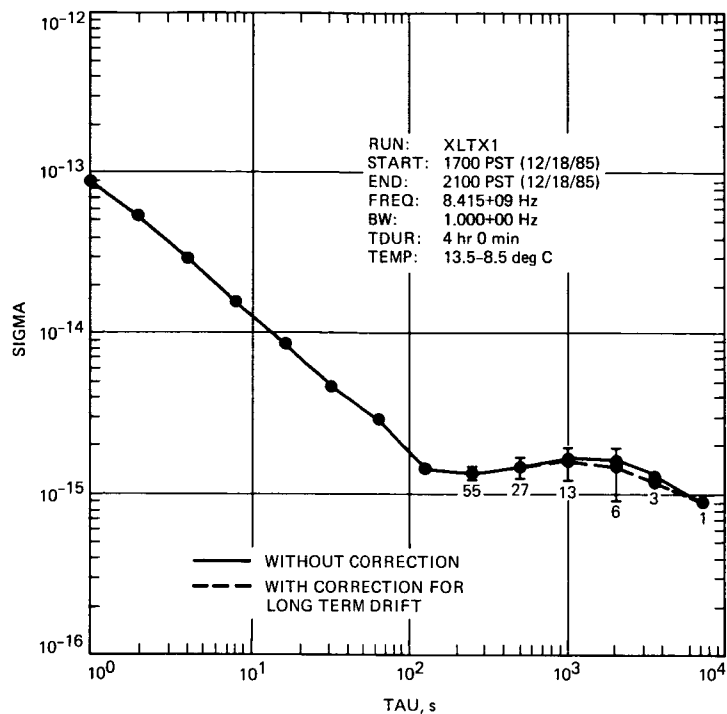
Fig. 6. Frequency stability plots for an X-band transmitter open loop output test at port 5 (see Fig. 1): (a) Allan sigma, (b) XTIME, and (c) YFREQ

Fig. 7. Allan sigma plot for an X-band translator output test at port 6 (see Fig. 1). The X-band transmitter was not included in the test configuration for this particular test result.
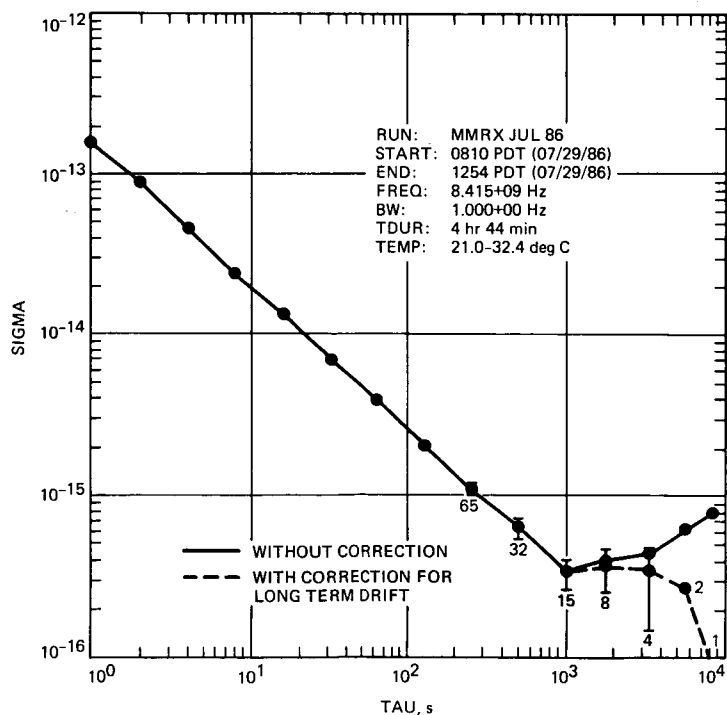

Fig. 8. Allan sigma plot for an X-band Multi-Mission Receiver (MMR) output test at port 7 (see Fig. 1). The X-band transmitter is not included in the test congfiguration for this particular test result.
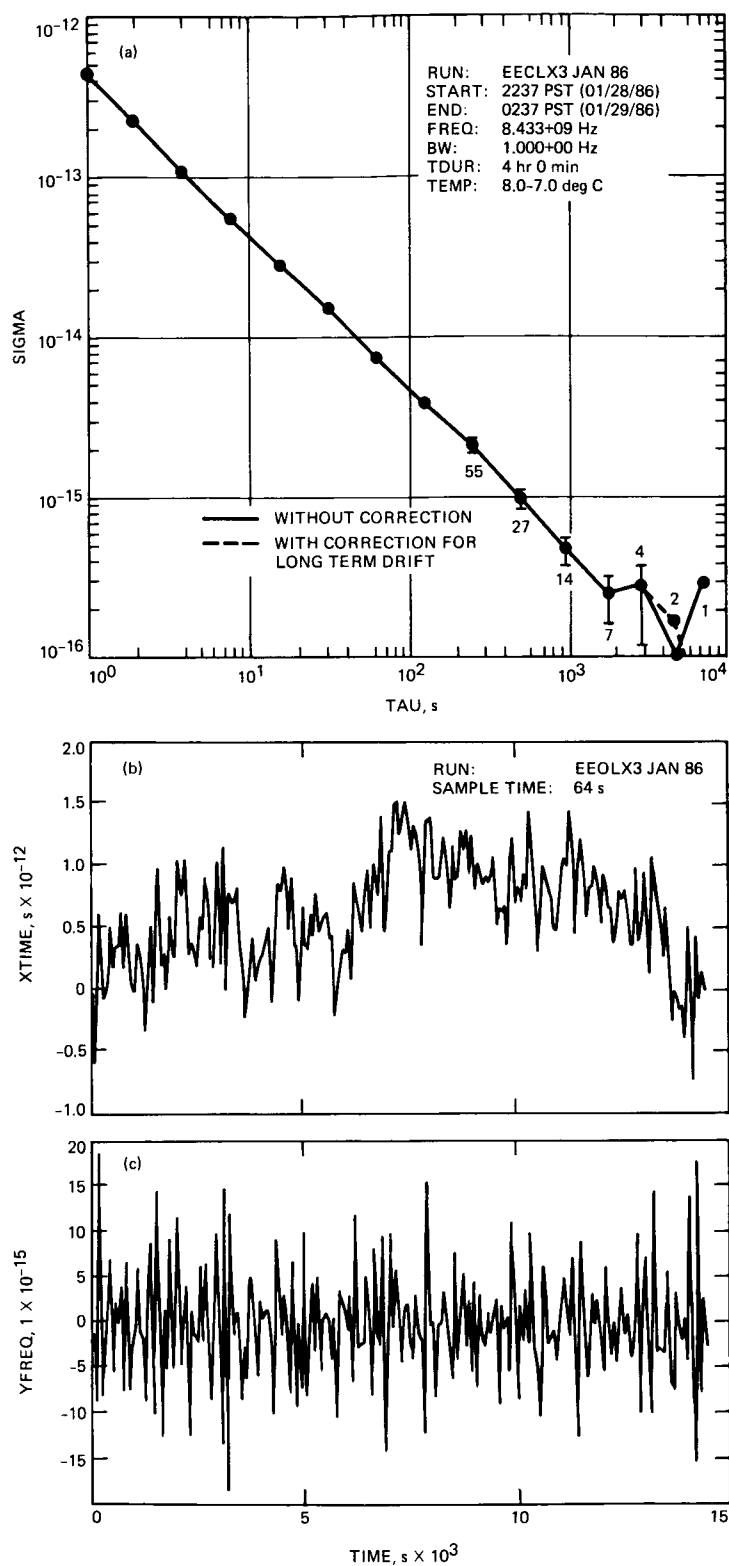
Fig. 9. Frequency stability plots for an end-to-end X-band uplink and X-band downlink system test with the receiver in closed loop configuration: (a) Allan sigma, (b) XTIME, and (c) YFREQ. The output port is the 1 MHz doppler extractor port 8 shown in Fig. 1.
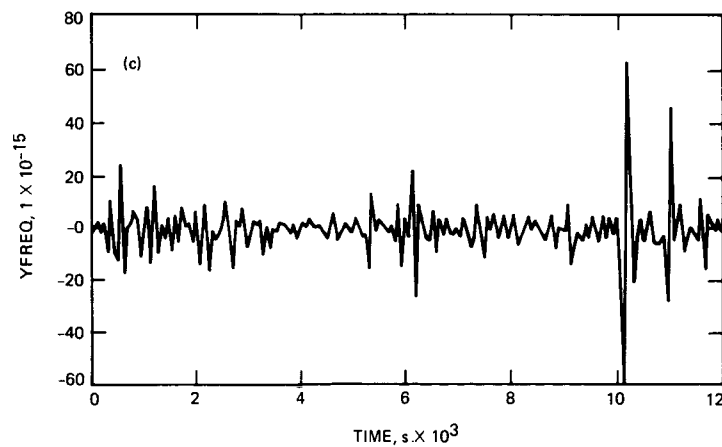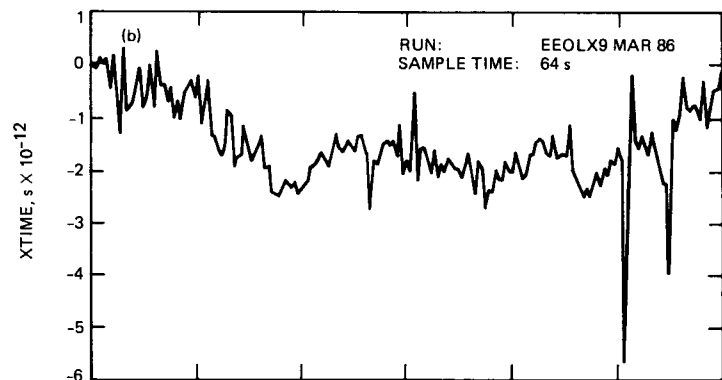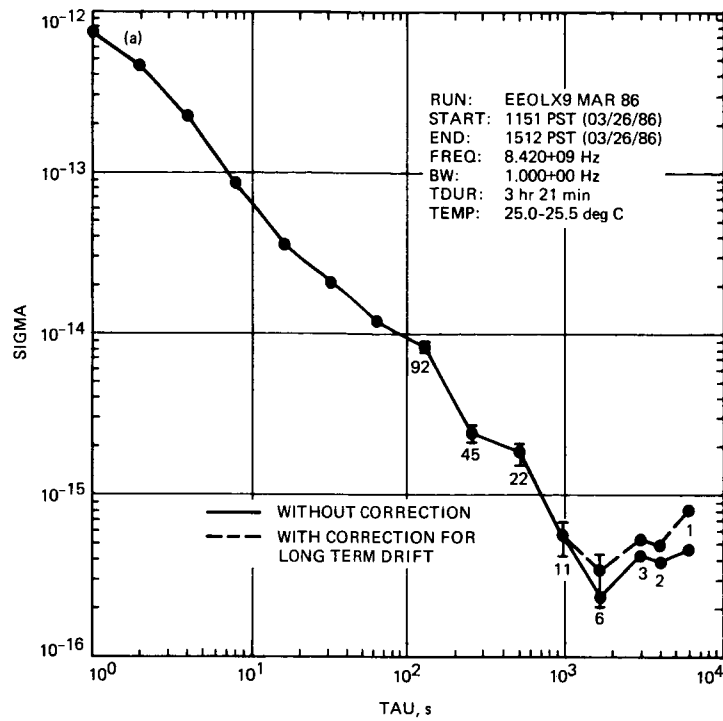
Fig. 10. Frequency stability plots for an end-to-end X-band uplink and X-band downlink system test with the receiver in a modified open loop configuration: (a) Allan sigma, (b) XTIME, and (c) YFREQ. The output port is the phase detector (mixer) output port 11 shown in Fig. 1.
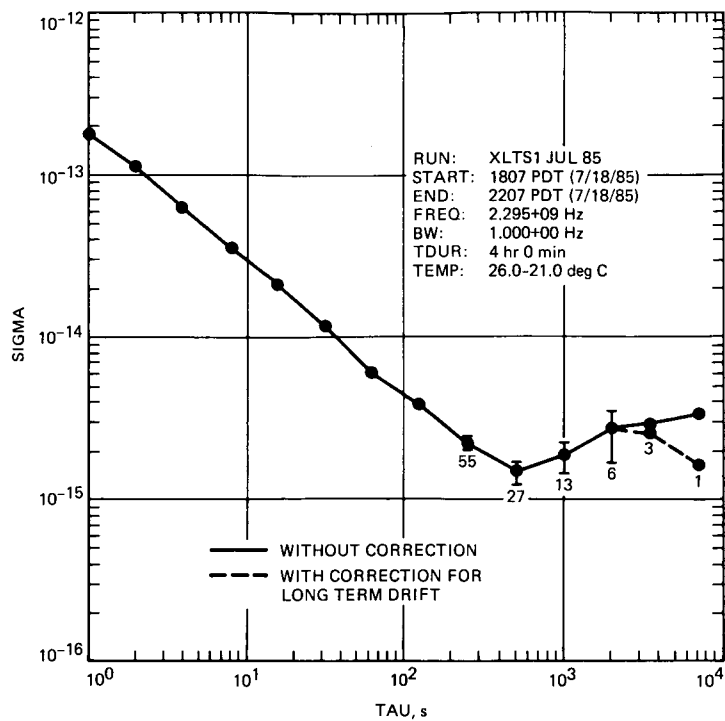
Fig. 11. Allan sigma plot for an S-band translator output test at port 12 (see Fig. 2). The X-band transmitter is not included in the test configuration.
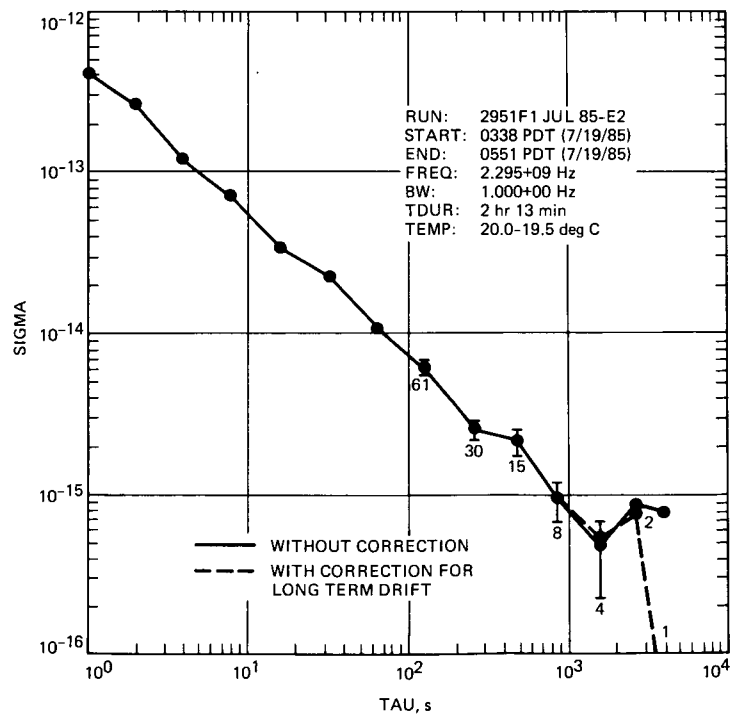

Fig. 12. Allan sigma plot for an S-band Multi-Mission Receiver (MMR) output test at port 13 (see Fig. 2).

Fig. 13. Frequency stability plots for an end-to-end X-band uplink and S-band downlink system test with the receiver in closed loop configuration: (a) Allan sigma, (b) XTIME, and (c) YFREQ. The output port is the 1 MHZ doppler extractor port 14 shown in Fig. 2.
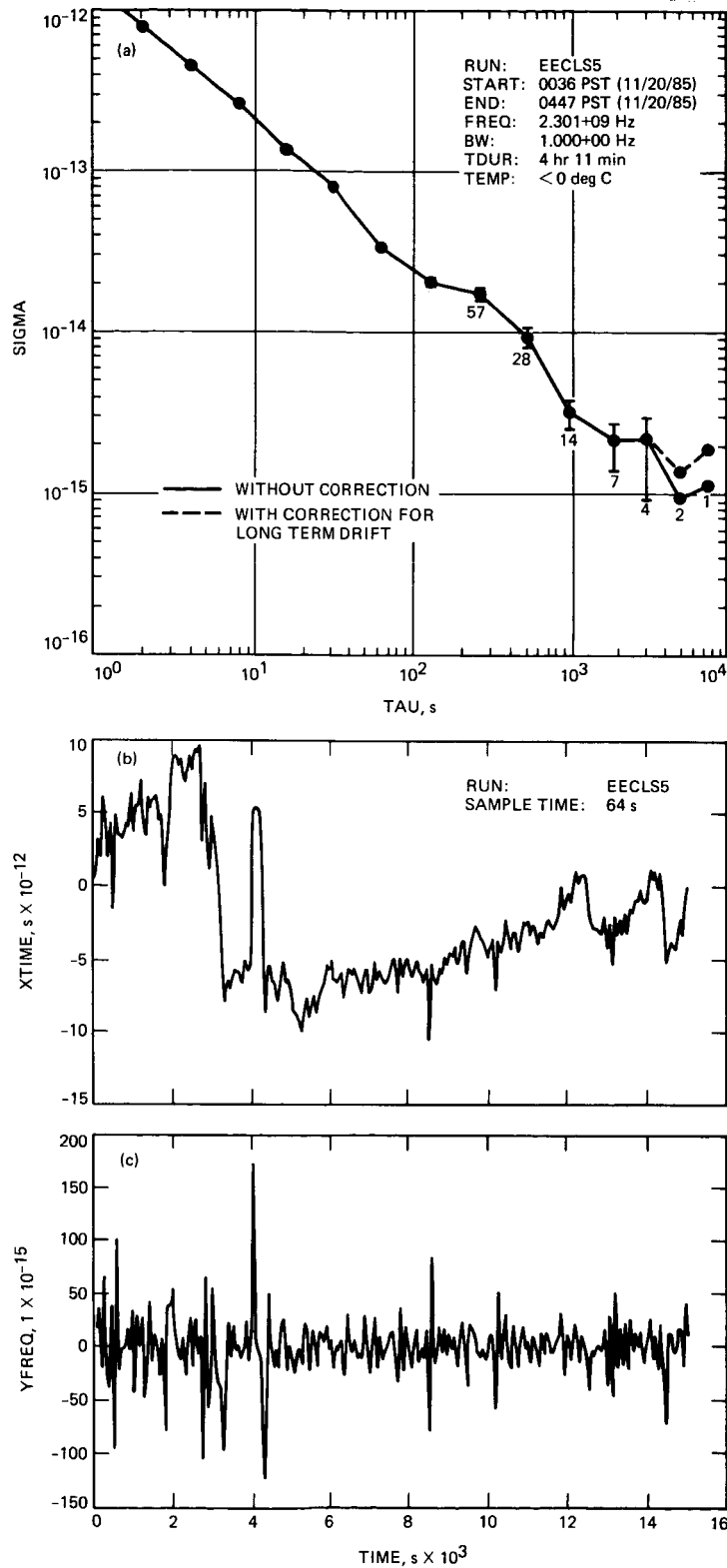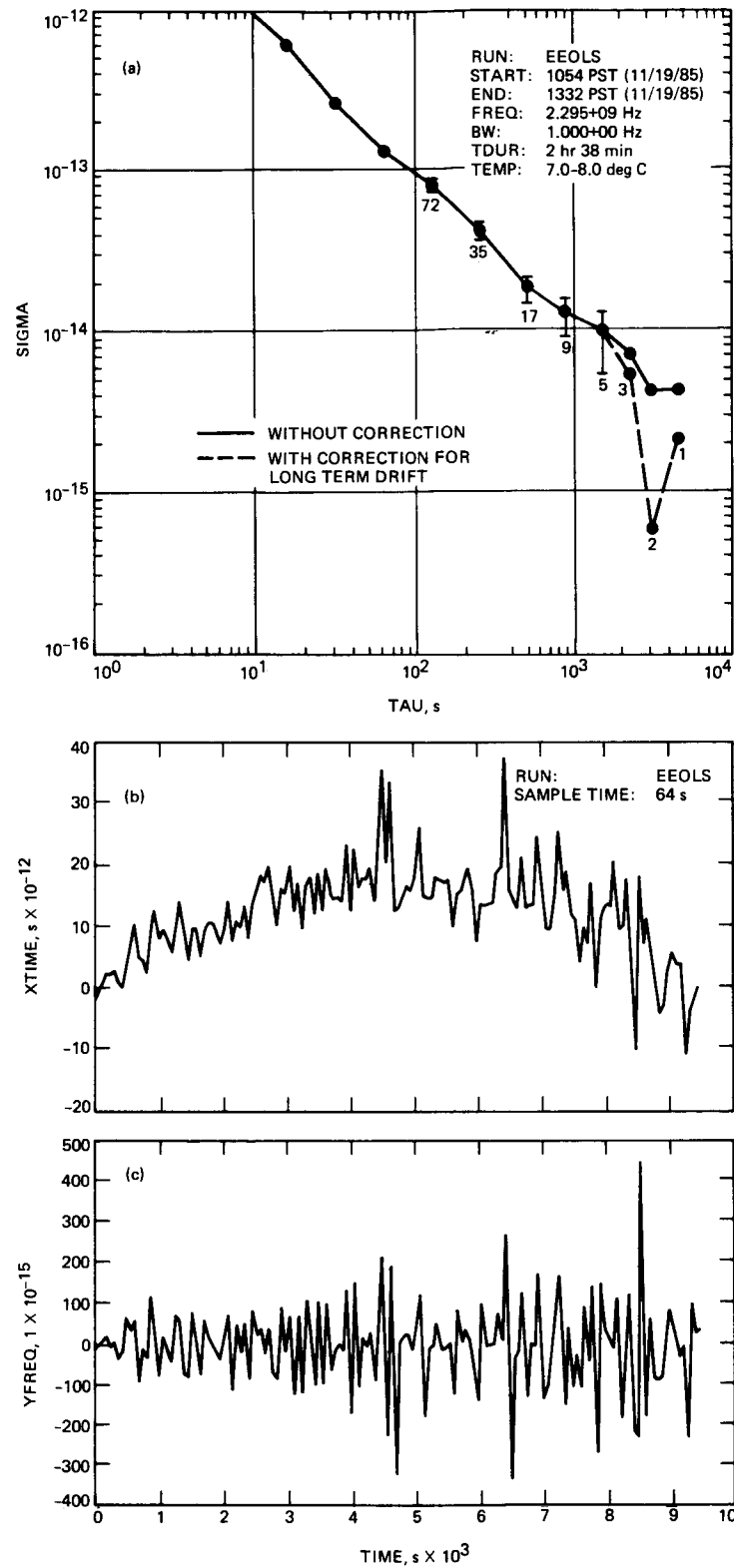
Fig. 14. Frequency stability plots for an end-to-end X-band uplink and S-band downlink system test with the receiver in a modified open loop configuration: (a) Allan sigma, (b) XTIME, and (c) YFREQ. The output port is the 10 MHz output port 16 shown in Fig. 2.

Appendix A

Nomenclature

Symbols that are used for description of test configurations are defined as follows:

EXCCL   Exciter output test configuration or chain for the exciter operating closed loop. The subsystems included in this configuration (or chain) are the transmitter synthesizer, X 16 multiplier, 36.6 m (1,200 ft) of uncompensated cable running from the synthesizer in the control room to the exciter subsystem in the cone, cable stabilized 100 MHz subsystem, and the exciter subsystem itself.

XMTCL   Transmitter output test configuration or chain when the X-band transmitter is operating closed loop. The subsystems included in this configuration consist of the buffer amplifier, klystron, feedback loop, and exciter chain described previously except with the exciter operating in open-loop mode.

XMTOL   Transmitter output test configuration when the X-band transmitter is operating open loop. The subsystems included in this configuration are the same as for the XMTCL configuration except that the exciter can be operating in either the closed-loop or open-loop mode. For all tests for this configuration, the exciter was intentionally operated in the closed-loop mode.

XLTRX   Translator X-band output test configuration for an X-band UL and X-band DL chain that consists of either the exciter or transmitter chain and the X-band UL to X-band DL frequency translator subsystem.

XLTRS   Translator S-band output test configuration for the X-band UL and S-band DL chain that consists of the exciter or transmitter chain and the X-band UL and S-band DL frequency translator.

MMRX   X-band Multi-Mission Receiver output test configuration for the X-band UL and X-band DL chain that now consists of either the transmitter or exciter chain, X-band UL to X-band DL frequency translator subsystem, X-band maser, and an R&D version X-band MMR receiver.

MMRS   S-band Multi-Mission Receiver output test configuration for the X-band UL and S-band DL chain that now consists of either the transmitter or exciter chain, X-band UL to S-band DL frequency translator subsystem, S-band maser, and an R&D version S-band MMR receiver.

EECLX   End-to-end system test configuration for X-band UL and X-band DL chain that includes the MMRX chain and Block III receiver #1 and doppler extractor subsystems. Block III receiver #1 is operating in a closed-loop mode.

EECLS   End-to-end system test configuration for X-band UL and S-band DL chain that includes the MMRS chain and Block III receiver #2 and doppler extractor subsystem. Block III receiver #2 is operating in a closed-loop mode.

EEOLX   End-to-end system test configuration for X-band UL and X-band DL chain that includes the MMRX chain and parts of the Block III receiver #1 subsystem. Block III receiver #1 is operating in a modified open-loop mode.

EEOLS   End-to-end system test configuration for X-band UL and S-band DL chain that includes the MMRS chain and parts of the Block III receiver #2 subsystem. Block III receiver #2 is operating in a modified open-loop mode.

Other abbreviations appearing in tables or figures are presented in alphabetical order and are defined as follows:

BW   Bandwidth

CS   Cable Stabilizer

DL   Downlink

EXC   Exciter

FFS   Fractional Frequency Stability or the Allan sigma (square root of the Allan variance of deviations, of observed frequencies from the test frequency, divided by the test frequency)

Freq   Frequency

#SDP   Number of second difference points used to compute the FFS

PDT   Pacific Daylight (Savings) Time

PST   Pacific Standard Time

Pts   Points

Rcvr   Receiver

Run   Test run or test data identification

Temp   Outside air temperature as measured at the cable bulkhead interface of the DSS 13 control room

Tdur   Test duration

UL   Uplink

Xltr   Translator

Xmtr   Transmitter

XTIME   Deviation of observed clock time from true clock time as determined from frequency stability measurements. It is calculated for a specified sampling time interval. It is plotted as a function of time relative to start of test time. See [2] for more details.

YFREQ   Average normalized frequency deviation for a specified sampling time interval. It is plotted as function of time relative to start of test time. See [2] for more details.

Spacecraft Mass Trade-Offs Versus Radio-Frequency Power and Antenna Size at 8 GHz and 32 GHz

C. E. Gilchriest

Telecommunications Systems Section

The purpose of this analysis is to help determine the relative merits of 32 GHz over 8 GHz for future deep space communications. This analysis is only a piece of the overall analysis and only considers the downlink communication mass, power, and size comparisons for 32 GHz and 8 GHz. Both parabolic antennas and flat-plate arrays are considered. The Mars Sample Return mission is considered in some detail as an example of the trade-offs involved; for this mission the mass, power, and size show a definite advantage of roughly 2:1 in using the 32 GHz over 8 GHz.

I. Introduction

The purpose of this analysis is to help determine the relative merits of 32 GHz over 8 GHz for future deep space communications. This analysis is only a piece of the overall analysis and only considers the downlink communication mass, power, and size comparisons for 32 GHz and 8 GHz.

A mission set is selected to demonstrate the 32 GHz versus 8 GHz relative merits. This set includes Saturn Orbiter Titan Probe (SOTP) and Mars Sample Return (MSR). While the following analysis applies to either (or any mission for that matter), it is tailored to the MSR where the size and mass of the antenna are important parameters because of the possible wind drag and vehicle upset, high center of gravity and vehicle upset, and compounding of the mass problems with cascaded vehicles. The launch-vehicle envelope with respect to the antenna size is another important parameter.

Certain improvements over 1985 performance levels are assumed for the ground stations for both 8 GHz and 32 GHz

and are discussed elsewhere [1]. Primarily these improvements are (1) array feed, (2) better subreflector, and (3) new surface panels set more precisely.

Analytical improvements in the combination of weather statistics with link performance uncertainties have been described by M. A. Koerner [2]. Both frequencies benefit from this improvement in estimated performance.

To be exactly correct, the analysis should contain the effects of tolerances or uncertainties in the link parameters. However, the comparisons are relative and the total uncertainties are similar. Therefore, answers to first order are not affected. This assertion will be tested in later work.

II. Mass, Size, and Transmitter Power Analysis

This analysis does not model all parts of communication system mass, size, and power. It considers only those parts

of the system which compete for mass at the expense of some other part in the downlink communications system. That is, we are looking for a mass minimization and not actual total mass.

Items that have a tare mass, such as transponders, support power converters, microwave components, uplink hardware, emergency communications hardware, and so forth, are not considered in the mass analysis.

As a first order analysis, structure is considered to be proportional to the mass of the communication system. It, therefore, does not enter into the mass optimization process outlined here.

The analysis includes the consideration of mounting the transmitter on the antenna either as a separate package on the backside of a parabolic dish or as an integral design included in an array antenna. The mass of the power and the power system, except for the transmitter power converter, are not considered because they are accounted for in the MSR locomotion requirements. For the MSR, the locomotion power requirements exceed that of the downlink which is only required when the rover is at rest. It is only when the raw power for the transmitter exceeds the power available for locomotion that the communication system is constrained.

Primary communications requirements are for 30 kbps telemetry.

A. Parabolic Dish and Lumped Transmitter Mass Analysis

The mass of the spacecraft Telecommunications System consisting of a downlink components parabolic dish, lumped transmitter, heat radiator and transmitter-power converter, for which there are trade-offs, is as follows:

$$\text{mass} = \text{mass of transmitter}$$

$$+ \text{mass of power converter}$$

$$+ \text{mass of antenna}$$

$$+ \text{mass of heat radiator}$$
$$\text{(if separate from antenna)}$$

In equation form this becomes

$$W = K_T P_T + K_A A_T + K_R A_R + K_C \sqrt{P_T/n_T} \qquad (1)$$

where

W = the mass of the downlink system (kg),

P_T = the spacecraft radiated radio-frequency power (watts),

n_T = the efficiency of converting raw direct-current power to radio-frequency power (dimensionless),

A_T = the actual antenna physical area (meter^2),

A_R = the actual spacecraft heat radiator area used to dissipate the heat not radiated by the antenna surface (meter^2),

K_T = the coefficient that relates transmitter radio-frequency power to mass (kg/watt),

K_A = the coefficient that relates actual physical area of the antenna to mass (kg/meter^2),

K_C = the coefficient that relates the converter power to mass (kg/$\sqrt{\text{watt}}$), and

K_R = the coefficient that relates actual physical area of the heat radiator to mass (kg/meter^2).

Equation (1) must be reduced to one independent variable, say P_T, for the analysis. This will be accomplished by relating the variables P_T, A_T, and A_R to one another. Also, other constraints imposed by the application will be defined. The variables P_T and A_T are related to each other by the Riis Equation and the level of performance to be satisfied by the link. Thus, signal power S is given by

$$S = \frac{P_T L_T (A_T n_T) G_R L_M L_r L_p}{4\pi R^2} \qquad (2)$$

where

P_T = transmitter power (watts)

L_T = transmitter circuit losses $(0 \leqslant L_T \leqslant 1)$

n_T = transmitter antenna efficiency $(0 \leqslant n_T \leqslant 1)$

L_M = data modulation loss, relating data power to total power $(0 \leqslant L_M \leqslant 1)$

G_R = ground receiving antenna gain (dimensionless)

L_p = performance margin for tolerances and weather $(0 \leqslant L_p \leqslant 1)$

L_r = receiving circuit loss $(0 \leqslant L_r \leqslant 1)$

R = range (meters)

Multiplying Eq. (2) by the bit time T_B and dividing by the noise spectral density $N_0 = kT_{sys}$ yields the energy per bit to noise spectral density ratio, a dimensionless quality which together with a channel coding scheme determines system performance. Thus,

$$(ST_B/N_0) = \frac{P_T L_T (A_T \eta_T) G_R L_M L_p T_B}{kT_{sys} 4\pi R^2} \qquad (3)$$

Other parameters in Eq. (3) are

k = Boltzmann's constant, 1.3806×10^{-23} (joules/kelvin)

T_{sys} = system noise temperature (kelvin)

T_B = bit time = 1/data rate (seconds)

1. Solution for the system mass with respect to the transmitter power. Equation (3) can be solved for the product $P_T A_T$ in terms of the other parameters. Thus,

$$P_T A_T = (ST_B/N_0) \frac{kT_{sys} 4\pi R^2}{G_R \eta_T L_M L_T T_B L_p} \qquad (4)$$

The quantity (ST_B/N_0) is related to channel error rate through a function which depends on the particular channel coding scheme in use. A minimum value of (ST_B/N_0) is therefore required to meet the maximum allowable error rate. Equation (4), therefore, amounts to a constraint on the power-area product.

$$P_T A_T \geqslant B_1 \qquad (5)$$

where

$$B_1 = (ST_B/N_0) \frac{kT_{sys} 4\pi R^2}{G_R \eta_T L_M L_T T_B L_p}$$

The area A_T is being kept explicit, rather than antenna gain, because physical size becomes an important constraint, later. The first two terms of Equation (1) are now expressed in terms of P_T.

$$W = K_T P_T + K_A B_1/P_T + K_R A_R + K_C \sqrt{P_T/n_T} \qquad (6)$$

Now, the mass of the heat radiator must be related to transmitter power P_T. In terms of the direct-current to radio-frequency conversion efficiency n_T, the dissipated power is

$$P_D = P_T \left[\frac{1}{n_T} - 1 \right] \qquad (7)$$

Dissipated power can also be related to the area A_D by thermal characteristics of the radiator. Thus,

$$P_D = \epsilon \sigma (T_1^4 - T_2^4) A_D \qquad (8)$$

where

P_D = thermal power radiated (watts)

A_D = radiating area (meter^2)

T_1 = temperature of the surface A_D (kelvin)

T_2 = effective temperature of surrounding space (kelvin)

ϵ = emissivity of the surface ($0 \leqslant \epsilon \leqslant 1$)

σ = Stefan-Boltzmann constant, 5.6696×10^{-8} (watt/kelvin-meter^2)

The process of equating (7) and (8) and solving for A_D yields

$$A_D = P_T \frac{\left[\frac{1}{n_T} - 1 \right]}{\epsilon \sigma (T_1^4 - T_2^4)} \qquad (9)$$

or

$$A_D = P_T B_2 \qquad (10)$$

where

$$B_2 = \frac{\left[\frac{1}{n_T} - 1 \right]}{\epsilon \sigma (T_1^4 - T_2^4)}$$

The total dissipation area A_D is composed of both sides of the transmitting antenna plus an auxiliary area A_r, if $2A_T$ is not sufficient to radiate at the temperatures T_1 and T_2. Thus

$$A_D = A_r + 2A_T \qquad (11)$$

or

$$A_r = A_D - 2A_T \qquad (12)$$

Using the relationships defined in Eqs. (7) through (12), the mass equation (6) becomes

$$W = K_T P_T + K_A B_1/P_T + K_r (A_D - 2A_T) + K_C \sqrt{P_T/n_T}$$
(13)

which becomes

$$W = K_T P_T + (K_A - 2K_r) B_1/P_T + K_r B_2 P_T + K_C \sqrt{P_T/n_T}$$
(14)

Rearranging terms yields

$$W = (K_T + B_2 K_r) P_T + (K_A - 2K_r) B_1/P_T + K_C \sqrt{P_T/n_T}$$
(15)

with the constraint

$$K_r = 0, \quad P_T \leqslant \sqrt{2B_1/B_2}$$

$$= K_R, \quad \text{otherwise}$$
(16)

Physically, this means the extra radiating area vanishes if not needed.

The power converter for the transmitter is part of the mass trade-off with power. This is found to vary with the square root of the power [3]. The mass function of the power converter W_{pc} becomes

$$W_{pc} = K_C \sqrt{P_T/n_T}$$
(17)

where n_T, K_C, and P_T have been previously defined.

2. Solution of the system mass with respect to the antenna area. Previously, the mass W had been determined to be (equation (15)):

$$W = (K_T + B_2 K_r) P_T + (K_A - 2K_r) B_1/P_T + K_C \sqrt{P_T/n_T}$$
(18)

where the power converter had been included. From the relation (5) previously derived,

$$P_T = B_1/A_T$$
(19)

Let us substitute Eq. (19) into Eq. (18) which yields the following:

$$W = (K_T + B_2 K_r) B_1/A_T + (K_A - 2K_r) A_T + K_C \sqrt{B_1/(A_T n_T)}$$
(20)

with the constraint

$$A_D \leqslant 2A_T$$
(21)

Now if we solve for the constraints in terms of A_T, by using Eqs. (5) and (10),

$$A_D = B_2 P_T \leqslant 2A_T$$
(22)

Then we have,

$$A_D = B_1 B_2/A_T \leqslant 2A_T$$
(23)

The final constraint is as follows:

$$K_r = 0, \quad A_T \geqslant \sqrt{B_1 B_2/2}$$

$$= K_R, \quad \text{otherwise}$$
(24)

3. Discussion of parabolic antenna results. The computational results of the preceding formulas for mass in terms of P_T and A_T are embodied in Figs. 1, 2, 3, 4, and 5. They represent the cases of 34 m and 70 m Deep Space Network (DSN) usage for both 8 GHz and 32 GHz for the typical parameters shown in Table 1.

Figures 1 and 2 are for spacecraft antenna and transmitter mass versus spacecraft transmitter power with the 34 m and 70 m Deep Space Stations, respectively, at 8 GHz and 32 GHz. These curves show a distinct minimum mass as the transmitter mass and antenna mass compete with one another. The 32 GHz band is shown as a definite advantage over 8 GHz with regard to mass.

Constraints of 30 watts of radio-frequency power and 1.57 square meters (1.414 meter diameter for dish antenna equivalent to diagonal dimension of 1.0 square meter flat plate array) were assumed and shown on Figs. 1 and 2. The minimum spacecraft antenna and transmitter masses are all within the 30 watt radio-frequency power constraint.

Figures 3 and 4 are for spacecraft antenna and transmitter mass versus spacecraft antenna area with the 34 m and 70 m stations, respectively, at 8 GHz and 32 GHz. These curves also show a distinct minimum mass as the transmitter mass and antenna mass compete with one another. However, for the 34 m DSN antenna, the minimum mass 8 GHz design is slightly outside of the area constraint.

The minimums of the curves shown in Figs. 1, 2, 3, and 4 are rather broad. As a result only a slight penalty is suffered when the design is slightly off the minimum. Figure 5 shows

the requirements for the power-area product for the 34 m and 70 m stations, respectively, for 8 GHz and 32 GHz. The area and power constraints are also shown on this figure.

B. Flat-Plate Array Antenna and Distributed Transmitter Analysis

The flat-plate array differs from the parabolic dish and lumped transmitter combination considerably. One aspect of these differences is that the transmitter is integrated into the antenna surface with each antenna element. That is, one gets an elemental power associated with each elemental area of the array. In essence, one obtains an elemental power-area product for each elemental area. Although the elemental power is adjustable, the mass of the assembly is not a strong function of the radiated radio-frequency power. This makes the analysis and optimization different from the parabolic dish and lumped transmitter case presented before in that there is no obvious power-area trade-off for the flat plate array.

1. Solution of the system mass

a. Area. The area of the array is made up of discrete antenna elements distributed over one surface of the flat plate. These are distributed in a definite pattern which will be assumed to be uniform over a square plate as shown in Fig. 6. A square configuration is not essential and is only used for the convenience of analysis. The elements will also be distributed with a separation related to the wavelength. The separation Λ than is related by:

$$\Lambda = D\lambda = D\,c/f \qquad (25)$$

where

Λ is the separation of the antenna elements (meters),

D relates the separation of the elements to the wavelength (dimensionless),

λ is the wavelength (meters),

c is the velocity of light (meters/second), and

f is the frequency of the transmitter (hertz).

There are N antenna elements in each row and column for a total of N^2 elements on the flat plate. Each antenna element occupies an area which is related to the following:

$$A_o = (D\lambda)^2 \qquad (26)$$

where A_o is the physical area occupied by each antenna element (meter^2).

The total physical area (one side of the flat plate) then becomes:

$$A_T = N^2 A_o \qquad (27)$$

where A_T is the total one sided physical area of the flat plate (meter^2).

b. Transmitter. The transmitter is distributed in discrete components immediately behind the discrete antennas for low radio-frequency losses. They are thermally part of the array for heat dissipation. Each transmitter is isolated from one another with metal boxes to make their operation as independent as possible. Each is excited from a manifold whose purpose is to distribute radio-frequency power uniformly with a stable phase and amplitude (except in the case of an electronically steerable array). There is also a direct-current power distribution system associated with the transmitter elements. The mass of the boxes for isolation will be considered to be part of the array structure while the manifold and direct-current power distribution system will be considered to be part of the transmitter.

The mass of the transmitter element is depicted as shown in Fig. 7. From this figure, the mass does not reduce below W_o with power P_o because of the tare mass of the manifold and direct-current power distribution system. Therefore, the base power to be considered will be P_o. The radio-frequency output power of the array can be written as:

$$P_T = P_o N^2 (2^M)^m \qquad (28)$$

where

P_o =   the element base radio-frequency power (watts),

P_T =   the total radio-frequency power (watts),

m =   0, 1, 2, . . . , 22 for 8 GHz (dimensionless) (maximum power = 2.5 watts, m = 50),

m =   0, 1, 2, . . . , 8 for 32 GHz (dimensionless) (maximum power = 0.05 watts, m = 8), and

M =   1/4 (m, M are selected for computing values of radio-frequency powers and masses in plotting).

c. Power-area product. From the previous two sections, the power-area product becomes:

$$P_T A_T = P_o A_o N^4 (2^M)^m \qquad (29)$$

where the terms have already been defined. Now the required power-area product is related by equation (4) which can be written as:

$$P_T A_T = (ST_B/N_0) \frac{kT_{sys} \, 4\pi R^2}{G_R \eta_T L_M L_T T_B L_P} = B_1 \qquad (30)$$

where the terms have already been defined.

d. Total mass. The mass of the flat-plate array system, like equation (1), can be defined as:

mass = mass of flat plate structure

+ mass of transmitter

+ mass of heat radiator
(if separate from flat plate array).

Example designs have been performed where the mass of the transmitter has been estimated to be 10% of the total flat plate array mass when the transmitter element power P_o is 0.05 watts. The total mass of the element (kg) including transmitter is

$$W_o = K_A A_o \qquad (31)$$

where K_A and A_o have been previously defined. The mass of the flat-plate structure is then

$$W_A = 0.9 \, W_o N^2 = 0.9 \, K_A A_o N^2 \qquad (32)$$

The mass of the transmitter becomes

$$W_T = 0.1 \, W_o N^2 \, 10^{0.01574m} = 0.1 \, K_A A_o N^2 \, 10^{0.01574m} \qquad (33)$$

where

W_A = the mass of the flat plate structure or flat plate without the transmitter (kg)

W_T = the mass of the transmitter (kg)

The factor

$$10^{0.01574m} \qquad (34)$$

accounts for the compounding effect of the transmitter mass increase of 15% with every doubling of radio-frequency power.

The mass of the radiator was previously defined as

$$W_R = K_r (A_D - 2A_T) \qquad (35)$$

where

$$K_r = 0, \text{ if } A_D \leqslant 2A_T$$
$$= K_R, \text{ otherwise} \qquad (36)$$

and

$$A_D = P_T \frac{\left[\frac{1}{n_T} - 1 \right]}{e\sigma (T_1^4 - T_2^4)} = P_T B_2 \qquad (37)$$

By making the appropriate substitutions,

$$W_R = K_r [P_o N^2 (2^M)^m B_2 - 2A_o N^2] \qquad (38)$$

so that the total mass is

$$W = 0.9 \, K_A A_T + 0.1 \, K_A A_T \cdot 10^{0.01574m}$$
$$+ K_r [P_o N^2 (2^M)^m B_2 - 2A_T] + K_C \left[\frac{P_o N^2 (2^M)^m}{n_T} \right]^{1/2} \qquad (39)$$

with the constraint

$$K_r = 0, \text{ if } P_o N^2 (2^M)^m B_2 \leqslant 2A_t$$
$$= K_R, \text{ otherwise} \qquad (40)$$

2. Power-area requirement. The minimization of the flat-plate array does not occur in the same way as it does in the parabolic dish case. There is no choice of area versus power as in the case of the parabolic dish. Power and area are directly coupled. The choice that the designer has at his disposal is in the selection of the number of elemenets or possibly the power output of each element, P_o.

To show the minimization on the cuves that will result from the analysis, it is essential to compute and draw the power-area requirement to meet the system performance. This is B_1 as shown in a previous section.

3. Discussion of flat-plate array results. The computational results of the preceding formulas for the flat-plate array are embodied in Figs. 8 and 9. They represent the cases of 34 m and 70 m DSN usage for both 8 GHz and 32 GHz for the indicated parameters.

Figure 8 is for spacecraft antenna and transmitter mass versus spacecraft power-area product at 8 GHz and 32 GHz. The number of elements across the side of the flat plate, N, is used as a parameter as well as the power $\times$ area requirements B_1 of equation (5). On the left hand side of this curve the shape is determined largely by the power converter. On the right hand side, the shape for the 8 GHz curves are determined largely by the flat-plate array mass while the 32 GHz curves are determined by a combination of the flat-plate array mass and the heat radiator. The heat radiator is more of an effect for the 32 GHz case because the size of the elements are sixteen times smaller for the same number of elements, N. This effect did not show for 8 GHz even though the 8 GHz element was capable of about ten times the power of the 32 GHz element.

Examining the curves on Fig. 8, the 34 m performance requirement curve intersects the 8 GHz spacecraft antenna-transmitter mass curves for the number of elements 7 through 15. The mass is monotonically increasing with the number of elements, N. The minimum mass occurs for $N = 7$ (minimum on the boundary). An examination of the curves for 32 GHz shows that the 70 m performance requirement case intersects the 32 GHz spacecraft antenna-transmitter mass curves with the number of elements 10 through 13. Because of the peculiar way the power converter and heat radiator combine, the mass generally decreases with the number of elements, N. In some cases the mass can actually show a minimum as a function of the number of elements, N. This effect is more pronounced in studies without the power converter mass added (not shown).

Figure 9 shows the spacecraft array RF power versus spacecraft array area with the number of elements, N, and power-area product requirements for both the 34 m and 70 m DSN usages and 8 GHz and 32 GHz. Also shown are the assumed constraints of 1 square meter (1.4 meter diagonally) for the antenna area and 30 watts for the radio-frequency power. This allows one to determine if the minimum mass can be achieved for the number of elements mentioned above. For instance, this curve shows that the minimum mass with the number of elements of 7 for the 8 GHz 34 m, cannot be achieved because 9 must be used due to the power constraint.

An examination of the curves for the flat-plate array, compared to the parabolic dish, shows that 32 GHz has a decided mass advantage over 8 GHz.

III. Discussion of Parameters

A. Transmitters and Power Supplies

In general, redundant transmitters are required with the exception of the distributed ones such as that used in the flat-plate array which has inherent redundancy. For this reason, the mass of the transmitters such as traveling-wave tubes and solid-state amplifiers are doubled.

The switching mechanisms of complicated power supplies such as used on traveling-wave tube amplifiers are built with their individual power supplies and are therefore also doubled. Solid-state RF amplifiers will likely have their own power supplies also.

Distributed arrays (power amplifiers-antenna elements) have a certain amount of effective redundancy built into the system so that failure of one or several transmitting elements only partially degrades the output of the array. For this reason, the distributed power amplifier is not doubled for redundancy. The power converter for the array, however, can fail. Rather than having the power switched between redundant power converters, the power would be derived from split power converters, each serving half of the distributed power amplifiers. That is, a single power converter failure only causes roughly three decibels degradation in the communication link.

Since the mass of the power converter is a function of the square root of the delivered power, the mass of the split power converters increases by the square root of two over a single power converter.

The coefficient to convert power-converter output to mass is derived from the Mars Sample Return Technology Study. This data is consistent with [3] which is 0.38 kg/$\sqrt{\text{watt}}$. This article assumes that this coefficient includes the power-converter packaging. It also assumes that the power converter is mounted on the body of the Mars Sample Return for purposes of heat dissipation and requires no special heat radiator. Power from the power converter is wired across gimbals for the radio-frequency power amplifiers.

The coefficient to convert radio-frequency power output to transmitter mass has been derived. For traveling-wave tube amplifiers, this number is 0.434 kg/watt. For the distributed amplifier coefficient, see the discussion in Section II. This was related to the mass of the flat-plate array itself.

The mass for the distributed power amplifiers for the flat plate array, as shown in the analysis, is rather insensitive to the power output. The primary cause for this is the assumption by G. Klein[1] that the structure for the radio-frequency amplifiers, antenna elements, manifolds and heat conduction mass

---

[1] G. Klein, Planetary Spacecraft Systems Technology, Final Report 1986, JPL D-3731 (internal document), Jet Propulsion Laboratory, Pasadena, Calif., 1986.

had a density of 0.25 of that of a solid billet of aluminum. This makes the mass much larger than subsequent estimates by L. Riley [4].

B. Antennas

The mass of parabolic antennas was based on the Viking (V075) graphite-epoxy honeycomb dishes. It was assumed that the only mass variable of choice was that of the dish area. That is, the feed was about the same mass for antenna size or frequency. Area efficiencies assumed for the parabolic dish were 55% for both 8 GHz and 32 GHz.

The flat-plate array mass has been discussed in the section above. The flat-plate array design assumed elements with a separation of Λ. This separation will cause lobing of the antenna pattern. It has been assumed that this can be overcome by breaking each element into subelements with a net power

of a single element. Area efficiencies for the flat-plate array are assumed to be 0.9 at all frequencies.

IV. Summary

Within the constraints and parameters assumed, a viable design can be made to perform the telecommunications part of the Mars Sample Return Mission at either 8 GHz or 32 GHz. Under these circumstances, the mass, power and size show a definite advantage of roughly 2:1 of using the 32 GHz over 8 GHz as shown in Table 2.

In the designs shown above, there is no advantage of mass for the parabolic antenna versus the flat-plate array for a fixed frequency. It is believed that a much lighter design for the flat plate can be made than the example one chosen here and will show an advantage in mass in the future. The flat plate example design does show a definite advantage of size.

Acknowledgment

References

[1] W. A. Imbriale, A. M. Bhanji, S. Blank, V. B. Lobb, R. Levy, and S. Rocci, "Ka-band (32 GHz) Performance of 70-Meter Antennas in the Deep Space Network," *TDA Progress Report 42-88*, vol. October–December 1986, Jet Propulsion Laboratory, Pasadena, California, pp. 126–134, February 15, 1987.

[2] M. A. Koerner, "Relative Performance of X-band and 32 GHz Telemetry Links on the Basis of Total Data Return Per Pass," *TDA Progress Report 42-87*, vol. July–September, 1986, Jet Propulsion Laboratory, Pasadena, California, pp. 65–80, November 15, 1986.

[3] J. Leisenring, "Study and Analysis of Satellite Power Systems Configurations for Maximum Utilization of Power," *NASA Report CR-898*, TRW Systems, Redondo Beach, Calif., for Goddard Space Flight Center, October, 1967.

[4] A. L. Riley, "Ka-Band (32 GHz) Spacecraft Development Plan," *TDA Progress Report 42-88*, vol. October–December, 1986, Jet Propulsion Laboratory, Pasadena, Calif., pp. 164-173 February 15, 1987.

Table 1. Typical parameters used for results

Parameters	X-Band	Ka-Band
DSN		
Canberra, Improved 34 m		
Antenna Gain, dB	67.62	78.57
System Noise Temperature, K	24.98	31.2
Canberra, Improved 70 m		
Antenna Gain, dB	73.89	84.84
System Noise Temperature, K	24.98	31.2
Frequency, GHz	8.450	32.0
Elevation Angle, deg	30	30
SYSTEM		
Range, AU	2.683	2.683
Bit Rate, bps	30000	30000
ST/N_0, dB	4	4
Circuit and Polarization Losses, dB	-0.86	-0.92
Performance Margin, dB	-1.15	-3.55
Link Reliability, %	90	90
SPACECRAFT		
VO 75 Parabolic Dish, Heat Radiator; Redundant TWTAs and		
Power Converters		
Antenna Area Efficiency	0.55	0.55
Antenna Area to Weight, kg/m^2	2.94	2.94
Transmitter Power to Weight, kg/Watt	0.434	0.434
Radiator Area to Weight, kg/m^2	20.77	20.77
Power Converter Power to Weight, kg/Watt$^{0.5}$	0.76	0.76
Flat Plate Array/Transmitter, Heat Radiator;		
Split Power Converter		
Antenna Area Efficiency	0.9	0.9
Modulation Loss Factor	0.9698	0.9698
Antenna Area to Weight, kg/m^2	25.7	25.7
Radiator Area to Weight, kg/m^2	20.77	20.77
Power Converter Power to Weight, kg/Watt$^{0.5}$	0.537	0.537
Emissivity, %	75	75
Antenna Temperature, K	380	380
Surrounding Temperature, K	260	260
Modulation Loss Factor	0.9698	0.9698

Table 2. Optimum design analysis results

	34m						70 m					
	8 GHZ			32 GHz			8 GHz			32 GHz		
	W	m^2	kg	W	m^2	kg	W	m^2	kg	W	m^2	kg
Parabola	13	1.6**	17	5.8	0.89	8.8	6.8	1.0	8.8	2.9	0.4	5.8
Flat Plate	30*	0.4	26	20	0.11	8.0	30	0.11	11	13	0.06	5.4
No. of Elements		902			1802			502			13	

*Power constrained design
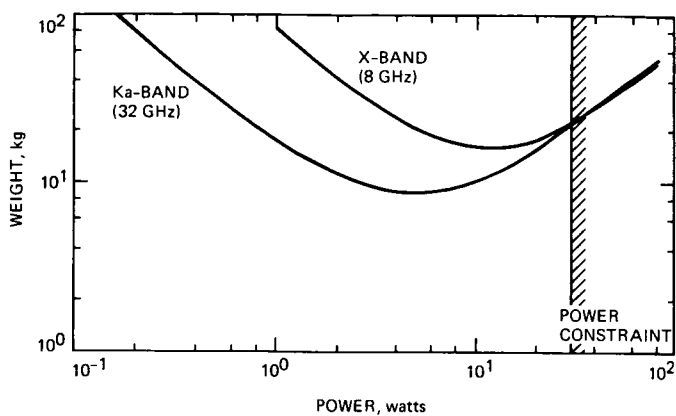**Area (envelope) constrained design

Fig. 1. The weight of the spacecraft's parabolic antenna and transmitter vs its transmitter RF power for 8 and 32 GHz using the Canberra improved 34-m antenna

Fig. 2. The weight of the spacecraft's parabolic antenna and transmitter vs its transmitter RF power for 8 and 32 GHz using the Canberra improved 70-m antenna
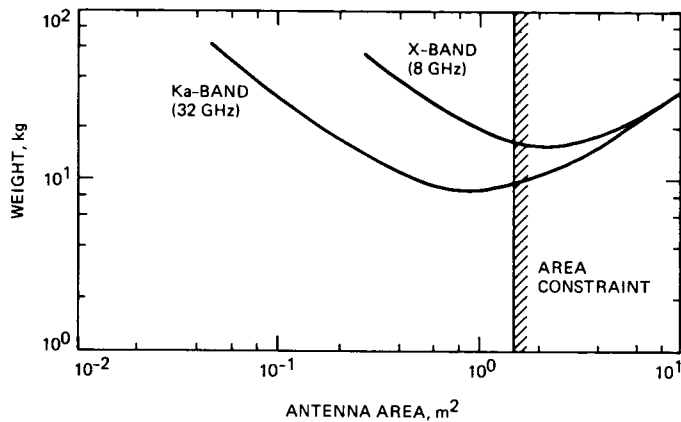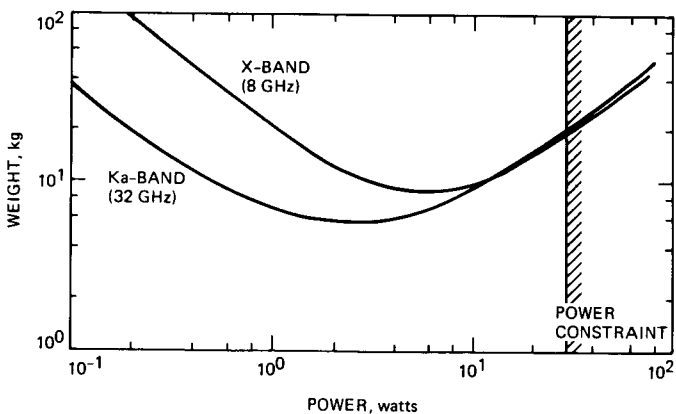

Fig. 3. The weight of the spacecraft's parabolic antenna and transmitter vs the antenna area for 8 and 32 GHz using the Canberra improved 34-m antenna
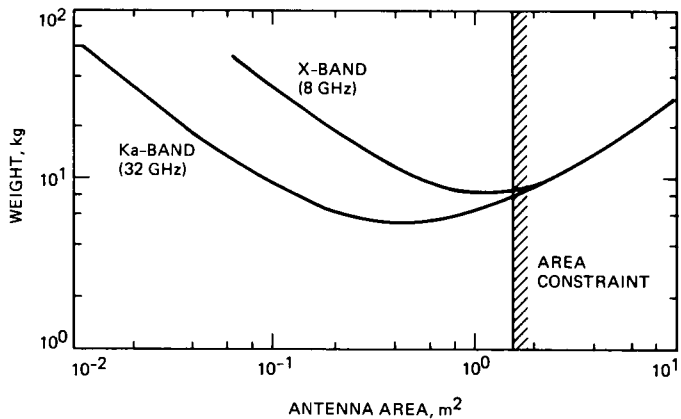

Fig. 4. The weight of the spacecarft's parabolic antenna and transmitter vs the antenna area for 8 and 32 GHz using the Canberra improved 70-m antenna
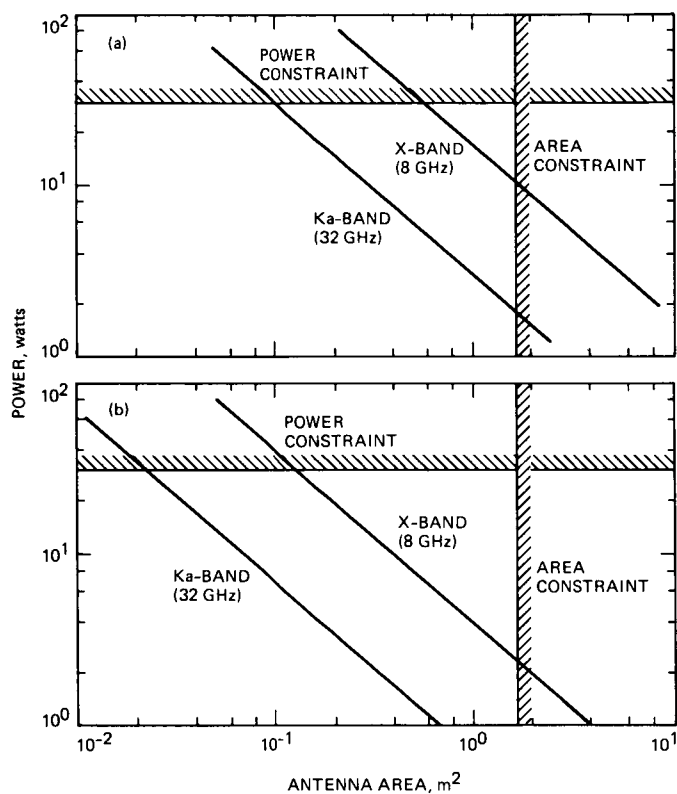
Fig. 5. The required spacecraft parabolic antenna RF power-area product vs RF transmitter power and antenna area for 8 and 32 GHz: (a) Canberra improved 34-m antenna and (b) Canberra improved 70-m antenna
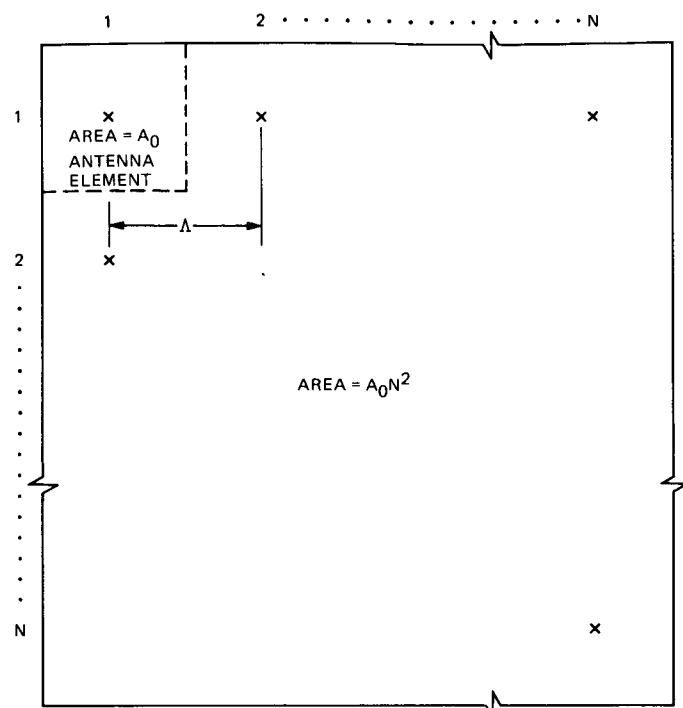

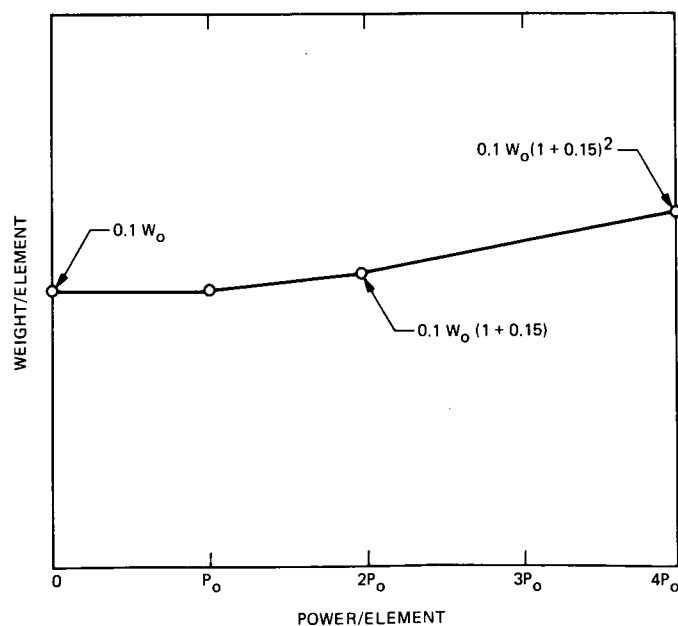Fig. 6. Flat-plate array layout

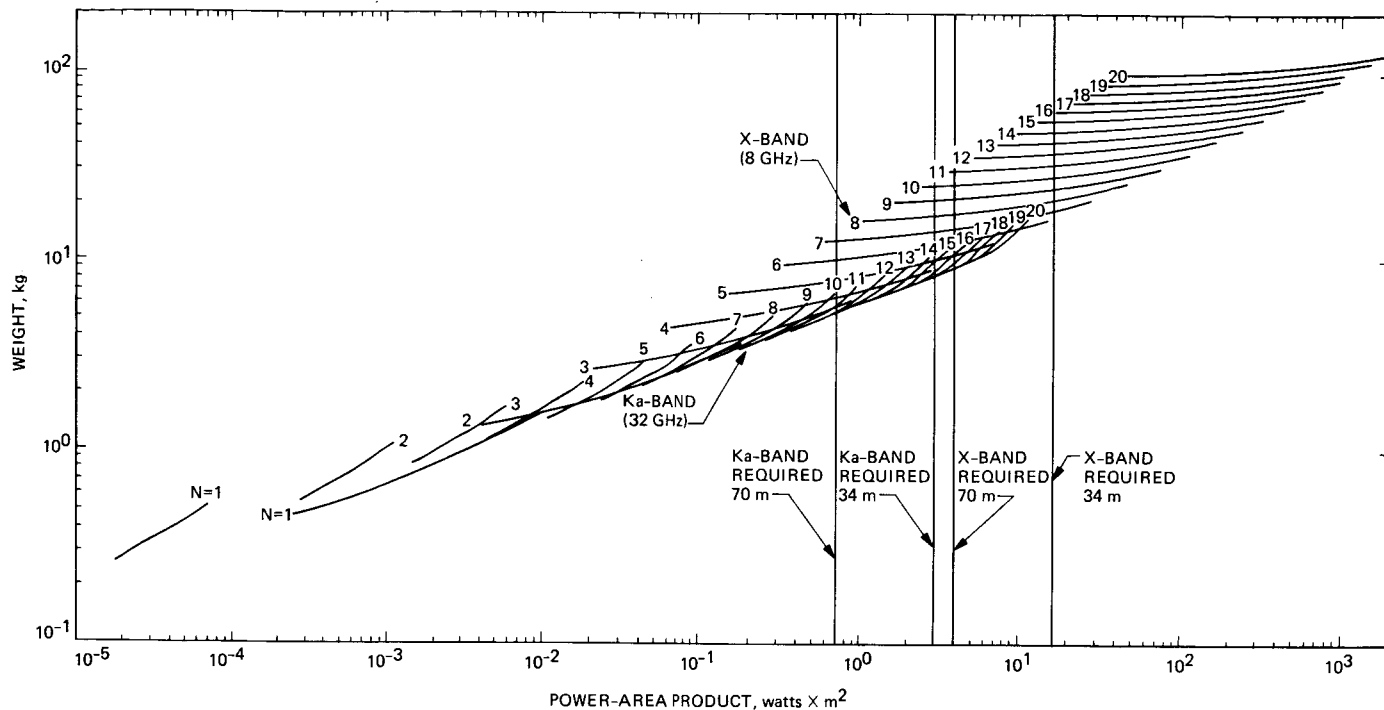Fig. 7. Weight vs power for the flat-plate array

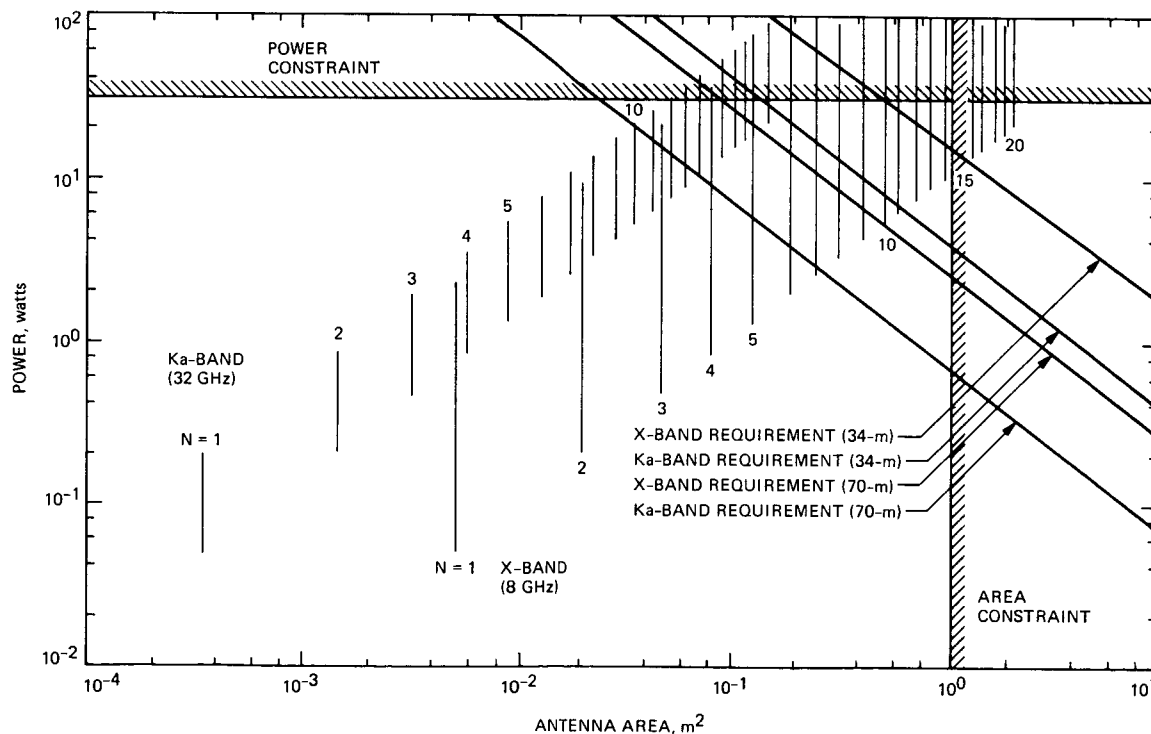**Fig. 8. The flat-plate array weight vs power-area product**

Fig. 9. The required and available flat-plate array RF power area product vs RF transmitter power and antenna area for 8 and 32 GHz, number _N_, and Canberra improved 34- and 70-m antennas

Use of a 2.3-GHz Traveling-Wave Maser on the Usuda 64-Meter Antenna

D. Neff

Radio Frequency and Microwave Subsystems Section

A 2.3-GHz traveling-wave maser/closed-cycle refrigeration system was installed on the 64-m antenna at Usuda, Japan. This was done to evaluate the beam-waveguide antenna noise performance, and to support the International Cometary Explorer's (ICE's) comet flyby mission. System noise temperature at 2270 MHz was measured to be 15 K, including the maser noise contribution of 2.5 K. Maser installation and noise performance are described. The Usuda 64-m antenna is of high quality with a system operating noise temperature better than the DSN 64-m antennas.

I. Introduction

The Institute of Space and Astronautical Science (ISAS), a Japanese agency that is similar in function to NASA, completed construction of a 64-m cassegrain antenna in October 1984 at Usuda, Japan, approximately 180 km west of Tokyo. This antenna is a more modern design than the DSN 64-m antennas, the first of which was completed in 1966. The Usuda antenna uses shaped main and subreflector surfaces, a beam-waveguide feed system, automatic subreflector positioning, extensive digital control systems, very modern receiver equipment with fiber optics interface to the antenna, and automated station control with remote monitor and control capabilities from Tokyo.

NASA's interest in the antenna's beam-waveguide noise temperature performance and a decision to use the antenna for tracking the International Cometary Explorer (ICE) [1] prompted an agreement to ship, install, and operate a 2.3-GHz traveling-wave maser (TWM) and closed-cycle refrigerator (CCR) system to support the ICE Giacobini-Zinner comet

flyby. This article describes the preparation, installation, testing, and operation of the TWM-CCR system in support of these objectives.

II. Preparation

Starting in August 1984, new equipment was ordered and existing equipment was assembled for the planned TWM-CCR installation at Usuda. The equipment required for the installation, operation, and maintenance of the system had to be supplied from JPL to the site. A TWM developed in 1973 [2] was available, as well as a compressor and helium purifier from the JPL and DSN inventory. The balance of the system was borrowed from several other projects to reduce costs (all equipment was returned to JPL when the task was completed). The TWM was tested at JPL on the roof of Building 238 in March 1984, and the results were virtually identical with the noise data taken in 1974 at 2295 MHz (Table 1). The total system noise operating temperature (T_{op}), measured at 2270 MHz (10.2 K), was quite acceptable, so the TWM components were shipped in March 1985 via air freight.

III. Site

The antenna (Fig. 1) is located in a forest preserve on the side of a mountain at a 1074-m elevation (N = 36°07'49", E = 138°22'03"), approximately 15 km from the town of Usuda in the Nagano prefecture. Standard access to Usuda is by train via Komora from Tokyo Ueno Station. Travel time is 3 to 4 hours, depending on transfer connections at Komora. Equipment must be transported by truck from Narita Airport (80 km west of Tokyo) over generally good roads. The last 8 km are over a maintained dirt road. Access in the winter is sporadic due to heavy snow at various times. Rain is a common occurrence the rest of the year and varies from clouds and mist to heavy precipitation. A dormitory building has recently been completed to reduce travel requirements for personnel working at the site.

IV. Installation and Layout

Mitsubishi Electric Company (MELCO) installed a 2.3-GHz feedhorn in a low-noise configuration for use with a TWM (Fig. 2). The antenna feedhorn, complete with polarizer and orthomode transducer, terminates in an air-conditioned room, allowing easy access to equipment. The maser equipment rack (Fig. 2) was located adjacent to the maser, requiring only a 3-m cable run. The compressor is in another room where temperatures can vary between –20°C and above 35°C (Fig. 3). Earthquakes are a constant threat in Japan, and therefore everything was braced and securely bolted in place to the antenna structure.

A block diagram of the antenna microwave front end and TWM system is shown in Fig. 4. The front end consists of the following:

Main 64-m shaped surface

Shaped cassegrain subreflector

Four beam waveguide reflecting surfaces [1]

S-band antenna feedhorn

RCP/LCP orthomode polarizer

WR 430 waveguide switch

WR 430 waveguide

33-dB directional coupler

TWN/CCR assembly

The beam-waveguide system uses a movable mirror as a switch to connect to other feeds. A separate feedhorn with angle tracking and diplexed transmitter and receiving ability can be used for two-way communications with spacecraft at S-band.

V. Problems

Maser testing at the site was delayed a week because of a CCR warm-up problem during the test period allocated by MELCO. The station ran on a rather fixed and predetermined schedule because of the ongoing antenna work and acceptance testing being performed by MELCO. The TWM system testing was later restricted to brief periods before and after actual tracking periods.

The TWM experienced warm-up problems about every 4 to 6 days when first installed. Troubleshooting was difficult because the station was not manned 24 hours a day and failures often occurred during the night. The warm-up problems were believed to be caused by helium gas contamination, either from the compressor or from the helium supply source. The helium gas purity at the station was checked and found to be at least 99.999 percent pure. It was next suspected that the problem might be associated with the CCR drive cylinder system. The drive was changed with no improvement. Finally, the helium compressor was replaced with a spare unit. This contamination problem was not observed again, and the TWM operated normally during tracking periods for the ICE spacecraft. The suspect compressor was returned to JPL, where it was found to exhibit the same symptoms with a second refrigerator as those observed at Usuda. This compressor has subsequently been found to have an oil breakdown problem not observed in other compressors. The exact failure mechanism is not yet known, but an overheated component in the 440 three-phase motor or head assembly is suspected.

VI. Test Results

The first T_{op} measurement was made on April 29, 1985 using the cold sky/ambient load Y-factor technique. During clear sky conditions with the antenna at zenith, T_{op} measured 15.7 K at 2270 MHz and 15.0 K at 2295 MHz. After additional TWM tuning experience was obtained at Usuda, T_{op} final measurements of 15.0 K at 2270 MHz and 15.0 K at 2295 MHz were obtained. The net maser gain was between 45 and 50 dB, and instantaneous bandwidth (at –3 dB points) was approximately 20 MHz.

A tipping curve from 10-deg elevation to zenith was made and is plotted in Fig. 5. Data from a typical DSN antenna is shown for comparison. The subreflector support is a tripod rather than the quadripod structure used in the DSN and results in less blockage and lower ground noise. The improved noise performance, compared to the DSN data, varies from 1.5 K at the zenith to 4.5 k at the 10-deg elevation angle. The system noise temperature performance comparison between an existing operational DSN S-band antenna and the Usuda antenna is shown in Table 2 (from [1]).

VII. Beam-Waveguide System

The fact that the system noise temperature remained normal during heavy rain and did not increase is due to the design of the beam-waveguide system, since the horn window is protected from rain and is heated to prevent water condensation.

The beam-waveguide system (shown in [1]) consists of an approximately 3.5-meter-diameter tube with the necessary reflectors to refocus the microwave energy to the feedhorn. The feedhorn is a Potter dual mode sheet metal type [3], and is about 7 meters in length. The length (which is about twice that of DSN feedhorns) is required to reduce phase error at the horn aperture—a requirement of the beam waveguide system. The antenna in its present configuration has provisions for other antenna feedhorns, either at the same frequency or at other frequencies.

VIII. Summary

The ISAS Usuda 64-m antenna is a modern beam-waveguide antenna of superb quality with operating noise temperature performance better than the DSN 64-m antennas. The most outstanding feature from a hardware point of view is the ability to quickly install and maintain large pieces of equipment. The beam waveguide allows flexibility for multiple feed systems, multiple frequency bands, and expansion for future programs without compromising the performance of any existing front end system.

All goals of the ICE Giacobini-Zinner comet encounter involving the installation of the 2.3-GHz TWM were met, and much was learned about the new ISAS 64-m antenna. Future DSN antenna construction should consider the features and merits of the Japanese design.

Acknowledgment

References

[1] J. P. Goodwin, "Usuda Deep Space Center Support for ICE," *TDA Progress Report 42-84*, October–December 1985, pp. 186–196, Jet Propulsion Laboratory, Pasadena, Calif., February 15, 1986.

[2] R. Clauss and E. Wiebe, "Low-Noise Receivers: Microwave Maser Development," *JPL Technical Report 32-1526, Vol. XIX*, November–December 1973, pp. 93–99, Jet Propulsion Laboratory, Pasadena, Calif., February 15, 1974.

[3] P. D. Potter, "A New Horn Antenna with Suppressed Sidelobes and Equal Beamwidths," *Microwave Journal*, Vol. 6, pp. 71–78, 1963.

Table. 1. The comparison of system noise temperatures

Frequency, MHz	T_{op}, K	TWM, K	T_{op}, Switch and Coupler, K	Year
2295	8.3	2.1	N/A	1974
2295	8.3	2.2	8.5	1985
2270	9.1	3.0	10.2	1985

Table 2. System comparison

Components	DSS 14, K*		Usuda, K*	
	Zenith	30-deg Elevation	Zenith	30-deg Elevation
TWM	2.5	2.5	2.5	2.5
Feed Components†	4.4	4.4	3.9	3.9
Antenna (spillover)	4.5	6.7	4.0	4.9
Sky (cosmic + atmos.)	4.6	6.5	4.6	6.5
Totals	16.0	20.1	15.0	17.8

*Low-noise configuration, 2295 MHz.

†Feed components at DSS 14 include: calibration coupler, switch, transmit filter, orothomode junction, polarizer, rotary joints, feedhorn and two reflex feed reflectors. Feed componets at Usuda include: calibration coupler, switch, orothomode junction, polarizer, moder generator, feedhorn, and four beam-waveguide reflectors.
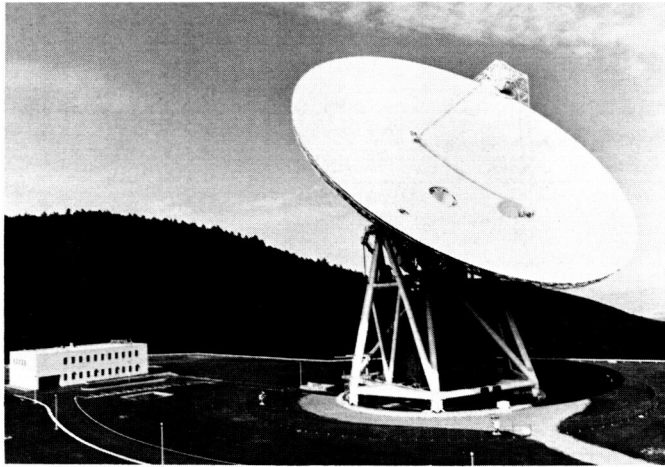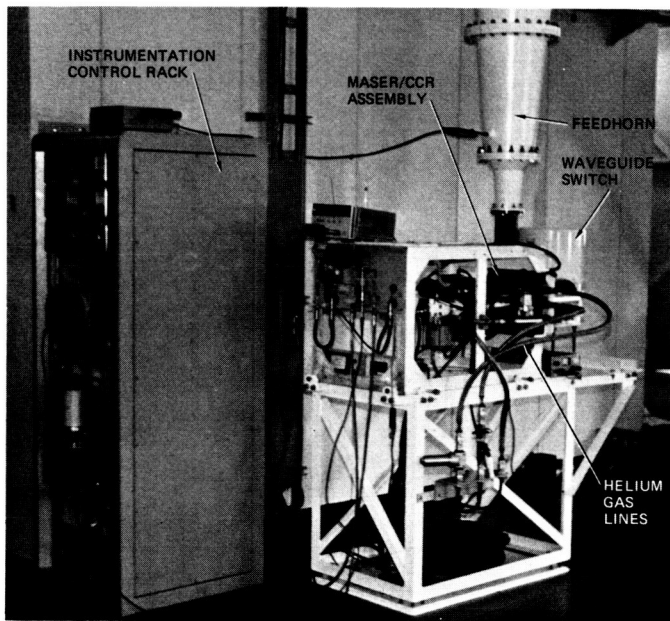
Fig. 1. Usuda antenna

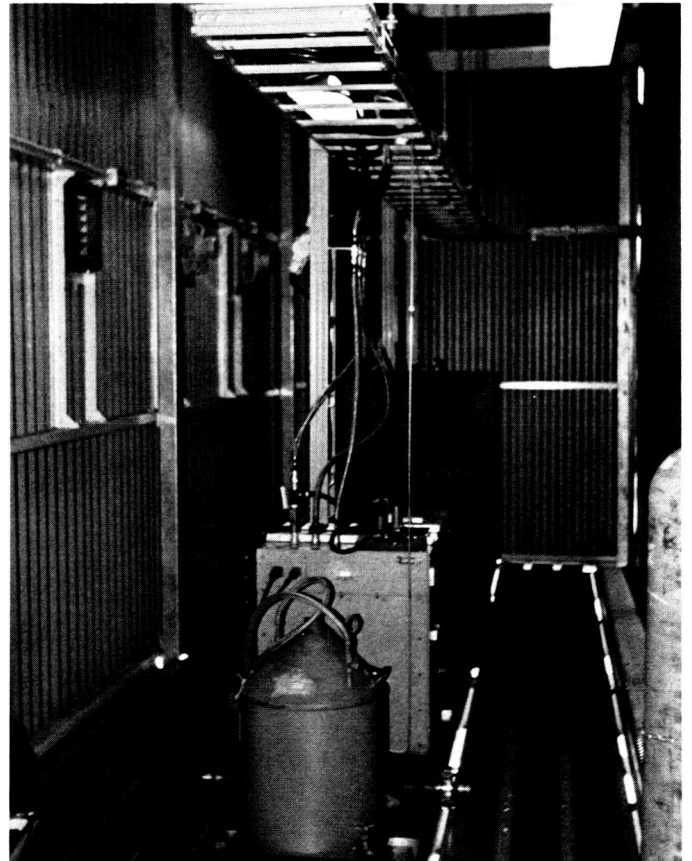Fig. 2. Maser and instrumentation equipment
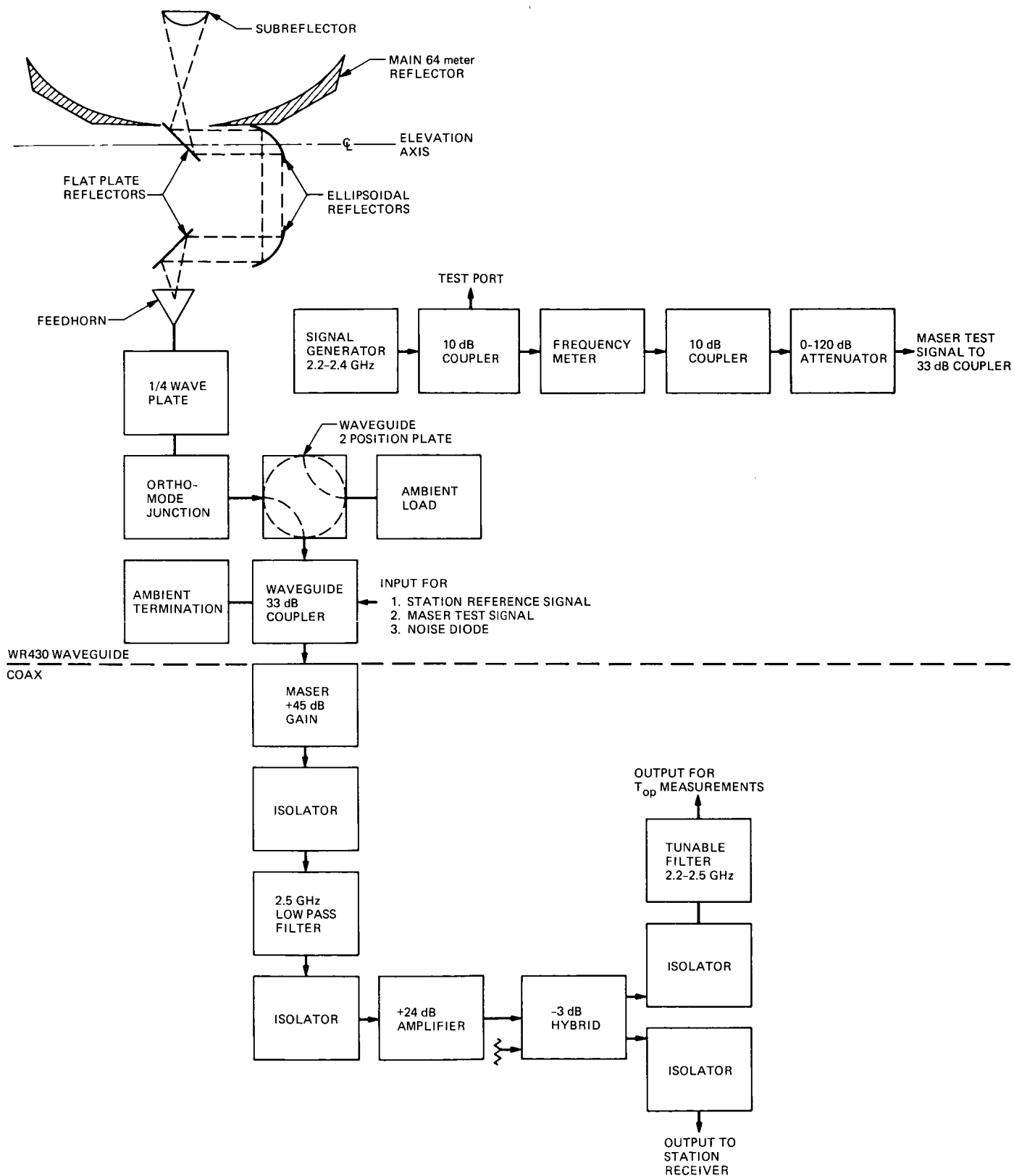

Fig. 3. Compressor room
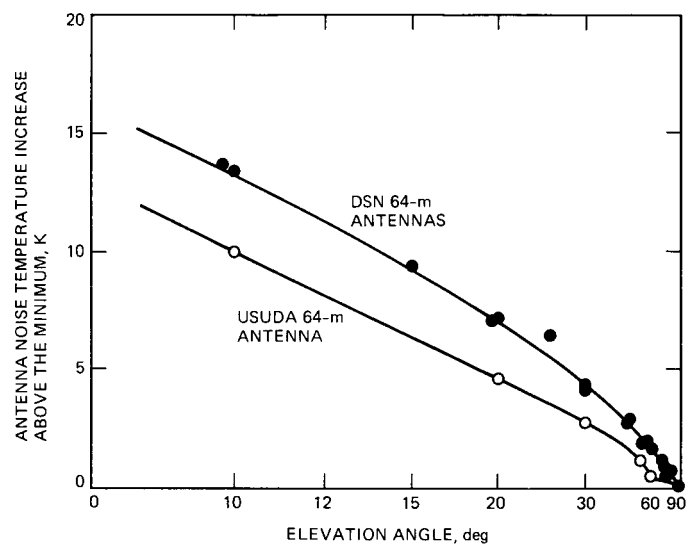
Fig. 4. RF block diagram

Fig. 5. Tipping curve

A VLSI Single Chip (255,223) Reed-Solomon Encoder With Interleaver

I. S. Hsu, L. J. Deutsch, and T. K. Truong
Communications Systems Research Section

I. S. Reed
Electrical Engineering Department
University of Southern California

This article presents a description of a single-chip implementation of a Reed-Solomon encoder with interleaving capability. The code used was adapted by the CCSDS (Consulative Committee on Space Data Systems). It forms the outer code of the NASA standard concatenated coding system which includes a convolutional inner code of rate 1/2 and constraint length 7. The architecture, leading to this single VLSI chip design, makes use of a bit-serial finite field multiplication algorithm due to E. R. Berlekamp.

I. Introduction

A concatenated coding system consisting of a convolutional inner code and a Reed-Solomon outer code has been adopted as a guideline for downlink telemetry for future space missions by CCSDS (Consultative Committee for Space Data Systems) [1]. The participants in this committee include the European Space Agency (ESA) and NASA as well as space agencies from many other nations.

The convolutional inner code is the same (7, 1/2) code used by NASA's Voyager project. The outer Reed-Solomon code is a (255, 223) block code on 8-bit symbols and it is capable of correcting up to 16 symbol errors. The performance of such a scheme is investigated in [2]. It is shown that this concatenated channel provides a coding gain of almost 2 dB over the convolutional-only channel at a decoded bit error rate of 10^{-5}.

One of the benefits of concatenated coding, and one of the main motivations for its acceptance as a standard system, is that it provides for nearly error free communication links at fairly low signal power levels. This means that source data compression techniques [3] can be used to help increase channel throughput without a substantial change in overall error rate. Data compression algorithms, while promising to remove substantial information redundancy are very sensitive to transmission errors. An end-to-end study of a system using concatenated coding with data compression can be found in [4].

The interleaving buffers are required because the inner decoder errors tend to occur in bursts, which occasionally are as long as several constraint lengths. The outer decoder remains undisturbed by burst errors which occur within a given 8-bit symbol (which corresponds to about one con-

straint length of the inner convolutional code). However, its performance is severely degraded by highly correlated errors among several successive symbols. As a consequence, interleaving is required for best performance.

A Reed-Solomon encoder is basically a circuit which performs polynomial division in a finite field. Such circuits are well known [5] and the implementation is straight forward. The major problem in designing a small encoder is the large quantity of hardware that is necessary to perform the finite field multiplications.

Due to the limited weight, space and power that can be allotted to a spacecraft instrument, the equipment used must be as light and as small as possible. Therefore, a single chip Reed-Solomon encoder can have a significant advantage in deep-space probe missions. Such an encoder represents a considerable space, weight and power savings over the smallest existing encoder (about 30 chips).

A conventional encoder described in [5] for the (255, 223) RS code, requires 32 finite field multipliers. These multipliers are usually implemented as full parallel multipliers or table lookup multipliers. The use of either of these multiplication algorithms prohibits the implementation of the encoder on a single medium density VLSI chip.

Fortunately, E, R. Berlekamp [6] developed a serial algorithm for finite field multiplication over a binary field. Berlekamp's algorithm requires only shifting and exclusive–OR operation. Recently, it is shown [7] that this multiplication algorithm makes possible the design of a workable VLSI architecture and that this new dual-basis (255, 223) RS encoder can be readily realized on a single VLSI chip with NMOS technology.

In this article, an extension of the previous work is presented. It is demonstrated in this article that a (255, 223) RS encoder with 5-depth interleaving capability also can be implemented on a single VLSI chip with NMOS technology.

II. Review of Interleaving Algorithm

The basic block diagram of a concatenated coding system is shown in Fig. 1. The inner encoder-decoder is a convolutional encoder, while the receiver utilizes Viterbi (maximum likelihood) decoder. The outer code is a high rate block code.

It is demonstrated [2] that this concatenated channel provides more than 2 dB of coding gain over the convolutional-only channel. However, the performance of the recommended Reed-Solomon coding scheme in the concatenated coding system can only be achieved when the bursts of errors appearing at the Viterbi decoder output are dispersed in such a manner that the RS symbols at the outer decoder input are randomized sufficiently. This randomization can be achieved by interleaving [15].

In the (255, 223) RS code, each code word contains 255 symbols, and each symbol contains 8 bits. These symbols are grouped into frames. The frames, together, form a block or format. Figure 2 shows an interleaving scheme for the RS outer coding scheme. The numbers used in this figure are for illustration purposes only.

To achieve interleaving, the information and parity symbols are transmitted column-by-column from left-to-right and each column from top-to-bottom. As a result, a bursty error event of the Viterbi decoder will tend to affect only one symbol of each code word provided the number of rows in each interleaving array is sufficiently high. This number is called the interleaving depth.

The standard RS interleaving depths used for deep-space probes are less than or equal to five [1]. As a consequence, a chip was designed which is capable of being programmed. The interleaving depth can be changed from one to five at the user's convenience.

III. A Single VLSI Chip of a (255,223) RS Encoder With Interleaver

Berlekamp's bit-serial multiplication algorithm for a (255, 223) RS-encoder over $GF(2^8)$ is presented in [7] and [8] (also see M. Perlman and J. J. Lee "Reed-Solomon Encoders-Conventional Versus Berlekamp's Architecture," JPL Internal Document, No. 3610-81-119ISMP, dated July, 1981). The block diagram of the (255, 223) RS encoder with programmable interleaver is exhibited here in Fig. 3.

In Fig. 3, one observes that the circuit is divided into five units: the Product unit, Remainder and Interleaver unit, Quotient unit, I/O unit, and Control Unit. The use of each unit is explained in detail in [8]. However, the Remainder and Interleaver unit is different from that in [8]. This is due to the fact that the interleaver is included in this design, while in [8], no such capability was available.

The function of the Remainder and Interleaver unit is discussed in detail in what follows. Figure 4 shows the block diagram of the Remainder and Interleaver unit. The Remainder and Interleaver unit is used to store the coefficients of the remainder during the division process. This unit also performs the interleaving operation.

In Fig. 4, $S_{i,j}$'s for $0 \leqslant i \leqslant 30$, $1 \leqslant j \leqslant 5$ are 8-bit shift registers. The addition used in the circuit is a modulo 2 addition or Exclusive-OR operation.

The "Turn" and "No-turn" signals are used to program the interleaving depth and the "No-turn" signals are the logical complement of the corresponding "Turn" signals. For example, if "Turn 2" equals 1 and all other "Turn" signals equal 0, then obviously signal "No-turn 2" will equal 0 and all other "No-turn" signals will equal 1. These will turn transistors T_2, T_3, T_6, T_8, T_9 and transistors in the corresponding positions in Fig. 2 on. Also, transistors T_1, T_4, T_5, T_7, T_{10}, T_{11}, T_{12} and their corresponding transistors in Fig. 2 will be turned off. Therefore, data can be transferred from registers $S_{i,1}$'s to $S_{i,2}$'s for $0 \leqslant i \leqslant 30$.

The outputs of registers $S_{i,2}$'s, for $0 \leqslant i \leqslant 30$, are sent to the inputs of modulo 2 adders by bus lines L_i's, for $1 \leqslant i \leqslant 31$. Since transistor T_4 and transistors in its corresponding positions in Fig. 4 are off, outputs of $S_{i,2}$'s can not be sent to $S_{i,3}$'s, for $0 \leqslant i \leqslant 30$, which means only a depth of 2 interleaving operation is allowed in this manner. The depths of 3, 4 or 5 of interleaving can be carried out similarly.

An overall block diagram of the chip is shown in Fig. 5. In Fig. 5, V_{DD} and GND are power pins. The signals ϕ_1, and ϕ_2 are the two phases of a system clock. The information symbols are fed into the chip serially through the data-in pin, DIN.

Similarly, the encoded code word is transmitted out of the chip sequentially from the data-out pin, DOUT.

The control signal, SL, is set to 1 (logic 1) when the information symbols are loaded into the chip. After this, SL is set to 0. The control signal "START" resets a 3-bit word counter in the chip before the encoding process begins. The "Turn" signals are used to program the interleaving depth.

The entire chip was simulated on a general purpose computer using ESIM (a logic level simulation program) [9] and SPICE (a transistor level circuit simulation program) [10]. The layout of this chip was accomplished using the program CAESAR [12]. LYRA [12] was used to check the resulting layout against a set of geometric rules supplied by the fabricator. Timing simulation was accomplished using CRYSTAL [14].

This circuit comprises about 10,000 transistors. It was fabricated using the MOSIS service [13]. The technology used is $4\,\mu m$ NMOS. The layout of this encoder is shown in Fig. 6. The chip was successfully tested and the maximum clock frequency is about 1.5 MHz. The operating speed of this chip is limited mainly by the long clock lines associate with the two-phase clocks used in the dynamic shift registers and there are more than 1250 dynamic registers used on this chip. The chip area is about $4800 \times 3220 \ \mu m^2$. The power consumption at the maximum clock frequency is about 300 mW.

References

[1] "Recommendation for Space Data System Standards: Telemetry Channel Coding," (Blue Book), Consulative Committee for Space Data Systems, CCSDS Secretariat, Communications and Data Systems Division, Code TS, NASA, Washington, D.C., May 1984.

[2] R. L. Miller, L. J. Deutsch and S. A. Butman, "On the Error Statistics of Viterbi Decoding and the Performance of Concatenated Codes," *JPL Publication, 81-9*, Jet Propulsion Laboratory, Pasadena, California, pp. 33-39, September 1, 1981.

[3] R. F. Rice, "Some Practical Universal Noiseless Coding Techniques," *JPL Publication, 79-22*, Jet Propulsion Laboratory, Pasadena, California, March 15, 1979.

[4] R. F. Rice, "End-To-End Imaging Information Rate Advantages of Various Alternative Communication Systems," *JPL Publication, 82-61*, Jet Propulsion Laboratory, Pasadena, California, September 1, 1982.

[5] W. W. Peterson and E. J. Weldon *Error-Correcting Codes*, Cambridge: MIT Press, 1972.

[6] E. R. Berlekamp, "Bit-Serial Reed-Solomon Encoders," *IEEE Trans. on Information Theory*, vol. IT-28, No. 6, pp. 869-874, November 1982.

[7] I. S. Hsu, L. J. Deutsch, T. K. Truong, and I. S. Reed, "A VLSI Single Chip (255, 223) Reed-Solomon Encoder," *TDA Progress Report 42-83*, vol. July–September 1985, Jet Propulsion Laboratory, Pasadena, California, pp. 51-56, November 15, 1985.

[8] I. S. Hsu, I. S. Reed, T. K. Truong, K. Wang, C. S. Yeh, and L. J. Deutsch, "The VLSI Implementation of a Reed-Solomon Encoder Using Berlekamp's Bit-Serial Multiplier Algorithm," *IEEE Trans. on Computers*, Vol. C-33, No. 10, pp. 906-911, October 1984.

[9] C. Terman, "ESIM — An Event Driven Simulator," *Documentation of 1983 VLSI Tools*, Computer Science Division, Univerisity of California, Berkeley, California, 1983.

[10] L. W. Negal and D. O. Pederson, "SPICE — Simulation Program with Integrated Circuit Emphasis," Memorandum No. ERL-4382, Electronic Research Laboratory, University of California, Berkeley, April, 1973.

[11] J. Ousterhout, "CAESAR — Editing VLSI Circuit with CAESAR," *Documentation of 1983 VLSI Tools*, Computer Science Division, University of California, Berkeley, California, 1983.

[12] J. Ousterhout, "LYRA — A Design Rule Checker," *Documentation of 1983 VLSI Tools*, Computer Science Division, University of California, Berkeley, California, 1983.

[13] MOSIS Project, "The MOSIS System (what it is and how to use it)," Information Science Institute, University of Southern California, Publication ISI/TM-84-128, Marina Del Rey, California, 1984.

[14] J. Ousterhout, "Using Crystal for Timing Analysis," *Documentation of 1983 VLSI Tools*, Computer Science Division, University of California, Berkeley, California, 1983.

[15] J. L. Ramsey, "Realization of Optimum Interleavers," *IEEE Trans. on Information Theory*, vol. IT-16, pp. 338-345, May 1970.
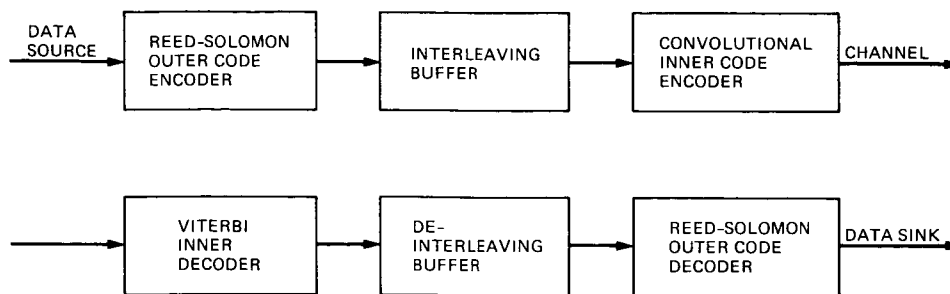
Fig. 1. A concatenated coding system

Fig. 2. An interleaving scheme for the RS outer coding scheme
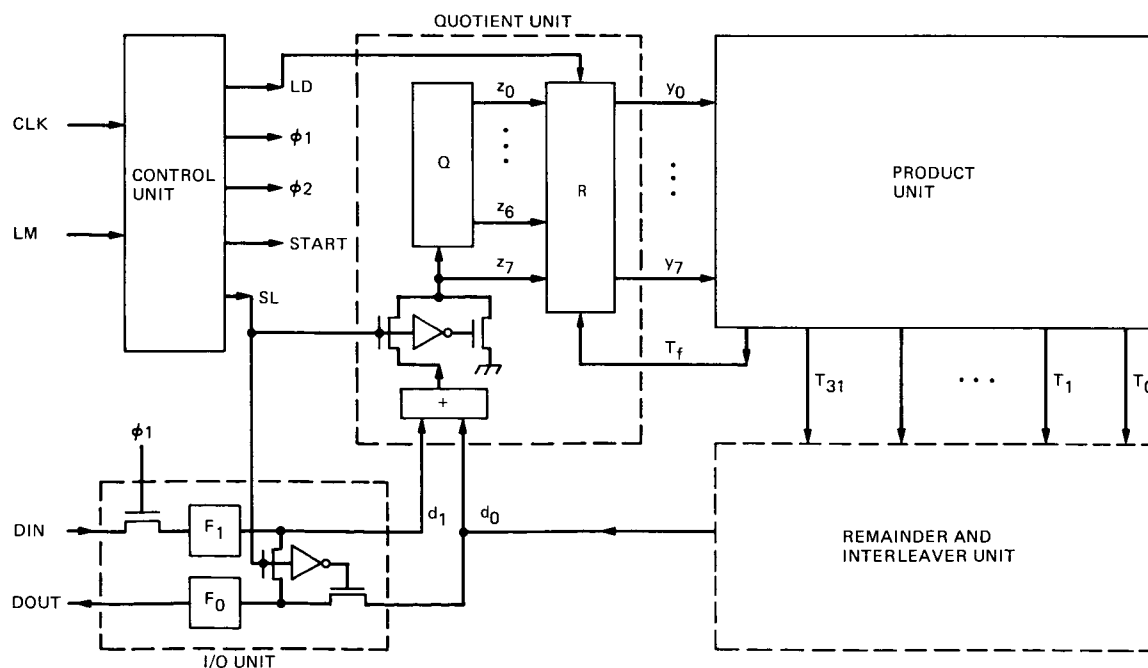
Fig. 3. Block diagram of the (255,223) RS encoder
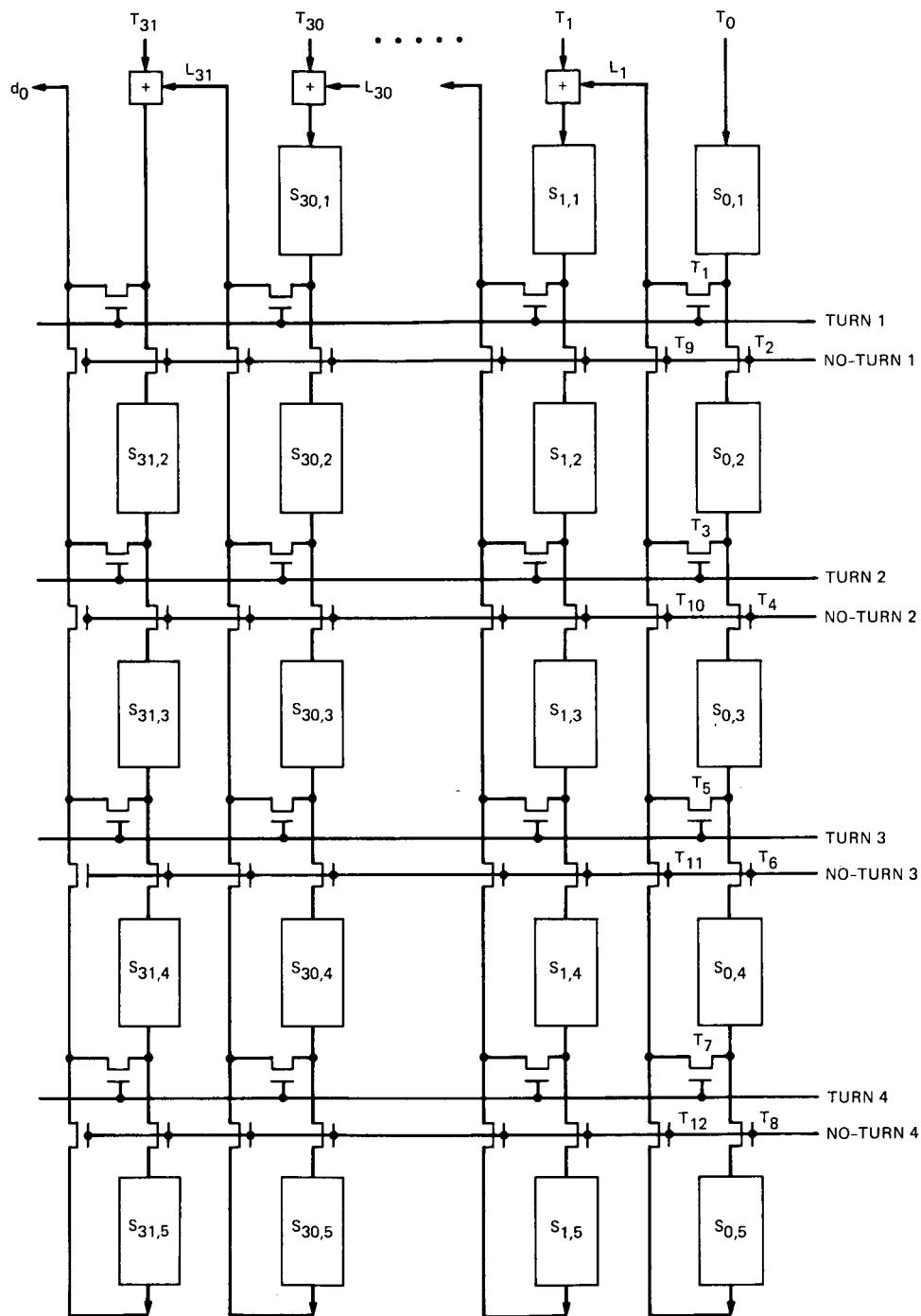
Fig. 4. The block diagram of the remainder and interleaver unit
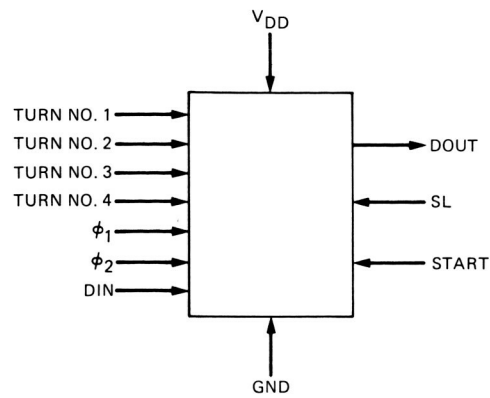
Fig. 5. The symbolic diagram of a (255,223) RS encoder chip
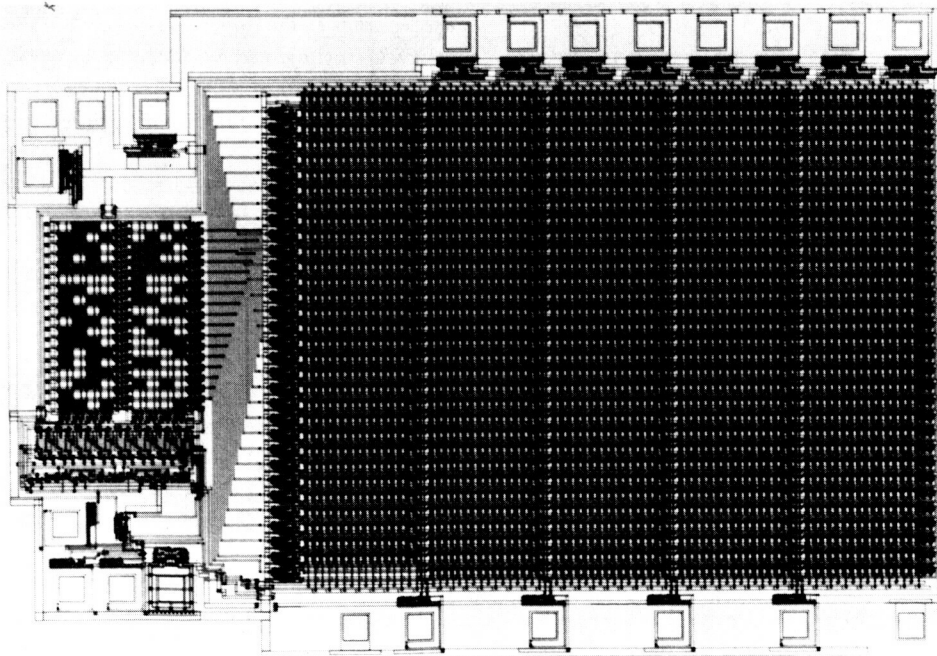
Fig. 6. Layout of the (255,223) RS encoder with interleaver chip

DSN Advanced Receiver: Breadboard Description and Test Results

D. H. Brown and W. J. Hurd
Communications Systems Research Section

A breadborad Advanced Receiver for use in the Deep Space Network has been designed, built, and tested in the laboratory. Field testing was also performed during Voyager Uranaus encounter at DSS-13. The development of the breadboard is intended to lead towards implementation of the new receiver throughout the network. In this article, the receiver is described on a functional level and then in terms of more specific hardware and software architecture. The results of performance tests in the laboratory and in the field are given. Finally, there is a discussion of suggested improvements for the next phase of development.

I. Introduction

The advent of high speed digital signal processing hardware over the last few years has enabled the application of digital solutions to classically analog problems. This, in many cases, has allowed for increased performance, while reducing cost and maintenance requirements. In the area of communications, signals can now be digitized and processed at rates high enough to allow for wide signal bandwidths, such as those required in communication systems found in the Deep Space Network (DSN). The Advanced Receiver (ARX) has been designed for the DSN and uses these advanced digital technologies as well as certain modern communication theory results, such as sideband-aided carrier tracking, to achieve improved performance over existing analog receivers. The theoretical background on the ARX has been well documented elsewhere [1-14]. The goal of the ARX project is to develop a receiver for implementation throughout the DSN. A breadboard ARX has been built and tested.

A. Receiver Description

The ARX is a hybrid analog/digital receiver which uses intermediate frequency sampling and digital phase locked loops to perform carrier tracking, subcarrier tracking, and symbol synchronization. It has been designed to avoid certain inherent problems associated with analog implementations such as DC offsets in mixers and amplifiers, and the need for precise RF calibration and adjustment. In addition, the digital system allows for more flexibility and increased reliability while reducing cost and space requirements.

Figure 1 shows the ARX broken into functional blocks. The receiver uses the open loop IF signal at 53 MHz from the RF front end and performs all subsequent processing through symbol detection. In the IF assembly, the carrier phase locked loop is locked to a submultiple of the sampling rate, as described in section IIA, and then the signal is digitized. All further processing is digital. The receiver performs the carrier

tracking functions currently handled in the Deep Space Stations by the Block III and Block IV receivers, in addition to the subcarrier tracking and symbol synchronization functions of the baseband assembly (BBA). The ability to fit all of the signal processing into one chassis reduces the number of interfaces between subsystems and thereby increases reliability. It also greatly simplifies the implementation of sideband aided and fully suppressed carrier tracking, since the carrier, the subcarrier, and the symbols are processed in the same assembly.

B. Scope of Article

This article describes the design, development, and testing of the advanced receiver. This includes theoretical concerns, hardware and software design, and the results of tests in the laboratory and in the field. It is shown that the receiver performance compares well with expected results in all areas. In some areas, test results suggest improvements which could be made.

II. Breadboard System Description

The breadboard ARX consists of three modules: an intermediate frequency assembly (IFA), a signal processing assembly (SPA), and a test signal assembly (TSA). The IFA performs intermediate frequency sampling, and serves as the point of closure for the carrier and symbol loops. The SPA contains all of the digital signal processing hardware and software which is necessary to operate the three loops. The TSA uses built-in fixed frequency oscillators or externally supplied reference frequencies to generate IF test signals. A block diagram is shown in Fig. 2.

A. Intermediate Frequency Assembly

The IFA interfaces the receiver to the station. Its block diagram is given in Fig. 3. The input to this assembly is an IF signal which has been open loop down converted to approximately 53 MHz ±0.5 MHz. The signal is then bandpass filtered before passing through a total power automatic gain control (AGC). Then the carrier loop is closed by mixing the output of the AGC amplifier with the carrier reference. The carrier reference signal is produced by mixing a constant 46.25 MHz signal with the output of the carrier loop numerically controlled oscillator (NCO), and has a nominal resulting value of 48 MHz. After the AGC output is mixed with the carrier reference, it is filtered and digitized by the A/D. The clock input to the A/D is the sum of frequencies of a fixed 18.0 MHz reference and the symbol synchronization loop NCO. It has a nominal value of 20 MHz and serves to close the symbol synchronization loop. The carrier and symbol loops are linked in such a way that the received carrier frequency is phase

locked to exactly 1/4 of the A/D sampling rate, and there are a constant integer number of samples per symbol.

This sampling process is known as intermediate frequency (IF) sampling [1]. The carrier is not demodulated to analog baseband for phase detection, but instead is phase locked to a known reference before being digitized, in this case one quarter of the sampling rate. Demodulation and phase detection are done digitially. This technique removes the effect of any DC bias in the A/D converter, since the DC component will be translated out of band when the signal is digitally mixed to baseband. Locking to a multiple of the symbol rate, known as synchronous IF sampling, has the added advantage of easing the carrier demodulator implementation (see section III), though problems may arise at low signal-to-noise ratio (SNR) due to the A/D clock coupling into the signal path (see section VIII).

B. Signal Processing Assembly (SPA)

The SPA contains the signal processing hardware and software. Figure 4 shows the SPA in block diagram form and Fig. 5 shows the signal processing hardware in more detail. The SPA performs the operations which implement the phase detectors and loop filters for the carrier, subcarrier and symbol loops. It also contains hardware and software for fast acquisition and signal parameter estimation.

1. **Residual carrier phase locked loop.** Residual carrier phase detection is accomplished using the quadrature (Q)-channel samples. The phase detector output is the sum of some fixed number, N, of consecutive Q-channel samples. A complete mathematical analysis is given in [1]. This summation imposes a low pass filter operation on the channel with bandwidth determined by the number of samples in the sum. The effect of this filtering operation can be assumed to be negligible as long as the effective filter bandwidth is wide compared to the bandwidth of the carrier phase locked loop.

The gain at the output of the hardware phase detector is a function of the number of Q-channel samples in the sum, the square root of the power in the carrier, and any hardware scaling constants. This phase detector output is then passed to a microprocessor which implements type II and type III loop filters as described in [2].

Carrier amplitude is estimated by summing the inphase (I)-channel samples over the same time interval as the carrier phase detector. The signal is further summed in software and then scaled to produce the estimate.

2. **Subcarrier phase locked loop.** The subcarrier phase detection and synchronization is done by employing an optimum Costas loop. A complete mathematical analysis is

given in [1]. The carrier Q samples are multiplied in the two arms of the Costas loop by phase quadrature square wave reference signals at the subcarrier frequency. The products in the two arms of the Costas loop are then summed over one symbol time to implement matched filter detection. These phase quadrature symbol time sums are multiplied together and summed over a longer interval to produce the phase detector output. The subcarrier phase detector gain is given by the number of terms in the phase detector sum, the hardware gain factors, and the ratio of data power to noise spectral density. As for the carrier loop, the microprocessor implements type II or type III loop filters.

3. Sideband-aided carrier tracking. The Advanced Receiver also has the ability to perform sideband-aided carrier tracking after subcarrier lock is achieved. In this scheme, a Costas type phase detector is implemented for carrier tracking by adding a third arm, with carrier inphase and subcarrier inphase. The other arm of the carrier Costas loop is carrier quadrature, subcarrier inphase. The output of the carrier Costas phase detector is added to the output of the residual carrier phase detector with appropriate weighting [1].

4. Symbol synchronization loop. A transition tracking symbol synchronization loop is used, as described in [18]. Symbol phase detection is accomplished by summing across symbol transition windows. The summation is multiplied by the transition direction (-1, 0, +1) and then these products are summed over a longer interval. The width of the window is selectable from software.

Detector gains are given by the hardware gains and the data signal level. The gain does not depend on the window width, provided the symbol transition is within the window. The phase detector output is filtered in a type II or type III loop as above.

5. SNR and signal parameter estimation. Integrated symbols are used to estimate symbol SNR by applying the split symbol SNR estimator as described in [19] for the Baseband Assembly Demodulation Synchronization Assembly. The symbol squared and early-late products are averaged in hardware and then combined in software to produce the estimate.

The SPA produces estimates of signal parameters based on observed quantities measured during signal processing. Parameters measured include carrier power to noise spectral density (P_c/N_0), data power to noise spectral density (P_d/N_0), and steady state carrier phase error (ϕ_{ss}).

6. Fast acquisition. The SPA also performs signal processing for fast acquisition. Fast acquisition is implemented by doing an FFT on the complex I and Q pairs at the output of

the carrier phase detector. A sinusoid at the output of the phase detector indicates a frequency difference between the input carrier frequency and the mixing reference. The frequency of this sinusoid is then fed back as a correction to the initial prediction of carrier frequency.

C. The Test Signal Assembly (TSA)

The test signal assembly provides modulated signals for test and evaluation of the advanced receiver and is shown in block diagram form in Fig. 6. The reference frequencies for the test assembly can be generated by internal oscillators which supply fixed frequencies or by external synthesizers. An internal noise generator injects noise into the signal. Signal to noise ratios and modulation indices are controlled by attenuators for the carrier, data and noise channels. The test assembly uses three input frequencies, a carrier, a subcarrier and a symbol clock, to form a residual carrier signal biphase modulated with a square wave subcarrier. The TSA can also produce direct carrier modulated signals and Manchester coded signals. The data can be either the data clock or a repetition of a 1023-bit-length pseudonoise (PN) sequence that is generated in the TSA.

The internal crystal oscillators are tuned to produce a Voyager II type signal. The test carrier frequency is 53 MHz, the nominal down-converted down link frequency. The subcarrier is at 360 kHz and the symbol rate is 43.2 ksps. This configuration is used in the field when no external synthesizers are available.

III. Signal Processing Hardware

The signal processing assembly contains digital signal processing, control, and system hardware in a Multibus I enclosure. The boards in the Multibus chassis are:

(1) Intel SBC–8614 Single Board Computer (SBC)

(2) Array Processor

(3) 512K RAM Card

(4) Serial I/O Card

(5) Disk Controller Card

(6) Signal Processing (SP) Board

(7) Timing and Control (T&C) Board

(8) Two Numerically Controlled Oscillators (NCOs)

In addition, there is a display monitor for operator interface and a dual floppy disk drive for program storage and data logging. The CRT, disk drives, and the RAM, I/O, and disk controller cards fall into the category of system hardware

and are used for monitor and control of the breadboard ARX. They are not fundamental to receiver operation.

The signal path through the SPA is shown in a block diagram in Fig. 5. The digitized signal from the IF assembly is fed to the timing and control board, where it passes through a complex demodulator producing an I channel and a Q channel. The I and Q data and timing signals then go to the signal processing board and into a bank of multiply-accumulate chips (MACs) which produce carrier, subcarrier, and symbol phase error signals and signal statistics. The phase detector outputs are input to the SBC which implements the three loop filters. The filter outputs are the control signals that drive the carrier, subcarrier, and symbol NCOs, and close each of the loops. The SBC also processes signal statistics to produce estimates of signal parameters. In the fast acquisition mode, the SBC passes I and Q channel values to the FFT processor and processes the resulting transforms to obtain frequency estimates.

A. Sampling and Carrier Demodulation

Synchronous IF sampling allows the T&C board to perform the complex carrier demodulation without the use of a multiplier. In the synchronous IF sampling scheme, the digital demodulating frequency is identically 1/4 of the sampling rate. Complex demodulation requires quadrature references. These are easily obtained by recognizing that the sine and cosine reference signals have only four values per cycle, since there are only four samples per cycle of input carrier. The sine and cosine arguments can then be chosen to be multiples of $\pi/2$ radians, which results in the reference signal taking on values from the repeating stream $(\ldots 0, 1, 0, -1 \ldots)$. Thus in this special case, demultiplexing into odd and even samples and then multiplying alternately by +1 and -1 is equivalent to complex demodulation followed by the summing of every two consecutive samples in each channel. It should be noted that the summation of consecutive samples is valid only when the phase information is narrow band in relation to the sampling frequency. The summation is actually a crude low pass filter operation, which could introduce amplitude distortion, with a normalized frequency transfer function of the form [20]

$$H(v) = \left(\frac{1}{N}\right) \left[\frac{\sin\left(Nv\,\frac{\pi}{2}\right)}{\sin\left(v\,\frac{\pi}{2}\right)}\right]$$

where

N = number of terms in the sum

v = normalized frequency = $2f/f_s$

B. Timing and Control

Multiply-accumulate chips (MACs) are used for subcarrier demodulation, symbol integration, phase error accumulation over fast (carrier) and slow (subcarrier and symbol) loop filter update periods, and SNR estimation. The accumulation period for each of these MACs is controlled by a series of counters on the T&C board. These counters are loaded from software computed values during the hardware initialization routine.

C. Signal Processing

There are 12 MACs on the signal processing board which perform the necessary operations for tracking and data detection. In addition, the integrated symbol values are passed to an external device for decoding or other further processing. The MACs and the signals they produce are shown in Fig. 5. Seven signals are used by the SBC, and five intermediate values are used only by the SP board. Since the signals these devices produce are the key outputs of the signal processing hardware, they are described below.

(1) RCE is the sum of Q-channel samples over one carrier update period and is used as the residual carrier phase error signal.

(2) AMP is the sum of I-channel samples over one carrier update period and is used as a measure of carrier amplitude.

(3) DCE is the output of a carrier Costas-type phase detector formed by the product of the inphase carrier and inphase subcarrier channels, summed over one carrier update period and is used as the data aided carrier phase error signal. A weighted sum of RCE and DCE is the input to the carrier loop filter.

(4) SCE is the subcarrier Costas loop phase output. First, carrier Q-channel samples are multiplied by subcarrier inphase and quadrature square wave references, and the products are summed over one symbol time to form the matched arm filter outputs. Then the product of these channels is taken and summed over one subcarrier update period to form the subcarrier phase error signal.

(5) SSE is the symbol synchronization loop phase output. It is formed by summing carrier Q-channel samples across a symbol boundary and multiplying this sum by the output of a transition detector [18], and then summing this over several symbols. The width of the summation window around the boundary is a software selectable fraction of one symbol time. When the phase error is small and there is a transition, the sum across that transition is proportional to the magnitude of the

phase error, and its sign is given by the product of the sign of the sum and the sign of the transition.

(6) PWR and MSQ are the two signals used to compute the split symbol estimate [19] of the ratio of symbol energy to noise density (E_s/N_0). PWR is formed by squaring the sum of the samples in one symbol, and summing these squares over one subcarrier update period. MSQ is formed by multiplying the sum of the samples in the first half of a symbol by the sum of the samples in the second half of that symbol, and summing this product over one subcarrier update period. These values are combined in the software to produce the estimate of E_s/N_0.

The above signals are read by the SBC. The RCE, DCE, SCE, and SSE signals are all input to the digital loop filters implemented by the SBC. The output of the carrier and symbol synchronization filters go to the NCOs. The NCOs in turn output analog signals to the IF assembly. The output of the subcarrier filter goes to the subcarrier NCO, which is located on the T&C board. The RCE signal is also combined with AMP to produce an estimate of carrier phase angle. The SNR and PWR signals are combined to form the estimate of E_s/N_0. The following signals are intermediate results used only by the SP board.

(7) QSMODE is the summation of the inphase subcarrier channel over one symbol time. The inphase subcarrier channel is formed by taking the product of the carrier quadrature channel and the internally generated sine phase subcarrier reference. It is used as the soft output symbol value. It is also used by the SP board for transition detection, as the inphase arm of the subcarrier Costas loop, as the quadrature arm of the sideband aided carrier loop, and is squared to form PWR.

(8) QCMODE is the summation of the quadrature subcarrier channel over one symbol time. The quadrature subcarrier channel is formed by taking the product of the carrier quadrature channel and the internally generated cosine phase subcarrier reference. The QCMODE signal is used as the quadrature arm of the subcarrier Costas loop.

(9) ISMODE is the summation of the product of the carrier inphase and internally generated sin phase subcarrier reference, over one symbol time. It is used as the inphase arm of the sideband aided carrier loop.

(10) DQSMDM is the summation of the inphase subcarrier channel across the symbol transition over the software selected window width. It is used to form SSE.

(11) DQSH is the summation of the inphase subcarrier channel over one-half of one symbol time. It is used to form MSQ.

D. Scaling

The output detected symbol value is the summation of the inphase subcarrier channel over one symbol time and can be written as

$$D(nT_s) = \sum_{k=nN}^{((n+1)N)-1} (SCALE * [2^{2*MODE}]$$

$$* \sin [\omega_{sc} kT + \hat{\phi}] * q [kT])$$

where SCALE and MODE are software selectable scaling constants. This is the output of the subcarrier inphase arm MAC. When E_s/N_0 is greater than -3 dB, SCALE and MODE are set such that the mean value of the output data is 21.5 binary units for compatibility with current telemetry processing equipment. At E_s/N_0 = -3 dB, the noise standard deviation is equal to the signal mean. When E_s/N_0 is less than -3 dB, the noise dominates, and summation overflow could occur. Therefore, at SNRs below -3 dB, the scaling factors are chosen so that the standard deviation of the noise is 21.5.

The values assigned to MODE and SCALE are computed by the SBC based on *a priori* signal parameters. The value of MODE is determined by the symbol rate. If the symbol rate is less than 1 ksps then it is set to one, otherwise it is set to four. This is to prevent overflow in the accumulators at low symbol rates. Once MODE is fixed, SCALE is calculated as above and quantized to one of sixteen levels. The SCALE value is introduced into the signal stream through the subcarrier reference signal. The output of the NCO that produces the sine and cosine waveforms necessary for the subcarrier Costas loop is modified by two PROMs. These PROMs take the sine and cosine amplitudes, the SCALE value, and four control signals to produce the references. The control signals select between sine wave or square wave subcarriers, and non-return-to-zero or Manchester modulation, and can also select signals for testing.

E. Fast Acquisition Processing

An array processor is used to perform FFT processing for fast acquisition. When in the fast acquisition mode, the SBC stores consecutive values of RCE (carrier Q channel) and AMP (carrier I channel). The AMP and RCE signals are combined to form the complex value

$$X(t) = RCE + j \; AMP$$

After 128 values of $X(t)$ have been collected, the SBC passes the location of the data in shared memory to the array processor, which computes the magnitude squared of the complex FFT. This process is repeated four times and the power spectra are accumulated. The array processor then does a "peak pick" which is a procedure which returns the number of the FFT bin which had the highest magnitude response. From this number, an estimate of the frequency difference between the actual input signal and the carrier reference is derived. This offset is added to the initial carrier reference frequency and the loops are enabled. The range of frequencies covered by the FFT is equal to the carrier loop update rate, and is divided into 128 frequency bins.

IV. Signal Processing Software

Loop filter implementation and overall control are orchestrated by the Advanced Receiver software. The operation is divided between real time interrupt driven routines to perform the loop filter operations and a background process that communicates with the user and does low rate computations.

A. Environment

The Advanced Receiver software was developed on an 8086/87 processor based system running under the CP/M operating system. The majority of the of code (4000 lines) is written in Pascal with the remaining code in assembly language. The software was developed on the target system, which proved advantageous in the research and development phase. This approach is not recommended for the implementation phase, where the use of separate reusable development systems would be a more cost effective allocation of resources.

B. Structure

The Advanced Receiver software maintains two key run time processes: loop filtering and user interface. The loop filter process is timing critical and therefore is the higher priority or foreground process. The user interface is the lower priority background process. In addition, the software controls the hardware and software initialization routines.

The loop filter processing is an interrupt driven foreground process. The phase detector outputs, which are input to the loop filters, are generated on the signal processing board. When phase data are ready, an interrupt is generated by the signal processing board and one of the interrupt service routines responds by reading and processing the new data. The interrupt service routines are written in assembly language to increase speed. There are two interrupt routines; one that services the carrier loop only, and one that serves all three loops. This enables the carrier loop filter to be updated more frequently

and enables wider bandwidth carrier loops. After an interrupt has been serviced, program control returns to the background process.

The background process handles the calculation and display of system parameters and control of the receiver configuration. Menu selectable displays allow the user to select loop configurations and input *a priori* signal information or predicts. While the receiver is running, there are menu selectable displays for each loop's performance and an overall system performance display.

C. Dynamic Filter Modification

An important feature of the software architecture is the ability to dynamically change loop parameters, or change filters "on the fly." In other words, it is possible to change loop bandwidths, loop types, and damping coefficients without losing lock. This is possible due to the interrupt driven nature of the loop filters and the careful implementation of the filter equations. This is important since lock acquisition can be accomplished with wide bandwidth type II loops, and then the loops can be changed to narrow bandwidth type III loops for low phase jitter tracking.

The interrupt driven nature of the code helps to facilitate dynamic filter modification. When the operator requests a change in any or all of the tracking loop filter bandwidths, the background process begins to compute new filter coefficients. Meanwhile, the foreground process continues to service the interrupts and to process the incoming data using the current loop parameters. Once the new coefficients have been computed and stored into memory, the address pointer to the location of the filter coefficients is toggled such that the next time an interrupt service routine is called, it will use the most recently computed coefficients.

The loop filter equations must be implemented in such a way that avoids sharp discontinuities in filter output when loop parameters are changed. The digital transfer function of the loop filter used is of the form [2]

$$F(z) = G_1 + G_2 \left(\frac{Tz}{[z-1]} \right) + G_3 \left(\frac{T^2 z^2}{[z-1]} \right)$$

where G_1, G_2, and G_3 are filter coefficients and T is the sampling period. The second and third terms represent scaled single and double integrators in the z domain respectively. The second term is implemented as the sum of all previous inputs and the third term as the sum of all previous sums of inputs. The filter output can be written as

$$y(k) = G_1 x(k) + G_2 \sum_{i=0}^{k} x(i) + G_3 \sum_{i=0}^{k} \sum_{j=0}^{i} x(j)$$

Intuitively, the first term can be viewed as the phase correction term, the second as the frequency (velocity) correction term, and the third as the frequency rate (acceleration) correction term. If the gain coefficients vary with time, than a change in these coefficients should not perturb the previous corrections in phase, frequency and frequency rate. In order to account for the time varying nature of the loop coefficients, these coefficients must be brought inside the summations as below

$$y(k) = G_{1k} x(k) + \sum_{i=0}^{k} \left[G_{2i} x(i) + \sum_{j=0}^{i} G_{3j} x(j) \right]$$

where the second subscript on the G's indicates time dependance.

V. Receiver Operation

The ARX breadboard was designed as a research tool to validate ARX concepts. While it is not designed for use by operators in the field, its menu driven structure makes using the receiver simple and easy to learn. The normal operating mode would correspond to the maintenance mode of an implemented receiver whose prime user interface would be the Link Monitor and Control (LMC).

A. Breadboard Receiver

The current configuration of the ARX is designed for direct operator control, as this most easily lends itself to development and testing. All monitor and control functions are passed on an RS232 connection between the receiver and a CRT monitor. The operator enters signal characteristics and tracking requirements on the keyboard and then observes key performance parameters on the display screen.

The receiver software is fully menu driven. There are three levels of menus. From the main menu, the operator selects from one of these six options:

(1) Review and modify parameters

(2) Run self test

(3) Run real time

(4) Run real time with fast acquisition

(5) Log data

(6) Reinitialize (reinitialization).

At any time, the operator can exit from the main menu to the CP/M operating system. After selecting an activity from the main menu, the operator is presented with the appropriate submenu for that activity. Thus the operation of the receiver is self documented.

The "Review and modify parameters" option is selected when the loop or data parameters are to be changed or examined. Submenus include data specifications, carrier, subcarrier, and symbol loop parameters, and filter update rates. The entire receiver configuration can also be stored onto and recalled from a floppy disk. This allows for the storage of different receiver configurations which can easily be recalled and reloaded.

The "Self test" module runs a built-in hardware self test that is in ROM in the hardware. This module is still under development.

There are two real time tracking options. The first, "Run real time," executes the basic receiver software. This software implements the loop filters, collects and processes statistics on loop performance and signal characteristics, and controls the output of information to the screen.

The second real time tracking option, "Run real time with fast acquisition," executes an FFT on the carrier inphase and quadrature channels to determine the error in initial frequency estimate. This information is then fed back and a new frequency estimate is produced. This estimate is used as the center frequency for the carrier phase lock loop and the loops begin operation as in the "Run real time" option. Lab experimentation has shown that with the fast acquisition utility, carrier lock can be achieved in less than 2 seconds in the presence of Doppler rates in excess of 1 Hz/ sec over a range of ±250 Hz.

The main menu option "Log data" allows the user to toggle a software switch which controls data logging to a floppy disk. When this switch is on, tracking statistics and configuration information are written to a disk for later analysis. Data logging is transparent to the user.

The final option available in the main menu is "Reinitialization." Selecting this option resets and reinitializes all hardware and software. It is equivalent to restarting the program.

B. Operation of ARX for DSN Implementation

Current plans are that the receiver implemented in the DSN will have two distinct operating modes: normal mode and maintenance mode. The receiver will most often be in the normal mode, where it will receive commands from the

station operator via the LMC network. The maintenance mode will be reserved for times when the receiver requires testing, repairs, or modification. The maintenance mode can also be used if there is a failure of the LMC or LMC interface.

The normal mode will include several features that simplify the operation of the receiver. Routine acquisition is envisioned as a two step process. First, radiometric predicts are loaded into the receiver via the LMC. Then the receiver is commanded to acquire downlink. This command initiates an acquisition strategy which includes an FFT frequency search, fast acquisition, lock detection, and automatic bandwidth reduction. The receiver will constantly monitor its own performance. The operator also has full control to set the receiver configuration in a manual acquisition mode. Simple "help" utilities and menu driven options will further simplify operation.

The maintenance mode will facilitate field servicing and allow the receiver to be operated through a maintenance port, bypassing the LMC. This mode will make available diagnostic routines and monitor functions. In the maintenance mode, the receiver will be able to be operated as if from the LMC. In addition, test routines will exercise individual hardware and software blocks, simplifying the trouble shooting process. Access to board level monitor functions will allow the downloading of special test routines, and the loading and testing of new modules of the receiver software.

VI. Laboratory Tests

The Advanced Receiver breadboard has undergone initial testing in the laboratory. Tests have been conducted to determine its tracking and acquisition performance, phase jitter, and phase bias. These tests have proven valuable in giving confidence to initial assumptions and revealing areas in which modifications for the future are indicated.

A. Range of Operation

Tests were done to determine the range of functional operation of the receiver under different configurations. Laboratory results have shown the receiver can track effectively under the following conditions:

Carrier Frequency	53 MHz ±0.5 MHz
Subcarrier Frequency	20 kHz to 960 kHz
Symbol Rate	36 sps to 200 ksps
Symbol SNR	-20 dB to +25 dB

These results are preliminary and do not reflect the full operating range of the receiver. The lower limit on symbol SNR is higher at lower symbol rates due to practical limitations on how narrow the symbol and subcarrier loops can be made. Further tests of operating limits will be determined and published at a later date.

B. Fast Acquisition and Tracking Under Voyager Conditions

Tests were done with the ARX to simulate Voyager II signal characteristics as received at a 26-meter antenna, such as DSS-13 at Goldstone. The signal parameters are tabulated below.

Carrier Frequency	=	X-Band (Open loop downconverted to 53 MHz)
Subcarrier Frequency	=	360 kHz
Symbol Rate	=	43.2 ksps
Modulation Index	=	72 deg.
E_s/N_0	=	-10 dB
Doppler Rate Uncertainty (df_c/dt)	=	1 Hz/s
P_c/N_0	=	26.6 dB-Hz

The Doppler rate uncertainty was simulated by sweeping the carrier frequency synthesizer input to the test signal assembly at the appropriate rate.

Initial acquisition of this signal was achieved with the following receiver configuration.

Carrier Loop

Bandwidth	=	10 Hz
Loop type	=	II

Subcarrier Loop

Bandwidth	=	0.1 Hz
Loop type	=	II

Symbol Sync Loop

Bandwidth	=	0.1 Hz
Loop type	=	II

Using the FFT based fast acquisition scheme, the receiver was able to lock to the above signal and produce good symbol SNR estimates with a better than 99% success probability in less than 20 seconds. This is as fast as can be expected since the SNR estimates are only made once per 10 seconds.

After initial acquisition, the carrier loop parameters were modified to improve performance. In order to reduce phase jitter, the loop bandwidth was reduced from 10 Hz to 3 Hz. There is a limit however, to the minimum amount of bandwidth necessary in a type II loop in the presence of dynamics. The steady state phase error for a type II loop is proportional to the frequency rate divided by the square of the loop bandwidth. Thus, to allow for further bandwidth reduction and thereby improved loop SNR, the carrier loop was changed to a type III loop, which has zero static phase error for constant frequency rate. Table 1 shows the loop SNR and static phase error in the different stages of acquisition. After the type III loop is implemented, the static phase error goes to zero as expected. Then the bandwidth is further reduced to 1 Hz with a resulting loop SNR of 26.6 dB.

C. Swept Acquisition Test

The Advanced Receiver breadboard was tested for its ability to acquire high dynamic carrier signals. These are characterized by Doppler rates that are higher than the current FFT processor could handle without smearing. One hundred trials were performed [10] for three different loop parameter cases, each with an initial frequency offset of ten times the loop bandwidth. The loop bandwidth was set to 10 Hz and the carrier loop SNR was set to 13 dB for each case. Table 2 shows the sweep rate, measured probability of acquisition, and theoretical probability of acquisition for each of the three cases. There is a good level of agreement for cases 1 and 2, using type II loops. The discrepancy between actual and expected results in case 3, where type III loops are used, can be attributed to small DC offsets in the carrier phase detector output, which accumulate quickly in the double integrator of the third order loop.

D. Phase Error Jitter Measurements

Measurements were made on the carrier loop phase jitter in the presence of varying amounts of noise (Rafferty, Wm., "Phase Error Jitter Measurements on the Advanced Receiver Residual Carrier Phase Locked Loop," JPL Internal Document, IOM 331-86.5-117, Jet Propulsion Laboratory, Pasadena, Ca, May 15, 1986). The results were compared to those predicted by standard linear theory with favorable results. Under typical operating conditions, such as those experienced at Voyager II Uranus encounter, the measured phase error variance as a function of loop signal to noise ratio was within 1 dB, worst case, of that predicted by linear theory.

In the simple case of the unmodulated carrier tracking loop, the linear model of the relation of phase error variance, σ_ϕ^2, to loop SNR, SNR_L, is given by

$$\sigma_\phi^2 = 1/SNR_L$$

In Fig. 7, the above function is plotted along with the phase error variance results derived from experimental data. From the figure we see that the carrier phase locked loop agrees well with linear theory. The divergence of the linear theory from the actual measured curve at high SNR is not unexpected due to the presence of a noise floor in the phase locked loop which becomes apparent at high SNR. The ARX carrier loop implementation is in close agreement with the discrete time difference equations when operating in the normal region of loop SNRs, from 10 dB to 30 dB.

E. Phase Bias Measurements

During various tests and operation of the receiver, it has been observed that there is a static phase error at low SNR due to bias in the carrier phase detector output. This is evidenced by the fact that the measured carrier power is sometimes higher when there is a Doppler rate than when there is no Doppler rate. This occurs with a type II loop when the phase error due to Doppler rate cancels the phase error in the phase detector. Further, when the carrier loop is not closed, the mean value of the phase detector output is not zero; instead it is a nonzero value that varies over time and with relative physical positioning of the IFA and the SPA. Various attempts were made to eliminate or reduce the bias. These included adding power supply isolation between the A/D and IF circuits, shielding the A/D converter, and rerouting cables. The bias changed with configuration, but was not substantially reduced. One possible cause of this bias is on the A/D card itself, or even on the conversion chip.

A test was run to determine if the coupling between digital processing and the IF and the A/D circuitry caused the problem. The A/D was tested with a noise input, but without running the normal digital circuitry. A separate test circuit was used to measure the bias, instead of the normal processing. The test setup measures the power at one quarter of the sampling frequency when the input to the A/D is gaussian noise, which is white relative to the bandwidth of the sampling process. A signal at one quarter the sampling rate is periodic in four samples. Thus the amplitude of this component can be measured by mixing the A/D output with a frequency at one-fourth of the sample rate, much in the same way that carrier amplitude is measured in the carrier inphase channel in the receiver. To ease the implementation, only the sign bit was examined and the results were averaged over several seconds to reduce the variance of the noise.

The actual test involved designing a circuit to demultiplex the A/D output into four time sequential channels. The A/D was clocked at 20 MHz and the number of negative A/D outputs for each channel over a 10-second period was then recorded. Analysis of the results showed that the amplitude of

the bias term is in the order of several ten thousandths of a least significant bit, which corresponds to a ratio of interference power to noise spectral density of 5 dB-Hz to 10 dB-Hz. This value becomes significant when tracking very weak signals, such as Pioneer 10 at a 64-m station, with P_c/N_0 approximately 14 dB-Hz. The effect was significant, but not dominant in tracking Voyager from DSS-13, with P_c/N_0 24.4 dB-Hz as discussed in section VII.

VII. Demonstration at Voyager 2 Uranus Encounter

On January 24, 1986 the Advanced Receiver tracked the Voyager 2 spacecraft at Uranus encounter. This field test was performed at DSS-13, Goldstone, California. During the encounter, the receiver locked onto and tracked the residual carrier, subcarrier, and symbol stream. The overall receiver performance met all expectations.

The carrier signal to noise spectral density ratio was typically 24 dB-Hz, with some variation due to changing modulation index and elevation angle. Type III residual carrier phase locked loops with one-sided bandwidths of 1.5 Hz were successfully used to track Doppler rates in excess of 2 Hz/sec with a resultant phase error due to dynamics of less than 0.5 degree. The type III loops have no steady state phase error due to frequency rate (acceleration), and the error due to jerk (the derivative of acceleration) is proportional to the jerk times $(1/B_L)^3$. At Uranus encounter, the maximum predicted steady state phase error due to jerk is less than 0.2 degrees with a 1.5 Hz type III loop. Thus the actual steady state phase error was dominated by the phase detector bias, discussed in the preceding section. A Block IV receiver, operating at minimum bandwidth of $2B_{L0} = 10$ Hz, would have an actual one-sided loop bandwidth of 18 Hz, a static phase error 1.5 degrees at 2 Hz/sec Doppler rate, and a loop SNR of 11 dB. The loop SNR with the ARX operating with a 1.5 Hz loop is 22 dB. Thus the Advanced Receiver achieves a significant increase in loop SNR of about 11 dB.

At Uranus encounter, the ARX also achieved subcarrier lock and symbol synchronization, and produced estimates of symbol SNR. The tracked data rates varied from 25.6 ksps with E_s/N_0 of -7.2 dB to 14.4 ksps with E_s/N_0 of -4.4 dB. In all cases the modulation index was known, so that the relationship between P_c/N_0 was also known. Our estimates of P_c/N_0 and E_s/N_0 were consistent with this relationship to within 0.1 dB. Considering possible uncertainties in modulation index and losses in the symbol and subcarrier loops, our measurements indicate correct performance of the subcarrier demodulator, the symbol synchronizer, and the SNR estimator.

VIII. Possibilities for Future Improvement

Testing of the breadboard ARX and continuing analysis and research has highlighted some areas in which the performance of the receiver could be enhanced.

A. Offset Carrier

The ARX bias problem can be handled in several ways. One way would be to reduce the magnitude of the spurious frequency component at one quarter of the sampling rate by improving the design of the A/D unit, further isolating the sampling clock from the signal path. Though this may be technically possible, the wisdom of such an approach is not clear. One of the traditional problems with analog phase locked loops at low carrier power to noise power ratios is a lack of isolation between the input and reference signals. The only source of in-band spurious components in the ARX digital loop is at the A/D converter. Hence if we can move this component out of band, we have effectively removed the interference without having to increase the analog isolation circuitry.

The problem of generating spurious energy at the carrier frequency can be avoided by offsetting the sampling clock from four times the carrier IF. By offsetting, the sampling clock's subharmonic is moved away from the carrier frequency which will help to assure a high level of isolation in the feedback path. This offset should be selectable, to avoid the possibility of the subcarrier or data being corrupted if the sampling subharmonic happens to fall in band. The main disadvantage to this technique is that demodulation now requires actual complex multiplication at the sampling rate, but this is feasible with currently available VLSI chips.

B. Fixed Sampling Rate

To eliminate jitter in the carrier phase locked loop introduced by insufficient compensation for symbol loop coupling effects in the sampling clock, it is recommended that the sampling rate be fixed and not depend on the symbol loop. This will necessitate the redesign and new analysis of the symbol loop. There will be some loss in performance because there will be a noninteger number of samples per symbol. This loss will be negligible except at very high data rates, which only occur with direct carrier modulation types. The impact of effect at high rates is currently under study.

C. Subcarrier Windowing

Recent results [11] indicate that substantial improvements can be made in subcarrier tracking by windowing the subcarrier reference signal, in a manner similar to windows now used in the ARX for the symbol synchronization loop. Since the cost to do this is minimal and implementation is straightforward, it is suggested that this be done in future systems.

D. Loop Filters

Substantial work has been done recently in loop filter design [2, 5, 8, 9, 12]. Some benefit versus cost tradeoffs need to be done, but changing the form of the loop filters should be considered. The main potential benefits are for wide loop bandwidths, i.e., when the required loop bandwidth approaches the update rate of the loop filter.

E. Smoothing Estimators

Smoothing has been proposed as a method of improving carrier phase estimation [4, 5, 13, 14]. A 5.0 dB to 5.6 dB reduction in carrier phase tracking error can be achieved without narrowing the bandwidth of the phase locked loop. This is very important when the signal is weak and the loop bandwidth cannot be narrowed due to spacecraft Earth dynamics or system instabilities. This situation occurs when using small antennas in an array, or for weak spacecraft like Pioneer 10. Smoothing virtually eliminates radio loss whenever the phase locked loop can maintain lock.

F. Doppler Extractor

In anticipation of requirements for ARX DSN implementation, a digital Doppler extractor will be designed. This will take integrated uplink phase from the exciter and compare it to integrated downlink phase from the ARX to produce an estimate of two-way Doppler. These computations can be performed by the ARX signal processing assembly.

IX. Conclusions

A breadboard Advanced Receiver (ARX) has been built and demonstrated in the laboratory and in the field. It performs carrier tracking, subcarrier tracking, symbol synchronization, and data detection with improved performance over current DSN subsystems. Advanced features include FFT based fast acquisition, sideband aiding, and increased reliability to serve the flight projects of the 1990's.

Acknowledgments

References

[1] R. Sfeir, S. Aguirre, and W. J. Hurd, "Coherent Digital Demodulation of a Residual Carrier Signal Using IF Sampling," *TDA Progress Report 42-78*, vol. April–June 1984, pp. 135–142 Jet Propulsion Laboratory Pasadena, CA, August 15, 1984.

[2] S. Aguirre and W. J. Hurd "Design and Performance of Sampled Data Loops for Subcarrier and Carrier Tracking," *TDA Progress Report 42-79*, vol. July–September 1984, pp. 81–95, Jet Propulsion Laboratory, Pasadena, CA, Nov. 15, 1984.

[3] C. A. Pomalaza-Raez and W. J. Hurd "Improved Carrier Tracking by Smoothing Estimators," *IEEE Transactions on Aerospace and Electronic Systems*, vol. AES-21, no. 5, pp. 610–618, Sept. 1985. Also in *TDA Progress Report 42-79*, vol. July–September 1984, pp. 96–106, Jet Propulsion Laboratory, Pasadena, CA, Nov. 15, 1984.

[4] C. A. Pomalaza-Raez and W. J. Hurd "Carrier Tracking by Smoothing Filter Can Improve Symbol SNR," *IEEE Transactions on Aerospace and Electronic Systems*, vol AES-22, no. 5, pp. 554–558, Sept. 1986. Also in *TDA Progress Report 42-83*, vol. July–September 1985, pp. 57–62, Jet Propulsion Laboratory, Pasadena, CA, Nov. 15, 1985.

[5] R. Kumar and W. J. Hurd "A Class of Optimum Digital Phase Locked Loops for the DSN Advanced Receiver," *TDA Progress Report 42-83*, vol. July–September 1985, pp. 63–80, Jet Propulsion Laboratory, Pasadena, CA, Nov. 15, 1985.

[6] S. Aguirre, "Acquisition Times of Carrier Tracking Sampled Data Loops," *TDA Progress Report 42-84*, vol. October–December 1985, pp. 88–93, Jet Propulsion Laboratory, Pasadena, CA, Feb. 15, 1986.

[7] R. Kumar, "Fast Frequency Acquisition via Adaptive Least Squares Algorithm," *TDA Progress Report 42-85*, vol. January–March 1985, pp. 53–61, Jet Propulsion Laboratory, Pasadena, CA, May 15, 1986.

[8] J. Statman, "A Recursive Solution for a Fading Memory Filter Derived From Kalman Filter Theory," *TDA Progress Report 42-86*, vol. April–June 1986, pp. 70–76, Jet Propulsion Laboratory, Pasadena, CA, May 15, 1986.

[9] J. Statman and W. J. Hurd "An Estimator-Predictor Approach to PLL Loop Filter Design," *TDA Progress Report 42-86*, vol. April–June 1986, pp. 77–89, Jet Propulsion Laboratory, Pasadena, CA, May 15, 1986.

[10] S. Aguirre, D. H. Brown, and W. J. Hurd, "Phase Lock Acquisition for Sampled Data PLL's Using the Sweep Technique," *TDA Progress Report 42-86*, vol. April–June 1986, pp. 95–102, Jet Propulsion Laboratory, Pasadena, CA, May 15, 1986.

[11] W. J. Hurd and S. Aguirre, "A Method to Dramatically Improve Subcarrier Tracking," *TDA Progress Report 42-86*, vol. April–June 1986, pp. 103–110, Jet Propulsion Laboratory, Pasadena, CA, May 15, 1986.

[12] S. Aguirre, W. J. Hurd, R. Kumar, and J. Statman, "A Comparison of Methods for DPLL Loop Filter Design," *TDA Progress Report 42-87*, vol. July–September 1986, pp. 114–124, Jet Propulsion Laboratory, Pasadena, CA, May 15, 1986.

[13] R. Kumar and W. J. Hurd, "Fixed Lag Smoothers for Carrier Phase and Frequency Tracking," IASTED International Symposium on Applied Control and Identification, ACI 86, Los Angeles, CA, Dec. 10-12, 1986.

[14] R. Kumar and W. J. Hurd "Fixed Lag Smoothers for Carrier Phase and Frequency Tracking," *TDA Progress Report 42-89*, vol. January-March 1987, Jet Propulsion Laboratory, Pasadena, CA, May 15, 1987.

[15] W. J. Hurd and T. O. Anderson, "Acquisition Time for Symbol Synchronization for Low SNR Coded Systems," *Space Programs Summary 37-61*, vol. III, pp 57-63, Jet Propulsion Laboratory, Pasadena, CA, Jan. 31, 1970.

[16] W. J. Hurd, et. al., "Intercontinental Antenna Arraying by Symbol Stream Combining at ICE Giacobini-Zinner Encounter," *TDA Progress Report 42-84*, vol. October-December 1985, pp. 220-228, Jet Propulsion Laboratory, Pasadena, CA, Feb. 15, 1986.

[17] W. J. Hurd, et. al., "Antenna Arraying of Voyager Telemetry Signals by Symbol Stream Combining," *TDA Progress Report 42-86*, vol. April-June 1986, pp. 131-142, Jet Propulsion Laboratory, Pasadena, CA, Aug. 15, 1986.

[18] W. J. Hurd and T. O. Anderson, "Digital Transition Tracking Symbol Synchronizer for Low SNR Coded Systems," *IEEE Transactions on Communication Theory*, vol. COM-18, no. 2, pp. 141-147, April 1970.

[19] M. K. Simon and A. Mileant "SNR Estimation for the Baseband Assembly," *TDA Progress Report 42-85*, vol. January-March 1986, pp. 118-126, Jet Propulsion Laboratory, Pasadena, CA, May 15, 1986.

[20] N. Ahmed and T. Natarajan, *Discrete Time Signals and Systems*, Reston Va.: Reston Publishing Co., Inc., 1983.

Table 1. Lab tracking performance test with f = 1 Hz/sec,
E_s/N_0 = −10 dB, P_c/N_0 = 26.6 dB-Hz

Loop bandwidth B_L (Hz)	Loop type	Steady state phase error ϕ_{ss} (deg)	Phase error jitter σ_ϕ (deg)	Loop SNR_L ρ (dB)
10	II	−1.2	8.5	16.6
3	II	−13.5	4.7	21.8
3	III	0	4.7	21.8
1	III	0	2.7	26.6

Table 2. Swept acquisition test with B_{LC} = 10 Hz
P_c/N_0 = 23 dB−Hz

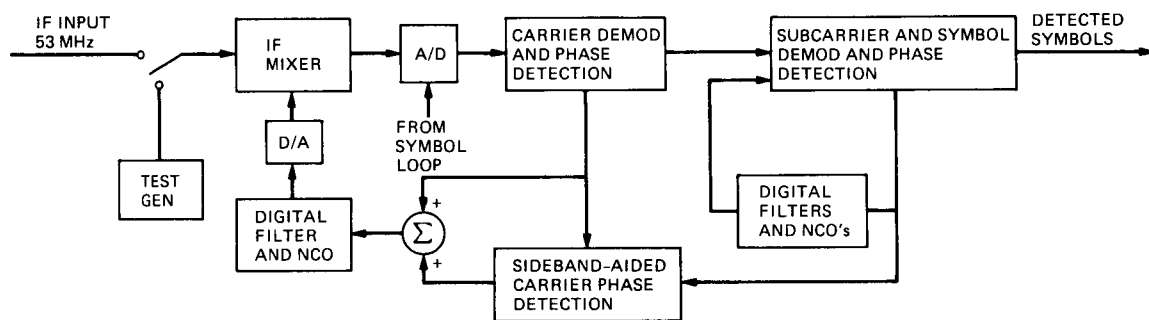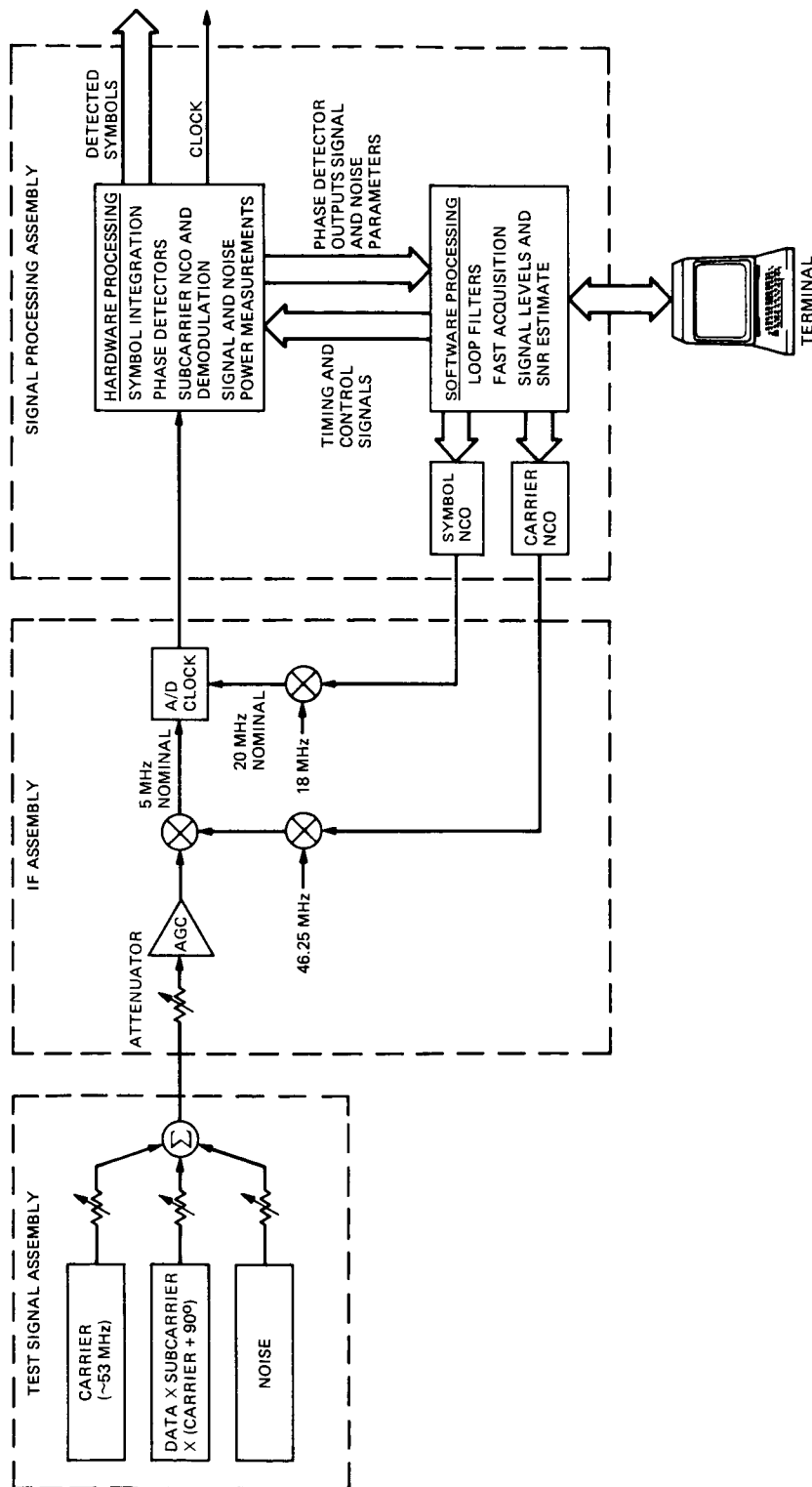| Loop type	Loop parameters		Sweep rate (Hz/s)	Theoretic probability of acquisition	Experimental probability of acquisition
	r	k			
II	2	0	30.4	0.92	0.95
II	4	0	24.8	0.87	0.88
III	4	0.25	20.8	0.82	0.42

Fig. 1. ARX functional block diagram
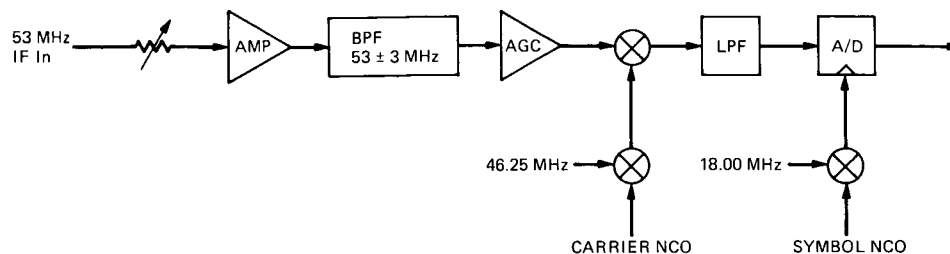
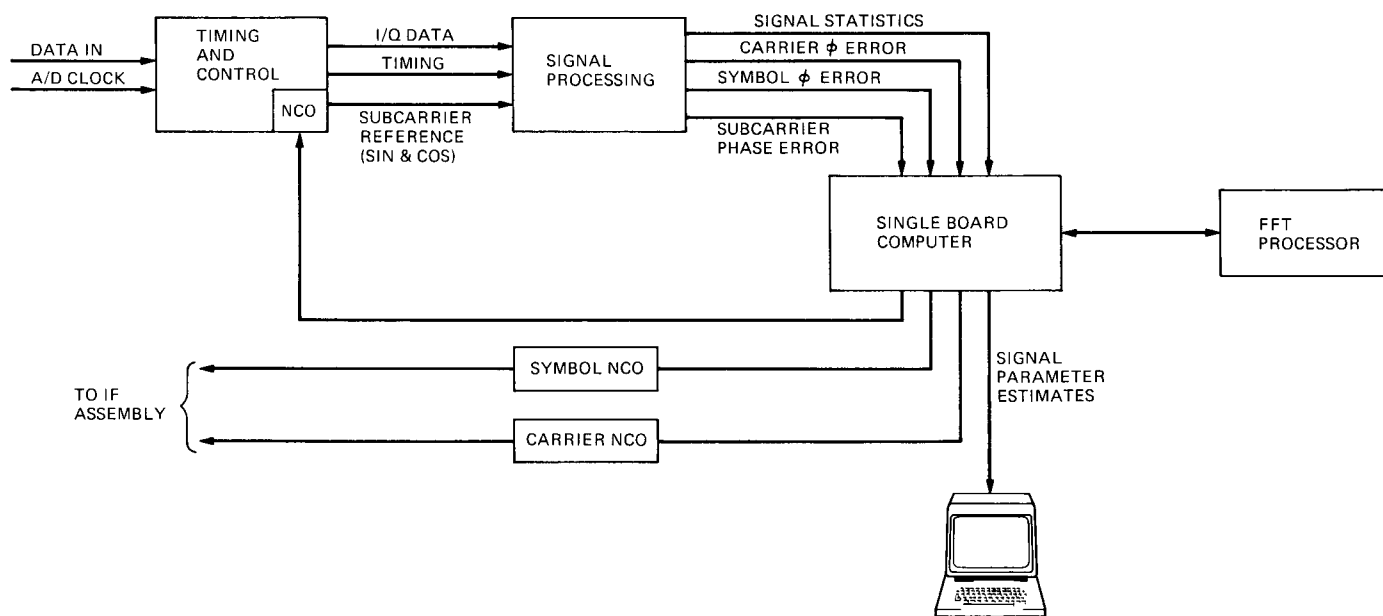**Fig. 2. ARX system block diagram**

Fig. 3. ARX IF assembly

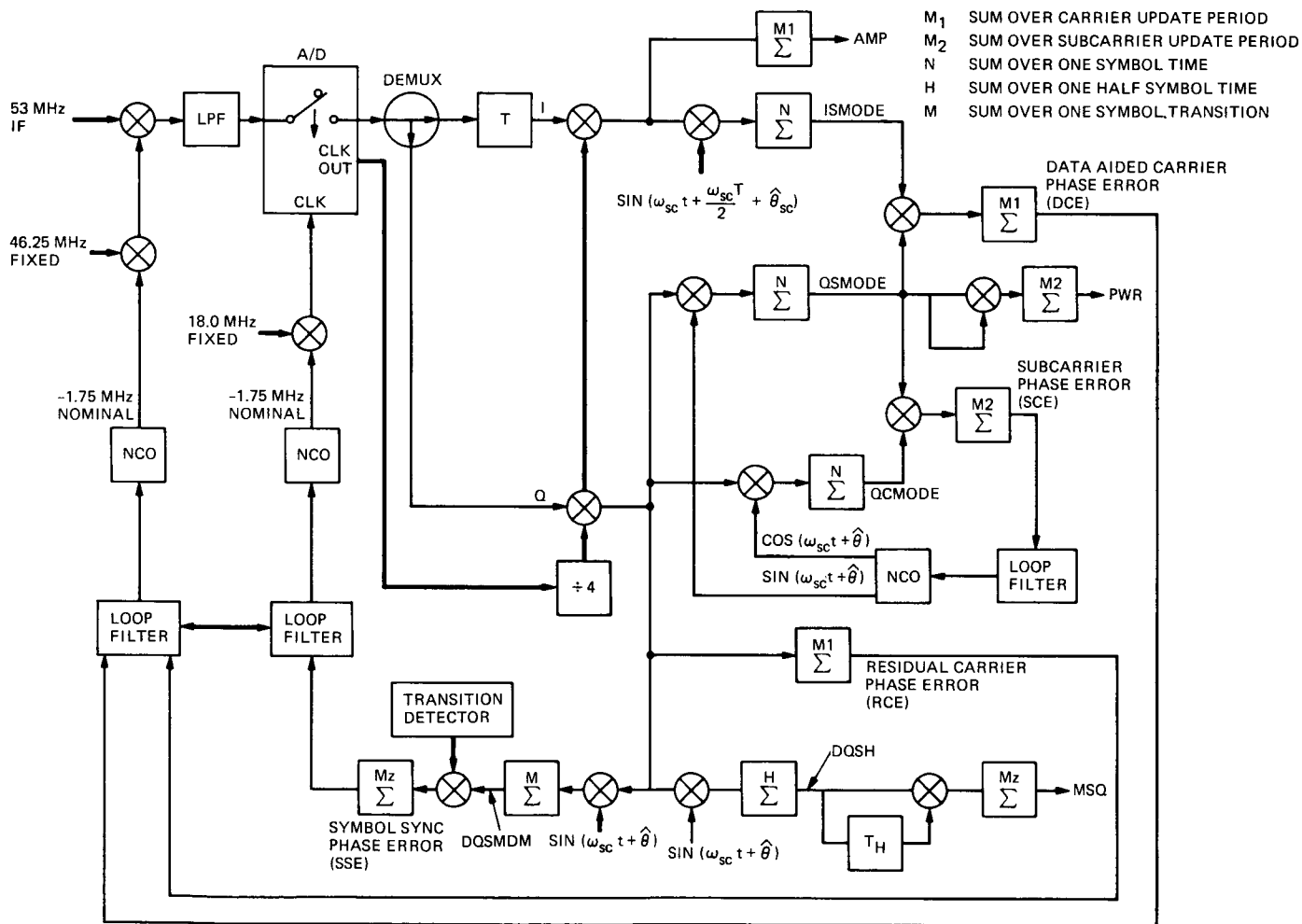**Fig. 4. ARX signal processing assembly**
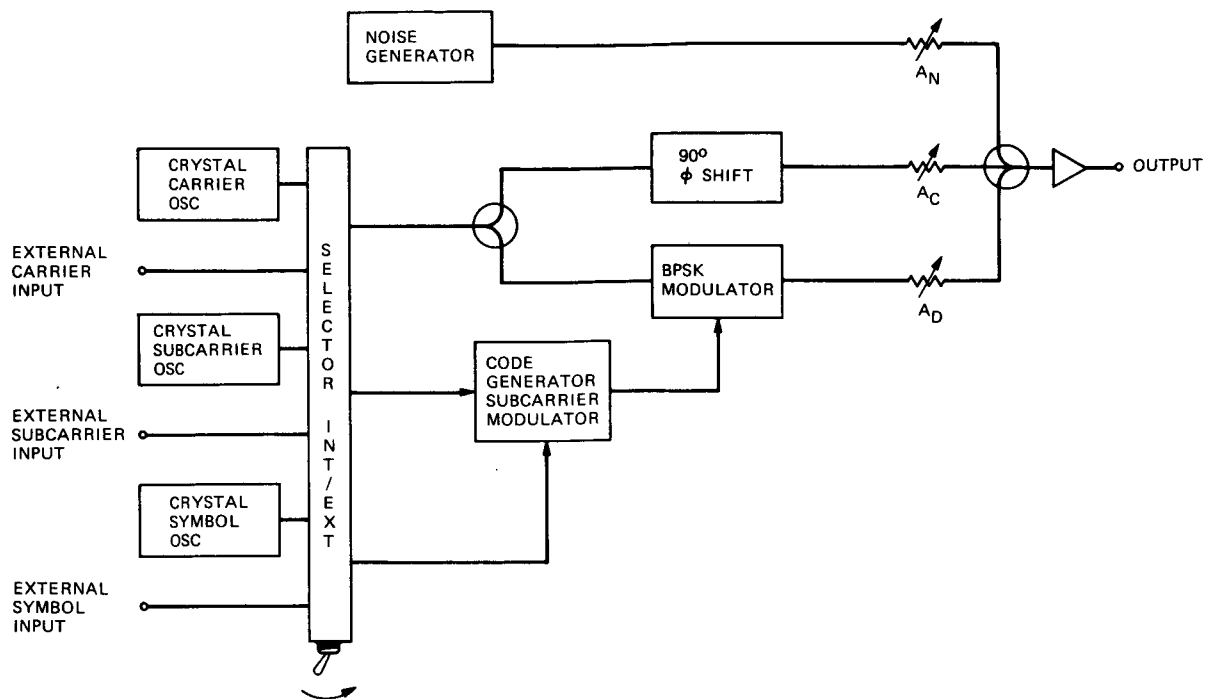
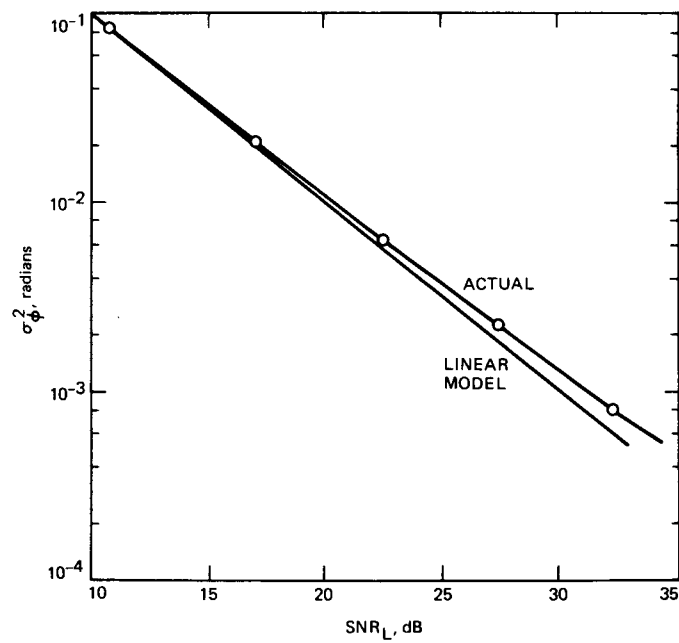**Fig. 5. ARX signal processing diagram**

Fig. 6. ARX test signal assembly

Fig. 7. Linear and actual phase error variances as a function of SNR_L

Results of Using the Global Positioning System to Maintain the Time and Frequency Sychronization in the Deep Space Network

P. A. Clements and A. Kirk

Communications Systems Research Section

R. Unglaub

DSN Control Center Operations Section

There are two hydrogen maser clocks located at each signal processing center (SPC) in the DSN. Close coordination of the time and frequency of the SPC clocks is needed to navigate spacecraft to the outer planets. A recent example was the Voyager spacecraft's encounter with the planet Uranus in January 1986. The clocks were adjusted with the goal of minimizing the time and frequency offsets between the SPCs at encounter. This article describes how the time and frequency at each SPC is estimated using data acquired from Global Positioning System Timing Receivers operating on the NBS-BIH (National Bureau of Standards-Bureau International de l'Heure) tracking schedule. These data are combined with other available timing receiver data to calculate the time offset estimates. The adjustment of the clocks is described. It was determined that the long range hydrogen maser drift is quite predictable and adjustable within limits. This enables one to minimize time and frequency differences between the three SPCs for many months by matching the drift rates of the three standards. The article will describe the data acquisition and processing techniques using a Kalman filter to make estimates of time and frequency offsets between the clocks at the SPCs and UTC (NBS) (Coordinated Universal Time realized at NBS).

I. Introduction

Each SPC (signal processing center) at the Deep Space Communications Complex (three, one at each complex) contains a frequency and timing system which provides the required frequencies and timing pulses for all of the subsystems in that SPC. There are two hydrogen masers located at each SPC; the first acts as the master clock and provides the primary frequency source, and the second acts as a backup. The backup hydrogen maser is kept syntonized (that is, syn-chronized in frequency) to the primary, particularly during critical missions, so that a switch from primary to secondary would have a minimum effect on DSN users.

A requirement exists that timing pulses and frequencies distributed throughout the SPC be coherent. This requirement precludes the use of microsteppers to keep the SPCs clocks synchronized to some uniform time scale. Therefore, the master clock exhibits the characteristic hydrogen maser drift in frequency.

The process of tracking spacecraft involves all three SPCs working in concert to continuously track spacecraft as the earth turns. At Voyager's Uranus encounter the round trip signal transmission time was very long (about five hours). A signal, sent from one SPC to the spacecraft, then transponded and sent back to earth, is received by a second SPC. The Neptune encounter, which is to occur in 1989, will require the transponded signal to be received by the second and third SPC. This procedure requires accurate synchronization and syntonization between SPCs to measure round trip signal transmission time and signal doppler shifts when communicating with the spacecraft. Other requirements such as Very Long Baseline Interferometry (VLBI) and radio science also require accurate synchronization and syntonization among the SPC clocks.

Presently, the DSN Frequency and Timing system (DFT) requirements are to maintain synchronization between SPCs to within ±20 microseconds with a knowledge of ±10 microseconds. Syntonization between SPCs is to be maintained to within 1×10^{-12} df/f with knowledge of $\pm 3 \times 10^{-13}$ df/f. It is possible that navigation at the Voyager Neptune encounter will require knowledge of frequency to less than 1×10^{-13} df/f.

It needs to be emphasized that the DSN is a user of time scales and not a producer. The DSN needs to adjust its clocks from time to time to keep them syntonized and synchronized with each other. It is convenient to use the UTC (NBS) time scale as a reference. First, it is a uniform and continuous time scale. Second, the proximity of the NBS Time and Frequency division to JPL (approx. 1000 km) has historically made NBS the most accessible time scale to the SPC-10 due to the short airplane flight to carry a clock. The use of the Global Positioning System (GPS) time transfer method has made the UTC (NBS) accessible to all SPCs, so we have created an ensemble of clocks using UTC (NBS) as the reference. JPL has a contract with NBS which provides JPL with access to UTC (NBS) and also to the cesium clock associated with WWVH (the NBS time broadcast radio station) in Hawaii, using the data from their GPS timing receiver.

II. The GPS Time and Frequency Coordination System

JPL has installed GPS timing receivers at the three SPCs [1]. These receivers get a timing pulse from the master clock at each SPC which is the "on line" hydrogen maser. The data from these receivers and other data are combined using a Kalman filter to produce estimates of time and frequency offsets of the SPCs with respect to UTC (NBS). JPL uses the tracking schedule published by NBS-BIH. This schedule allows mutual

views with receivers whose tracking data are posted on the GE MK III RC28 Catalog, which is administrated in the United States by the United States Naval Observatory[1]. Figure 1 is a schematic diagram showing the clocks used and the possible mutual views which are available.

The data are gathered by telephone once per week from the receivers in the DSN from the database at NBS and from the GE MK III database using an IBM XT personal computer. This is certainly a change from just a few years ago when we depended on traveling clocks and LORAN. Now we are able to observe the clocks, control them, and provide a guaranteed high accuracy synchronization and syntonization for the users of the DSN.

III. Operation of the Clocks

During the initial installation of a hydrogen maser frequency standard at an SPC, a calibration sequence is performed that includes the following steps:

(1) Verify environmental stability with unit in final position.

(2) Set final operating parameters.

(3) Degauss magnetic shields.

(4) Set internal bias field to required value.

(5) Spin-exchange tune the hydrogen maser cavity.

(6) Calibrate hydrogen maser rate to NBS (synthesizer calibration).

(7) Calibrate rate of backup standards.

(8) Set master and backup clocks.

Figure 2(a) is a quadratic least square fit to the time offsets of the SPCs clocks with respect to UTC (NBS), and Fig. 2(b) is a least square linear fit of the frequency of the clocks with respect to UTC (NBS). The maser frequency drift of approximately 4.5×10^{-15} df/f per day is well behaved and could be matched even closer between the three hydrogen maser clocks. Knowledge of this drift allows us to maximize the time interval between rate adjustments. After the masers are calibrated the cavity is deliberately mistuned so that the average frequency offset with respect to NBS is near zero between rate changes. The average time difference between the three SPCs clocks and NBS is minimized by choosing the appropriate initial time offset. By spin-exchange tuning the hydrogen

---

[1] Available from the Catalog Administrator, USNO Time Service Division, Washinton, D.C. 20390, USA.

maser after one to two years and recalibrating the synthesizer, we will be able to determine the long term drift that is due to mechanisms other than the cavity.

The backup standards are monitored on site with respect to the prime standard so that traceability to NBS is maintained. The rate of these units is manually corrected when necessary so that upon switching from prime to backup standard, the frequency shift is minimal. Figure 2(b) shows that this was not accomplished very well. From about day-of-year (DOY) 100 on, backup standards were shifted in and out for various reasons at SPC-60 and SPC-40. The GPS system gives near real time visibility of clock performance at the three SPCs and enables operational control personnel to evaluate and improve overall system performance.

IV. Example of the Voyager Encounter

As the Voyager spacecraft approaches the planet, calculations are made to correct the estimates of the spacecraft's location. The accurate measurements required for these calculations cannot be made until about 10 to 20 days before encounter. With these measurements, adjustments can be made to produce the desired trajectory by the planet. By having the three SPCs' clocks synchronized and syntonized through the encounter period, accurate measurements of the spacecraft's location can be made.

To satisfy encounter requirements it was decided to adjust the rate and offsets at each SPC so that at encounter the frequency and time difference between each station and NBS would be near zero. This was done about two months prior to encounter.

Daily GPS common view time observations were made to monitor the clock performance at each station. Figure 3 shows the time offsets with respect to NBS. The worst case station-to-station and station-to-NBS offset was less than 500 nanoseconds during the encounter period. Note the several prominent time steps at SPC-60 on days 355, 20, 77, and 87. The master clock at each SPC is driven by a 5 MHz "Flywheel" oscillator which is phase locked to the primary standard 5 MHz output. The phases of the backup standards are not maintained at zero with respect to the prime so that upon switching to the backup standard, a time change of up to ± 100 nanoseconds may result. This happened on the above mentioned days at SPC-40 when, for various tests and experiments, frequency standards were shifted. On about day 100, SPC-60 was directed to shift to a backup standard without first matching the frequency. A frequency change of about 6×10^{-13} df/f led to the rapid divergence of time from day 100 on.

V. Time and Frequency Offsets Using the Kalman Filter

The difference of the data from the receiver pairs is taken to produce mutual view values for clock pair offsets, one value each day for each spacecraft that is used for a mutual view for a given receiver pair. Using space vehicle i,

$$(c_b - c_a + n_{svi})_i = (gps - c_a + n)_i - (gps - c_b + n)_i$$

where n is the noise, n_{svi} is the total common view noise, c_a, c_b are the ground clocks, and gps is the space vehicle clock.

A mean C_{ba}, of the set of mutual view differences is then calculated along with the mean time T.

$$C_{ba} = \frac{1}{m} \sum_i (c_b - c_a + n_{svi})_i$$

$$T = \frac{1}{m} \sum_i t_i$$

where m is the number of daily observations, and t_i is the time of the observation using space vehicle i.

These mean values are used as inputs to the Kalman filter, which has the effect of giving each space vehicle's common view measurement equal weight. This tends to ignore the bias problem which was described by M. A. Weiss [2]. Also, if a measurement is not made for some spacecraft on a particular day, then the biases of the individual spacecraft measurement tend to offset the estimate for that day, an undesirable side effect.

The Kalman filter is a classical design, written in BASIC, and run on an IBM PC-AT computer. The output of the filter is the time, frequency and frequency drift of each clock with respect to UTC (NBS). An estimate of the time, frequency, and frequency drift for any point between endpoints of the data set can be made by smoothing to that point. The procedure is to smooth to 00 hours UTC each day and use that value of the state vector as the estimate of the time and frequency offset of the clock with respect to UTC (NBS). The data are handled in 30 day batches, with each new batch started off with the state vector and the covariance matrix from the previous batch.

Figure 3 shows the detail of the time offset of each of the clocks through the encounter to about DOY 130. The data were generated by the Kalman filter and each day is a point smoothed to zero hours UTC. Each of the clocks is referenced to UTC (NBS). However, because the estimate is for the

same time, the relation between the clocks at any two SPCs can be obtained by subtracting the value of one SPC from that of the second.

Figures 4, 5, and 6 show the estimated value of frequency of the SPCs clocks before, during, and after encounter. On top of these smoothed values are estimates of frequency obtained from the mutual view data by making a linear least squares estimate of the data over about ten day groups of data. These estimates were done manually with judicious choice of data.

Notice the boxed-in detail on Fig. 4, the frequency offset between SPC-10 and UTC (NBS). This indicates that there was almost 1×10^{-13} df/f change in frequency over a period of 10 to 15 days. Unexplained frequency changes of this magnitude have been noticed in hydrogen masers during tests at JPL. However, the mysterious thing is that the other clocks, SPC-40 and SPC-60, showed similar frequency changes at the same time. The Kalman smoother output agrees with the hand calculations of frequency using the mutual view data which indicates the filter is not causing the appearance of similar frequency changes in the several clocks.

One would conclude that the NBS time scale wiggled. Indeed, the wiggle seems to have been at NBS, but not the time scale. At that time JPL was not accessing the data from the time scale, but from clock nine at NBS. A check with NBS confirmed that clock nine experienced a similar frequency excursion at that time. Two conclusions can be drawn from this: the Kalman smoother produces good estimates of the clock performance and the need to make sure the data is from the UTC (NBS) time scale. This procedure was changed late in 1986; JPL presently accesses the UTC (NBS) time scale.

Figure 7 shows the values of Allan variance of frequency estimates of the three SPCs' clocks produced by the Kalman smoother. Nominal expected drift of the hydrogen masers which are deployed is a slope of 4.5 $\times$ 10^{-15} df/f per day. The SPC-10 line follows the performance of the field hydrogen masers fairly well. At four days or less, the SPC-60 and SPC-60 Allan variance is considerably worse than hydrogen maser performance. The SPC-60 Allan variance settled down to hydrogen maser performance at about eight days. The SPC-40 estimates never seem to settle down.

VI. Conclusions

Daily estimates of frequency with errors of less than 1 $\times$ 10^{-13} df/f are available on a routine basis. It appears that this can be reduced to several parts in 10^{-14} df/f in the next few months. Now it has been shown that DSN can be operated continuously with clocks which are syntonized to within 3 $\times$ 10^{-13} df/f and synchronized to within a microsecond. By matching the drift rates of the clocks it might be possible to routinely match the synchronization and syntonization even more closely.

This year's experience has shown that the development of better methods is needed to assure the secondary hydrogen maser is kept closely syntonized with the primary maser.

References

[1] P. A. Clements, S. E. Borutzki, and A. Kirk, "Maintenance of Time and Frequency in the DSN Using the Global Positioning System" *TDA Progress Report 42-81*, vol Jan.-Mar., 1985, pp. 94-108, Jet Propulsion Laboratory, Pasadena, CA, May 15, 1985.

[2] M.A. Weiss, *Proc. 17th Ann. Precise Time And Time Interval Applications and Planning Meeting*, pp. 261-273, Dec. 3-5, 1985.

Fig. 2. Time and frequency offset with respect to UTC (NBS)
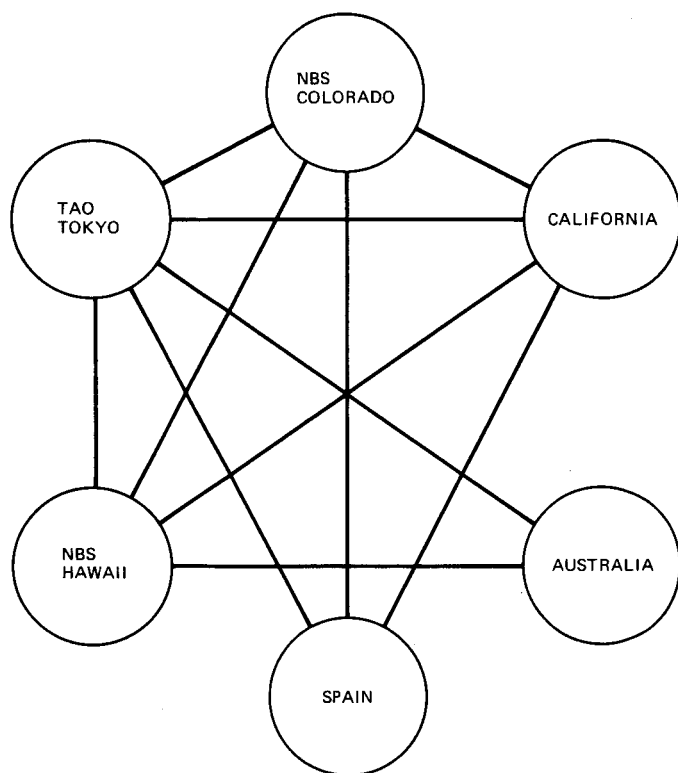

Fig. 1. Possible GPS mutual views available to measure the DSN clocks
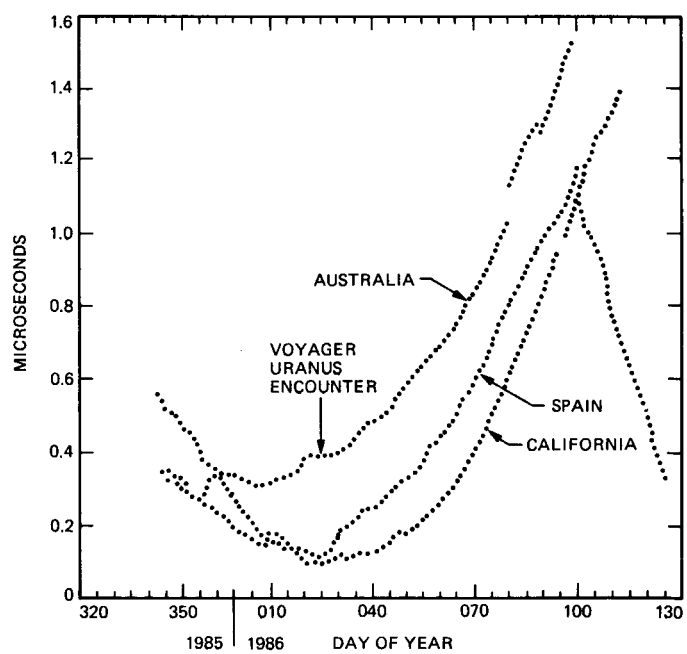

Fig. 3. Time offset with respect to UTC (NBS) (Output of Kalman Smoother)
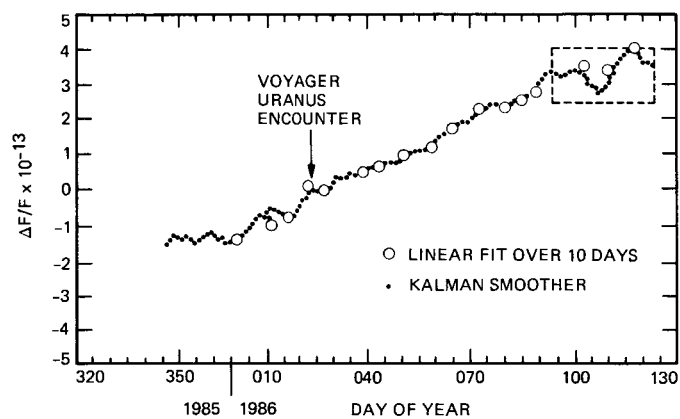
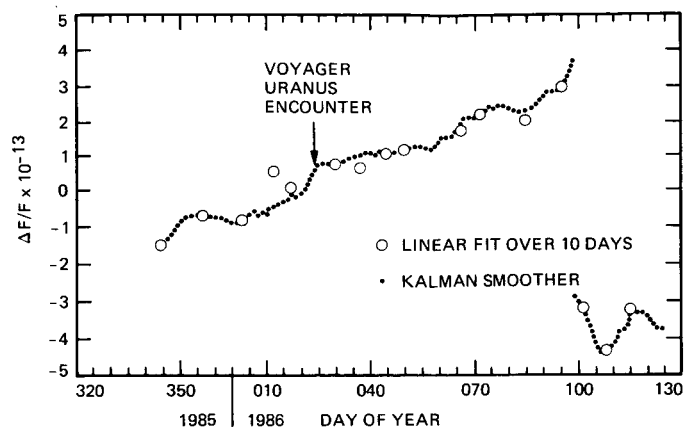Fig. 4. Frequency offset, California–UTC (NBS)
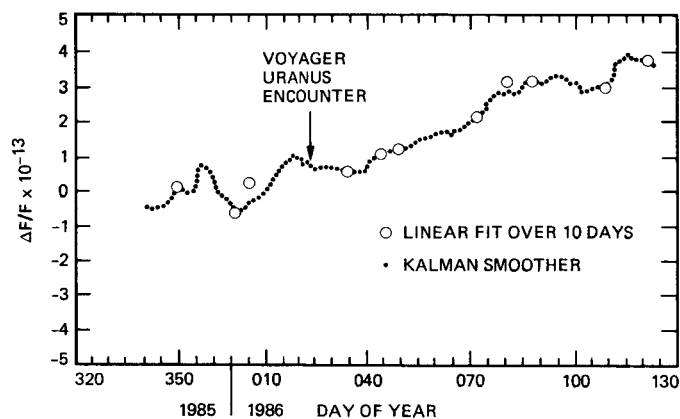

Fig. 6. Frequency offset, Spain–UTC (NBS)

Fig. 5. Frequency offset, Australia–UTC (NBS)
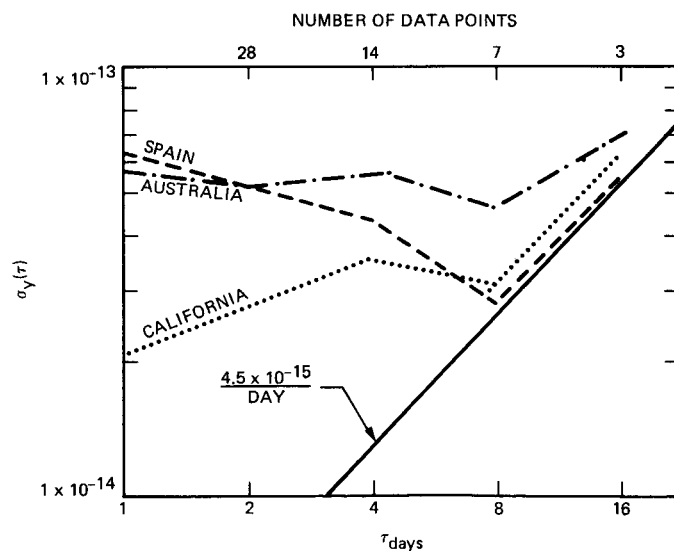
Fig. 7. Allan variance with respect to UTC (NBS)

Microwave Component Time Delays for the 70-Meter Antennas

R. Hartop

Radio Frequency and Microwave Subsystems Section

The X-band feed assemblies in the 64-meter antennas have been redesigned to accommodate the upgrading to 70 meters and the associated surface reshaping. To maintain time delay data logs, new calculations have been made of the microwave component delays for the XRO Mod IV X-band (8.4 to 8.45 GHz) feed assembly that has been installed at DSS-63, and will soon be implemented at DSS-43 and DSS-14.

I. Introduction

Since the microwave time delays were last calculated for the DSN 64-meter antennas [1], the feed configurations at S- and X-band have remained the same, despite some other changes to the antennas (such as the addition of L-band). But the extension of the antennas from 64 meters to 70 meters and the reshaping of the surfaces to further increase the gain has required that the XRO Mod III X-band feed be replaced.

The Mod III feed [2] was designed to provide more efficient illumination of the 64-meter antennas in time for the Voyager 1 encounter with Jupiter. With the current reshaping of the antenna main reflector and subreflector, the dual hybrid mode feed pattern produced by the Mod III feed is no longer advantageous. Thus, the Mod IV feed assembly returns to the DSN standard 22.4 dB gain gaussian beam design. The feed assembly incorporates a Bethe hole coupler for precision phase calibration and a new feedhorn extension that obviates the need to relocate the traveling wave masers within the feedcone. The coupler and feedhorn extension will be reported on later.

II. MOD IV XRO Feed Assembly

The new feed assembly is shown in Fig. 1. A schematic of its layout is shown in Fig. 2. Like the Mod III feed, the new feed incorporates an orthogonal mode transducer to provide simultaneous right- and left-hand circular polarization. Thus, there are two paths to consider for time delays. The quarter-wave plate polarizer is rotatable by 90 degrees to reverse the polarization senses at each output port in the event that the primary traveling wave maser (normally RCP) should fail.

The microwave component time delays, τ_g, (see Table 1) were computed at 8420 MHz using the methods described in [1], with the exception of the new feedhorn. In this case, a new computer program developed at JPL was used. The program calculates the modes propagating (and reflecting) from each discontinuity to find the total delay from the feedhorn throat to the radiating aperture of the extension. This value was then adjusted for the distance to the phase center, which lies in front of the aperture for this feed assembly. As before, the centerline of the TWM coupler (at the Type N coaxial connector) is chosen as the interface to the calibration signal equipment.

Acknowledgment

References

[1] R. Hartop, "Microwave Time Delays in the DSN 34- and 64-Meter Antennas," *DSN Progress Report 42-51*, vol. March-April, pp. 183-185, Jet Propulsion Laboratory, Pasadena, Calif., June 15, 1979.

[2] R. Hartop, "New X-Band Antenna Feeds for the DSN 64-Meter Stations," *DSN Progress Report 42-52*, vol. May-June, pp. 71-74, Jet Propulsion Laboratory, Pasadena, Calif., August 15, 1979.

Table. 1. Microwave component time delays for XRO Mod IV feed assembly at 8420 MHz

Item	τ_g, ns	
Feedhorn	3.479	
Phase calibration coupler	0.477	
Rotary joints, 2, total	0.424	
Polarizer	0.444	
	Straight Path to TWM No. 2	Side Path to TWM No. 1
Orthogonal mode junction	0.707	0.709
Waveguide twist	——	0.511
Waveguide switch	0.342	0.342
Waveguide	——	0.153
TWM coupler (to center)	0.153	0.153
TOTAL delay	6.026	6.690
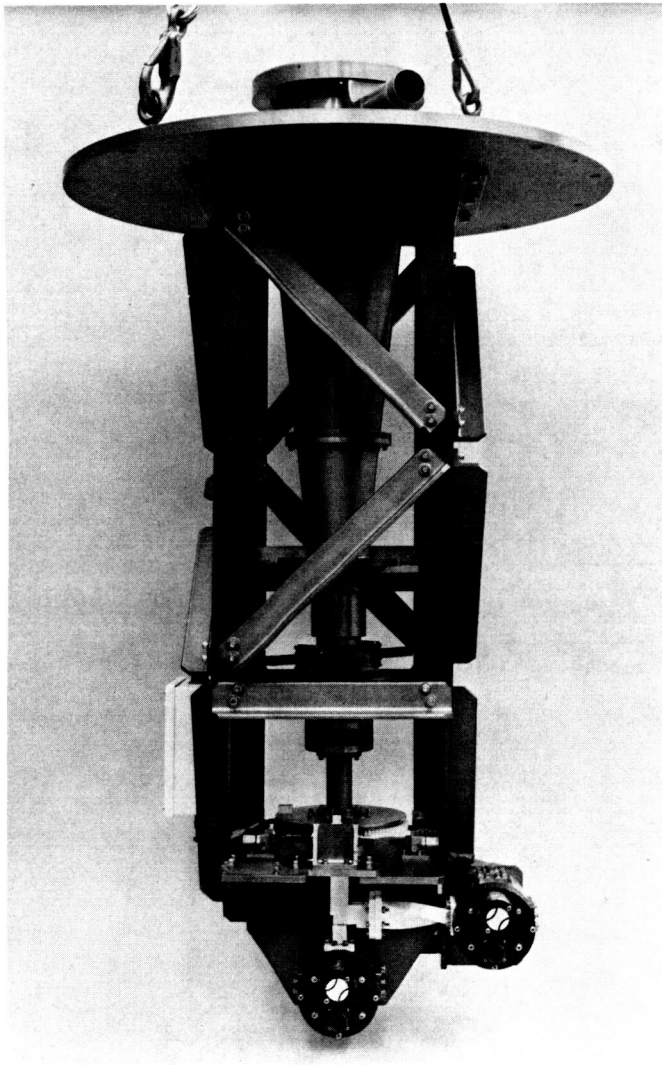
Fig. 1. XRO Mod IV feed assembly
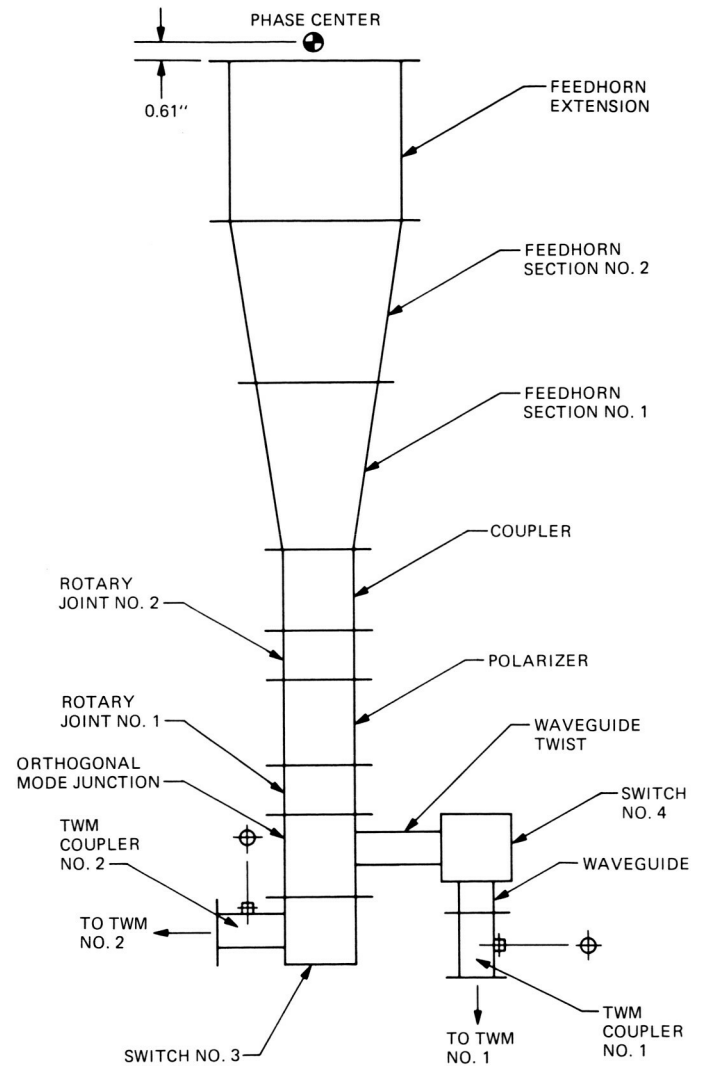
Fig. 2. XRO Mod IV feed layout

TDA Progress Report 42-89

Z-Corrections for DSN 70-Meter Antenna Ranging Calibration

A. G. Cha

Radio Frequency and Microwave Subsystems Section

This article documents the Z-corrections of the DSN 70-m dual-shaped reflector antennas. These corrections to the group delay time measured by the translator are required before the 70-m antennas can be used for ranging.

I. Introduction

This article summarizes the Z-corrections needed for 70-m DSS ranging calibration. According to [1],[1] the Z-corrections consist of four terms: τ_c, τ_d, τ_3, and τ_4, as shown in Fig. 1 and Eq. (1). These numbers come from three separate sources. The τ_4 X-band corrections are discussed in a separate article in this issue [2]. The τ_3 and τ_4 S-band corrections are discussed in [1] and [3]. Details on the derivations of τ_c and τ_d are presented in Section III.

$$Z_{\text{Correction}} = Z_{\text{Translator}} - (\tau_3 + \tau_4 + (\tau_c - \tau_d)_{\text{Up}}$$
$$+ (\tau_c - \tau_d)_{\text{Down}}) \qquad (1)$$

II. Derived Group Delay Time

Tables 1 (X-band) and 2 (S-band) summarize the derived group delay time for the 64-m and 70-m antenna configurations.

III. One-Way Ranging Equation for τ_c and τ_d Corrections

With reference to Fig. 2, a theoretical one-way ranging equation can be written that does not involve a detailed ranging system configuration and hardware. The terminology used in this article follows that of [1] and [4]; range is distance and delay is the group delay time.

A. Phase Delay

Figure 2 shows a Cassegrainian antenna in a microwave system. Point A is the reference location for ranging. Point B is the target location. The distance R is the topocentric range of the target [1]. The phase of a continuous carrier wave received at Point B is exp $[j(\omega t + \Phi)]$. Following [5] and [6],

$$\Phi = \Phi_{wg} + \Phi_{\text{ant}}(\omega) + kL - kR \qquad (2)$$

where $\omega = 2\pi f$, and f is the frequency. The meanings of each term on the right side of Eq. (2) are as follows. The first term is the phase delay from the RF transmitter (uplink) or receiver (downlink) to the feedhorn phase center. The second term is the phase delay in the Cassegrainian antenna from the feedhorn phase center to the aperture plane. The third term is the

phase correction term needed when the aperture plane does not contain the reference location. These are the three correctional terms to the fourth term, which corresponds to the topocentric range R, the distance from the reference point of the ground antenna to the referenced point of the spacecraft antenna.

B. Group Delay Time

The Group delay of the RF signal from the RF transmitter to the target location B is (from [5])

$$t = -\frac{d\Phi}{d\omega}$$

$$= -\frac{d\Phi_{wg}}{d\omega} - \frac{d\Phi_{ant}}{d\omega} + \frac{R-L}{V_c} \qquad (3)$$

where V_c is the free space light velocity and is 2.9979×10^{10} cm/s. The first term in Eq. (3) is the group delay time from the RF transmitter (or receiver) to the feedhorn phase center. The second term is the group delay time in the Cassegrainian antenna.

C. Air Path in Cassegrainian Antennas

A ranging path length may be artificially defined as the product of group delay time in Eq. (3) and free space light velocity.

$$\text{Path length} = -V_c \frac{d\Phi_{wg}}{d\omega} - V_c \frac{d\Phi_{ant}}{d\omega} + R - L \qquad (4)$$

The second term in Eq. (4) is commonly referred to as the air path in the Cassegrainian antenna. For convenience "equivalent path length" is similarly defined in this article for any waveguide component in the ranging system as the product of group delay time and free space light velocity. This will be applied to the dichroic delay at the X-band later. Next, the air path for 64-m and 70-m antennas is derived using geometric optics and aperture theory. The theoretical analysis was made in [5] and [6]. Only the results are applied in this article.

IV. 64-Meter Antenna Air Path and Delay

For classical Cassegrainian antennas consisting of a parabolic main reflector and a hyperbolic subreflector, the air path from the feedhorn phase center to the aperture is given by

$$-V_c \frac{d\Phi_{ant}}{d\omega} = \text{Air path} = f + 2a + d \qquad (5)$$

where

f = Focal length of the paraboloid

$2a$ = Distance between vertices of the two branches of the hyperbola used in defining the Cassegrainian subreflector

d = Distance from main reflector vertex to aperture plane (Fig. 2)

It is shown in [5] and [6] that Eq. (5) is exact in the context of geometric optics (GO) and aperture theory. Equation (5) holds equally in the tricone feed geometry, where the feed and subreflector are tilted relative to the main reflector axis.

When applied to 64-m and 70-m antennas, Eq. (5) must be supplemented by the additional air path of the horn/ellipsoid/dichroic at S-band and delay through the dichroic plate at X-band. These are worked out in [7]. This information is included in Table 3 for reference.

Figure 3 shows the relevant dimensions of the 64-m antenna for ranging. Traditionally, the 64-m antenna aperture plane is taken as the plane defined by the rim of the parabolic main reflector. In this case the distances d and L are given by

$$d = \frac{\rho^2_{main}}{4f} \qquad (6)$$

$$L = d + 807.72 \text{ cm} \qquad (7)$$

In Eq. (6), ρ_{main} is the radius of the main reflector. Note that d and L are dependent on ρ_{main}. The radius of the 64-m antenna is taken to be 3200.4 cm to be consistent with [7].

V. The 70-Meter Antenna Air Path and Delay

The 70-m antenna geometry relevant to ranging is shown in Fig. 3. The information is extracted from Figs. 3-1, 3-3, and 3-4 of another document.[2] The air path of the shaped 70-m antenna is not given by such simple algebraic expression as Eq. (5). However, from geometric optics synthesis of the antenna, the air path from feedhorn to plane 2 (Fig. 3) is

$$\text{Air path} = 4835.96 \text{ cm } (1903.92 \text{ in.})$$

---

[2] A. G. Cha and W. A. Imbriale, "Computer Programs for the Synthesis and Interpolation of 70-Meter Antenna Reflector Surfaces," JPL D-1843 (internal document), Jet Propulsion Laboratory, Pasadena, Calif., Nov. 1984.

The plane 2 is a reference used in the geometric optics synthesis program of the 70-m antenna and is seen from Fig. 3 to be 1893.2 cm above the intersection point A of elevation and azimuth axes. Note, as shown in Fig. 3, plane 2 is not defined by the rim of the 70-m antenna main reflector.

The 64-m antenna and aperture plane are shown in Fig. 3. In the following, the 64-m aperture plane, plane 1 in Fig. 3, is also used as the 70-m aperture plane. This simplifies comparisons of the air path and delay of the 64-m and 70-m antennas, as the group delay from the aperture plane to the ground reference point for the two antennas would then be the same. This is shown in Table 3. If other ground reference points and/or aperture planes are preferred, the antenna air path and group delay from the aperture plane to the ground reference point would then be different for 64-m and 70-m antennas. The new 70-m numbers can be worked out in a straightforward manner from Eqs. (3) and (4).

At press time, it appears that the main reflector surface of DSS 63 is 1.2 cm (0.5 in.) higher than originally designed. Since this variation is not exactly known at present and will be different for each of the three 70-m antennas, future revisions will be issued for each of the antennas when the exact information is available.

Acknowledgment

References

[1] T. Komarek and T. Otoshi, "Terminology of Ranging Measurements and DSS Calibrations," *DSN Progress Report 42-36*, pp. 35–40, Jet Propulsion Laboratory, Pasadena, Calif., Dec. 1976.

[2] R. Hartop, "Microwave Component Time Delays for the 70-Meter Antennas," *TDA Progress Report 42-89*, Vol. January–March, Jet Propulsion Laboratory, Pasadena, Calif., May 15, 1987.

[3] T. Otoshi, K. B. Wallace, and R. B. Lyon, "Dual Coupler Configuration at DSS 14 for the Voyager Era," *DSN Progress Report 42-42*, pp. 184–192, Jet Propulsion Laboratory, Pasadena, Calif., Sept. 1977.

[4] T. Otoshi and K. R. Weld, "Updated Z-Corrections for 64-m DSS Ground Station Delay Calibrations," *DSN Progress Report 42-47*, Vol. July and August, pp. 77–84, Jet Propulsion Laboratory, Pasadena, Calif., 1978.

[5] A. G. Cha, W. V. T. Rusch, and T. Otoshi, "Microwave Delay Characteristics of Cassegrainian Antennas," *IEEE Trans. on Antennas and Propagation*, Vol. AP–26, No. 6, pp. 860–865, Nov. 1978.

[6] A. G. Cha, "Phase and Frequency Stability of Cassegrainian Antennas," *Radio Science*, pp. 156–166, Jan. and Feb. 1987.

[7] R. Hartop, "Microwave Time Delays in the DSN 34- and 64-Meter Antennas," *DSN Progress Report 42-51*, vol. Mar. and Apr. 1979, pp. 183–185, Jet Propulsion Laboratory, Pasadena, Calif., May 15, 1979.

Table 1. X-band delay, ns

Correction	64-m	70-m	Delta
τ_c	152.28	156.79	4.51
τ_d	58.45	58.45	–
τ_3	No X-band uplink at present. Use S-band number for S– uplink and X-downlink.		
τ_4	Straight path 5.986 Side path 6.417	Straight path 6.026 Side path 6.690	0.040 0.273

Table 2. S-band delay, ns

Correction	64-m	70-m	Delta
τ_c	161.16	165.68	4.52
τ_d	58.45	58.45	–
τ_3	22.18	22.18	–
τ_4	19.66	19.66	–

Table 3. Air path and group delay for 64-m and 70-m antennas

Parameter	64-m		70-m	
	S-band	X-band	S-band	X-band
f, cm (in.)	2711 (1067.294)	2711 (1067.294)	–	–
$2a$, cm (in.)	904 (356.057)	904 (356.057)	–	–
d, cm (in.)	945 (371.875)	945 (371.875)	–	–
Air path, horn to aperture plane,* in absence of reflex/dichroic feed, cm (in.)	4560 (1795.226)	4560 (1795.226)	4695 (1848.42)	4695 (1848.42)
Air path due to reflex/dichroic feed, cm (in.)	272 (106.963)	5.49[†] (2.16)	272 (106.963)	5.49[†] (2.16)
Air path total, cm (in.)	4832 (1902.189)	4565 (1797.39)	4967 (1955.51)	4700 (1850.58)
One-way group delay, horn to aperture plane, ns	161.16	152.28	165.68	156.79
One-way group delay, aperture plane to reference point, ns	58.45	58.45	58.45	58.45
Net downlink airpath delay, ns	102.71[‡]	93.83[‡]	107.23	98.34

*Aperture plane is plane 1, Fig. 3, for both antennas (64-m antenna aperture plane).
[†]Converted from group delay of 0.183 ns [6].
[‡]Agree closely with values for Z_6 in [3].

SUBREFLECTOR

APERTURE
PLANE

τ_c τ_c

τ_d

REFERENCE
LOCATION

ANTENNA

τ_4 τ_3

H

TEST
TRANSLATOR   UWV   TEST
                                  TRANSLATOR

H   HORN PHASE CENTER
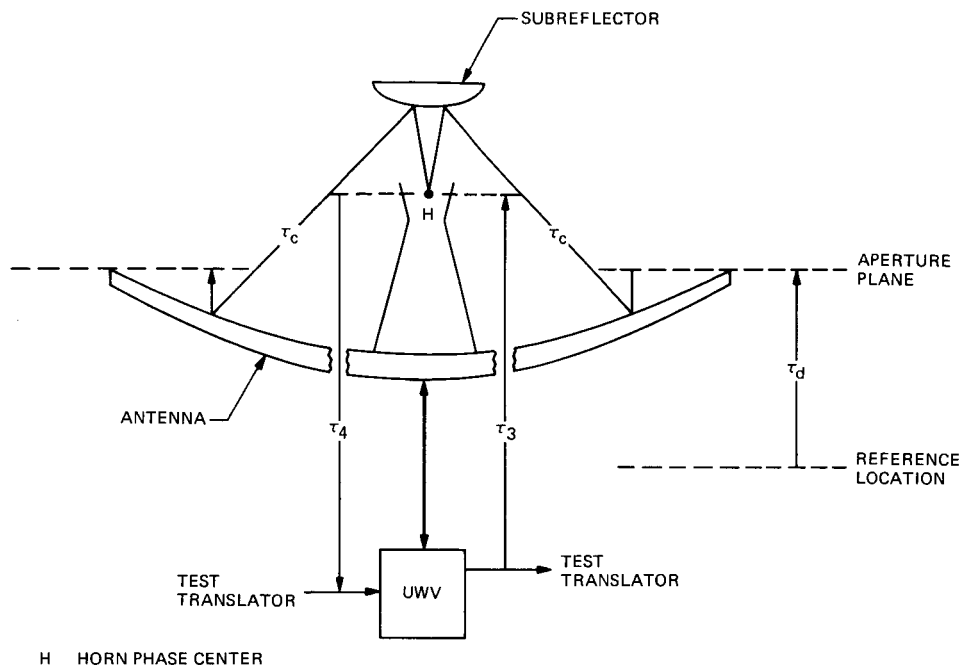
Fig. 1. Definitions of Z corrections

MAIN
REFLECTOR

APERTURE
PLANE

X

SUBREFLECTOR   A   INTERSECTION OF
                           ELEVATION AND
                           AZIMUTH AXES
A V H   B   Z V   MAIN REFLECTOR VERTEX
                       H   FEEDHORN PHASE CENTER
                       B   TARGET LOCATION

d

L

R
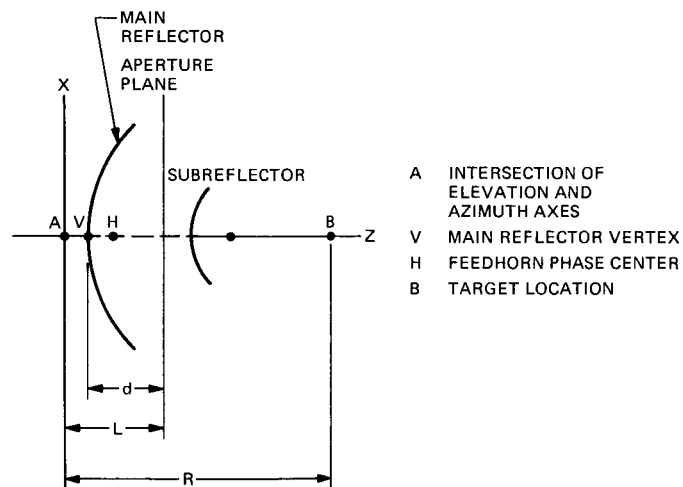
Fig. 2. Cassegrainian antenna in a microwave ranging system
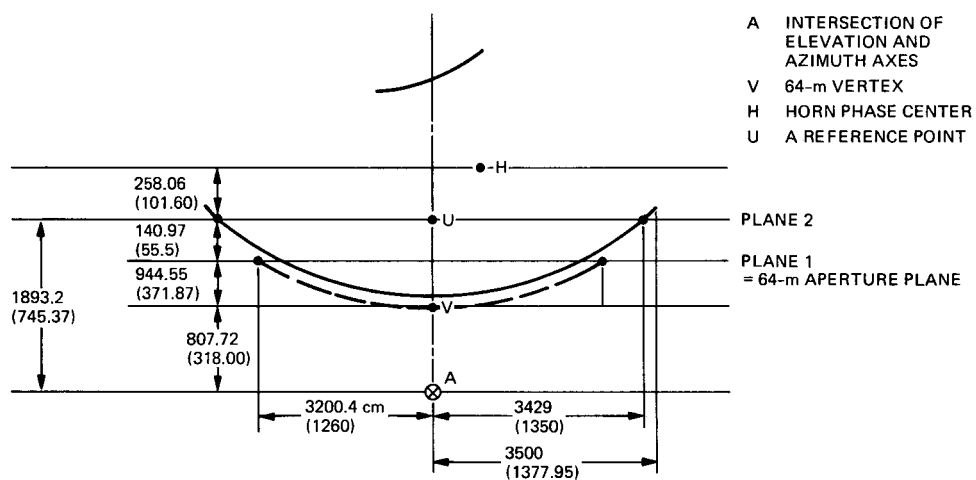
Fig. 3. Geometry of 64-m and 70-m antennas

A   INTERSECTION OF ELEVATION AND AZIMUTH AXES
V   64-m VERTEX
H   HORN PHASE CENTER
U   A REFERENCE POINT

258.06 (101.60)
140.97 (55.5)
944.55 (371.87)
1893.2 (745.37)
807.72 (318.00)
3200.4 cm (1260)
3429 (1350)
3500 (1377.95)

PLANE 2
PLANE 1 = 64-m APERTURE PLANE

Block III X-Band Receiver-Exciter

C. E. Johns

Radio Frequency and Microwave Subsystems Section

The development of an X-band exciter, for use in the X-Band Uplink Subsystem, has been completed. The exciter generates the drive signal for the X-band transmitter and also generates coherent test signals for the S- and X-band Block III translator and a doppler reference signal for the doppler extractor system. In addition to the above, the exciter generates other reference signals that are described in this article. Also presented is an overview of the exciter design and some test data taken on the prototype. A brief discussion of the Block III doppler extractor is presented.

I. Introduction

A new X-band exciter has been developed for the X-Band Uplink Subsystem for use in the Deep Space Network (DSN) that will provide the required $\Delta f/f$ stability of 5.2×10^{-15} for 1000 second integration periods. A similar (prototype) exciter was developed earlier [1] and evaluated at DSS 13. The evaluation has been completed and test results verified that its mechanization was appropriate for the new DSN exciter.

The exciter design is discussed in Sections II through VII, covering the overall block diagram generation of the X- and S-band receiver test signals, generation of the receiver 1st L.O., and generation of the reference signals to the ranging and doppler subsystems. In addition, the exciter phase control loop design is described, as well as the command phase modulation (and verification) and ranging modulation capabilities.

II. Basic Exciter Signal Generation

A simplified block diagram of the exciter is shown in Fig. 1. The configuration is similar to that described in [1] with the exceptions of the mechanization of the doppler reference signal, the references to the ranging and doppler subsystems, and the newly included receiver 1st L.O. signal. To generate the X-band exciter signal, F_x, a 43.125 MHz synthesizer input signal is multiplied by a factor of 16 to 690 MHz and mixed with 6500 MHz to provide the 7200 MHz sum frequency. The 6500 MHz is generated by multipling a 100 MHz input reference (from the station hydrogen maser) by a factor of 65. The 7200 MHz is selected at the mixer's output by a bandpass filter and then used as the basic exciter signal. The exciter signal is then amplified and connected through X-band command and ranging phase modulators. An RF relay is used for enabling or disabling the exciter output.

Prior to multiplying the 43.125 MHz synthesizer signal, the signal is passed through a 43 MHz voltage controlled phase shifter module used in the exciter phase control loop (described below).

III. Reference Exciter

A second X-band signal is generated within the exciter in a manner similar to the exciter signal. The 43.125 MHz input is divided into two paths. One path is used for driving the

exciter channel (as described above). The second path is multiplied by another ×16 multiplier and mixed with the 6500 MHz reference signal to yield an unmodulated X-band reference signal. This signal is used as the phase detector reference within the phase control loop.

IV. Exciter Functions

A. Exciter Phase-Control Loop

To reduce phase variations in the transmitted signal (that can be caused by component variations due to temperature changes, klystron characteristics, etc.), a phase correcting loop is incorporated within the exciter. A phase correcting loop is used in the original DSS 13 exciter, but the mechanization of the DSN exciter loop has been redesigned to improve loop gain and linearity. The original design did not use a reference exciter and the loop error was applied directly to an X-band phase shifter in the exciter path. To attain the required loop gain, high dc amplification was required, which resulted in excessive loop nonlinearities (amplifier saturation) with large phase error conditions.

Figure 2 is a simplified diagram of the DSN exciter phase control loop flow (heavy lines). When the phase control loop is used for controlling the output of the transmitter relay, K_x is actuated to allow the transmitter signal to be applied to the signal port of the loop detector and phase compared with the exciter reference signal. When relay K_x is in the exciter position, the loop controls only the phase of the exciter output. The error at the detector's output (due to the nonquadrature relationship of the two signals) is applied to a low pass RC filter and then amplified by a dc amplifier.

The filtered voltage, static phase error (SPE), from the amplifier is then applied to the dc control port of the 43 MHz voltage controlled phase shifter module. The phase of the 43 MHz exciter signal, applied to the input, is shifted proportionally to the SPE voltage and then multiplied by 16 by multiplier M1. The 690 MHz from the ×16 is then mixed with the 6500 MHz reference signal to provide the phase shifted X-band exciter output signal. The correction forces the phase of the transmitter signal toward quadrature, relative to the reference signal, at the phase detector inputs. The gain of the voltage controlled phase shifter followed by the ×16 multiplication increases the loop gain, permitting an appreciable reduction in dc amplifier gain that results in improved loop linearity in the presence of large phase errors.

The design −3 dB bandwidth of the loop is 2 Hz to ensure that low frequency command signals are not reduced by the loop response. The design loop gain is 100 to reduce transmitted phase perturbations by that factor.

A mathematical model of the loop is shown in Fig. 3 and the complex loop transfer function, $H(s)$, is derived below the figure. When the term $16\ k_d\ G_a\ K_\phi$, in the denominator, is set equal to the total loop gain, G_T, the loop transfer function becomes:

$$H(s) = \frac{RCs + 1}{RCs + G_T + 1}$$

Letting $s = jw$ and taking the absolute value of the transfer function:

$$|H(jw)| = \frac{\sqrt{((RCw)^2 + 1)}}{\sqrt{((RCw)^2 + (G_T + 1)^2)}}$$

To solve for the loop RC time constant, the cutoff frequency w_c, is set to $2\pi f_c$, where $f_c = 2$ Hz and $G_T = 100$. Setting $|H(jw)| = 2^{-1/2}$ and solving for RC:

$$RC = \frac{\sqrt{(100^2 + 200 - 1)}}{(2)(\pi)(2)} = 8.037 \text{ sec}$$

The loop filter time constant used within the exciter is 8 seconds.

Substituting 8 for RC, $2\pi f$ for w, and 101 for $G_T + 1$, the transfer function becomes:

$$|H(j2\pi f)| = \frac{\sqrt{((8 \times 2\pi f)^2 + 1)}}{\sqrt{((8 \times 2\pi f)^2 + (101)^2)}}$$

or

$$|H(j2\pi f)| = \frac{\sqrt{(2526.62 f^2 + 1)}}{\sqrt{(2526.62 f^2 + 10{,}201)}}$$

which is the ideal design loop response. This is plotted in Fig. 4.

B. Command Modulator and Verification

The X-band exciter signal is divided into two paths prior to application to the command phase modulator. One path allows the exciter to be phase modulated by command signals and the second serves as a phase detector reference, where it is phase compared to the modulated signal. The modulated signal is again divided into two paths—one path for the exciter output and the second for command verification.

The verification path is coupled through an X-band voltage controlled phase shifter, used within, in a phase correcting loop, and then coupled into the signal port of the verification phase detector. The resultant detector output, when the reference and modulated signals are in quadrature, is a demodulated replica of the command input signal with the exception that, since the output of the detector is sinusoidal with phase, the amplitude is compressed relative to the original modulation signal. The verification signal amplitude, A_m, is optimized at a modulation index of 45 degrees, and the amplitude can be closely computed by $A_m = 0.37 \sin (\text{mod index})$, where the modulation index is in degrees. The detector output is coupled into a module containing a video amplifier that provides two verification outputs that are coupled through coaxial cables to the command subsystem.

The module also contains an active low pass filter circuit whose output is coupled into the voltage control port of the phase shifter. The filter circuit controls the phase of the modulated signal, keeping it near quadrature relative to the reference signal. The design gain of the loop is 100 to reduce phase drifts to a negligible amount. The design frequency response is 2 Hz to prevent the tracking out of command signals in the 50 Hz range.

The verification phase control loop is mechanized somewhat like the exciter phase control loop, with the exception that it does not have the advantage of the phase gain of the 43 MHz voltage controlled phase shifter and its following $\times 16$ frequency multiplier. It was therefore necessary to increase the gain of the dc amplifier to obtain a loop gain of 100. Since the loop gain and cutoff frequency of the verification loop is the same as the exciter loop, the loop filter RC time constant is 8 seconds.

The high frequency response is designed to have a -1 dB cutoff of 150 kHz and is set by a low pass filter within the modulation control module.

C. Range Phase Modulator

A second X-band modulator follows the command modulator for application of ranging signals to the uplink signal. The modulator, including the range modulation control, is similar to the command modulator with exception of the modulation bandwidth. The ranging bandwidth is in excess of 5 MHz at the -3 dB point. By means of the exciter controller, up to two modulation signals can be applied to the X-band carrier.

D. Exciter On/Off Control

The DSS 13 X-band exciter was not equipped with an exciter on/off control to disable the drive to the transmitter input. The DSN exciters are equipped with a control to disable the output signal by means of the exciter controller. In addition, the control relay controls the transmitter warning light, located in the antenna.

E. Coherent X- and S-Band Test Signals

Coherent X- and S-band test signals are generated within the exciter. The method used for generating these signals is described in [1], but by reference to Fig. 1, it can be seen that the $F_x/80$ signal is multiplied by a factor of 10,480/749 (by means of a $\times$ 2096/749 and a $\times$ 5 multiplier) and mixed with a sample of the exciter signal to provide a sum frequency of 880/749 F_x, which is the coherent X-X receiver frequency. Similarly, the coherent S-band signal is generated by multiplying the $F_x/80$ signal by a factor of 40,720/749 (by means of a $\times$ 8144/749 and a $\times$ 5 multiplier), to generate a coherent 509/749 F_x signal that is mixed with a sample of the exciter output to provide a 240/749 F_x difference signal, the coherent X-S receiver frequency.

F. Receiver First L.O. Generation

To generate the coherent 640/749 1st L.O., the $F_x/80$ signal is multiplied by a factor of 8720/749 (by means of a 1744/749 multiplier followed by a $\times$ 5 multiplier), to produce a coherent 109/749 F_x signal. This signal is mixed with a sample of the unmodulated exciter signal to produce the coherent L.O. used to drive the X- to S-band down converter mixer. The L.O. signal down converts the received X-band to the required S-band input to the Block III receiver (880/749 F_x - 640/749 F_x = 240/749 F_x). The mixer output is filtered, amplified, and applied to an output terminal on the exciter.

G. 48 MHz Doppler Reference

The 48 MHz doppler reference signal is generated by multiplying the $F_x/80$ signal by a factor of 400/749 to obtain the required 5 $F_x/749$ ratio. The doppler signal is then coupled to the Block III receiver into the doppler reference distribution module (described below).

H. Tracking Subsystem References

To generate the 66 MHz exciter reference signal, F_{range}, for the ranging subsystem, the $F_x/80$ signal is multiplied by a factor of 11/15. The ratio of the output of the module to the exciter frequency is $F_{range} = 11 F_x/1200$. This mechanization was used to keep the frequency near the frequency supplied to the ranging subsystem from the Block III S-band exciter. The 22 MHz exciter reference to the MDA, F_{MDA}, is generated within the same module by dividing the 66 MHz by a factor of 3. The ratio of this signal to the exciter output is $F_{MDA}/F_x = 11/3600$.

V. Physical Configuration

The exciter is housed in three wall mounted Hoffman enclosures, each 36 in. by 24 in. by 8 in. Two of the enclosures contain the rf hardware and the third contains the power supplies and controller board. One rf enclosure (Test Signal and Reference Generator Assembly) contains the X16 multipliers, the 43 MHz phase shifter, the 13/16 frequency shifter and mixer, and all the frequency shifters used for generating the test and reference signals. The second rf enclosure (Mixer/Modulator Assembly) contains the mixers, the command and range phase modulators (and their associated controllers), the components for the exciter and confirmation phase control loops, the exciter output amplifier, and the exciter relay. The third box contains the power supplies and the single circuit board exciter controller. The controller is briefly described below.

VI. Temperature Stabilization

The components within each of the rf enclosures are ovenized to ensure signal stability over ambient variations of plus and minus 5°C around the mean elevation room temperature of 22°C. The temperature stability of the rf enclosures was measured in the JPL Environmental Lab. The measurements showed that the internal temperature of the Test Signal and Reference Generator Assembly will change 1°C for an ambient change of 7°C and the temperature of the Mixer/Modulator Assembly will change 1°C for a 10°C change.

VII. Controller

The exciter functions are controlled and monitored by means of a manual control panel located in the control room. A single controller circuit board is located within the power supply box in the antenna equipment and a two circuit board system is located within the control room equipment. One of the control room boards is used for communicating with the antenna (sending configuration data and storing monitor data) and the second is reserved for future interfacing with the Block III Monitor and Control Subsystem. A Universal Asynchronous Receiver/Transmitter (UAR/T) integrated circuit (IC) is used for transmitting control data to the antenna unit and a similar IC is used in the antenna unit to send monitor data to the control room. A CLEAR pulse is transmitted from the control room to the antenna at approximately 10 pps. The pulse synchronizes the circuitry at both ends and permits new data transmission at 10 times per second.

Control data actuates relays within the exciter to their required position, such as exciter on or exciter off, and monitor data indicates relay position. Also, the rf output power of most of the modules is monitored in the form of a single bit to indicate the presence or absence of rf. Other monitor data are power supply outputs, internal oven temperatures, and exciter output.

VIII. Doppler Reference Distribution

The 5 F_x/749 doppler reference signal (about 48 MHz), generated by the exciter, is coupled through coaxial cable to the control room and into the input of the doppler reference distribution module. Figure 5 is a simplified block diagram of the module showing the internal mixing processes that generate the 22 MHz reference signals for the doppler subsystem. The 22 MHz is not the same as that supplied from the X11/45 multiplier in the exciter. To generate the 22 MHz, a 26 MHz signal is generated from 1, 10, and 45 MHz reference inputs and mixed with the 48 MHz doppler reference from the exciter. As shown in Fig. 5, there are two mixers that generate the 22 MHz for the doppler subsystem—one from connector J6 that is permanently generated by mixing the 48 MHz with the 26 MHz reference, and one from J7, generated by mixing the 26 MHz with the 48 MHz from the exciter or the 48 MHz from the simulation synthesizer (sim synth), depending on the selected relay position within the module.

A third output, J4, supplies the 48 MHz to the Block III doppler mixer and X48 multiplier and can be selected from the exciter or the sim synth.

IX. Doppler Extraction

Figure 6 is a functional diagram of the complete doppler extraction system. Within the doppler mixer and X48 frequency multiplier module, the 48 MHz doppler reference from the exciter or the sim synth is mixed with twice the receiver VCO frequency, and the resulting difference is multiplied by a factor of 48 to yield 50 MHz doppler. The signal is then divided into two paths—one path is mixed with an externally applied 45 MHz reference to give a 5 MHz doppler difference that is connected to an output connector. The second path is mixed with a selectable 49 or 51 MHz reference to give a plus or minus (1 MHz doppler) difference that is also connected to output connectors on the module.

X. Exciter Test Results

A. Exciter Phase Correcting Loop

Frequency response measurements were made on the DSN exciter to verify the exciter phase correcting loop response. The measured response is shown in Fig. 4, along with the ideal

design response. Using the measured -3 dB point and the measured loop constants, the gain was computed to be 112. This was verified by a second measurement made by shorting the loop and introducing a known phase error (by calibrating the loop phase detector output), and then enabling the loop and again measuring the phase detector output.

B. Command Verification Phase Correcting Loop

The measured response of the command verification phase correcting loop is shown in Fig. 7. During the measurements, the exciter phase correcting loop was operating and therefore the response at 2 Hz is about -6 dB, as expected.

C. Command Confirmation Signal Linearity

The measured command verification signal level vs modulation angle is shown in Fig. 8. The output amplitude can be closely computed by A_m = 0.37 sin (mod angle), where the modulation angle is expressed in degrees. The computed, measured, and ideal curves are also shown for comparison.

D. Control and Monitor

All control and monitor functions were verified using the prototype X-Band Controller Assembly. To date, the exciter controller has not been interfaced with a system controller.

XI. Conclusions

Measurements made on the prototype DSN X-band exciter have been performed and the results show that the rf, control and monitor, and internal phase correcting loops perform to their design criteria. To date, the exciter stability ($\Delta f/f$) measurements have not been performed, but these measurements, as well as single sideband noise spectral density measurements, will be made in the near future.

Reference

[1] R. Hartop, C. Johns, and R. Kolbly, "X-Band Uplink Ground Systems Development" *DSN Progress Report 42-56*, vol. Jan.-Feb. 1980, pp. 48-58, Jet Propulsion Laboratory, Pasadena, CA, April 15, 1980.

VERIFICATION OUTPUTS TO COMMAND

VIDEO AMPLIF | LOWPASS FILTER

C/M C/M

COMMAND AND TEST MODULATION

C/M COMMAND MODULATION CONTROL

CONFIRMATION LOOP PHASE DETECTOR

PH CONT LOOP SPE

C/M ACTIVE LOWPASS FILTER

C/M RANGE MODULATION CONTROL

RANGE MODULATION

MON x16

BANDPASS FILTER 7190 MHz

LOOP PHASE DETECTOR

C/M TRANSFER RELAY, K$_R$

TRANSMITTER SAMPLE INPUT (749 F$_x$/749)

EXCITER ON/OFF

LIMITER

INPUT 40.3125 TO 45.9375 MHz FROM SYNTH

43 MHz VOLTAGE CONT PHASE SHIFTER

MON x16 ÷5

BANDPASS FILTER 7190 MHz

COMMAND PHASE MODULATOR

RANGE PHASE MODULATOR

C/M

EXCITER OUTPUT (749 F$_x$/749)

MON

100 MHz REFERENCE INPUT

x85 6500 MHz

WARNING LIGHT CONTROL

C/M C/M

F$_x$/80-1300/16

MON

F$_x$/80 (6 OUTPUTS)

100 MHz REFERENCE INPUT

x13/16

1744/749 FREQUENCY SHIFTER

MON x5 109 F$_x$/749 648 F$_x$/749

BANDPASS FILTER 6144 MHz

RECEIVER 1st L O OUTPUT (640 F$_x$/749)

2096/749 FREQUENCY SHIFTER

MON x5 131 F$_x$/749 C/M

X-BAND TEST SIGNAL OUTPUT (880 F$_x$/749)

F$_x$/80 (90 MHz) SPARE
66 MHz TO PRA
22 MHz TO DOPPLER

x11/15 x11/45

8144/749 FREQUENCY SHIFTER

MON x5 509 F$_x$/749

S-BAND TEST SIGNAL OUTPUT (240 F$_x$/749)

400/749 FREQUENCY SHIFTER

MON 5 F$_x$/749

DOPPLER REFERENCE OUTPUT (5 F$_x$/749)

C/M CONTROL/MONITOR
MON MONITOR

Fig. 1. X-band exciter functional block diagram

Fig. 2. X-band exciter phase control loop
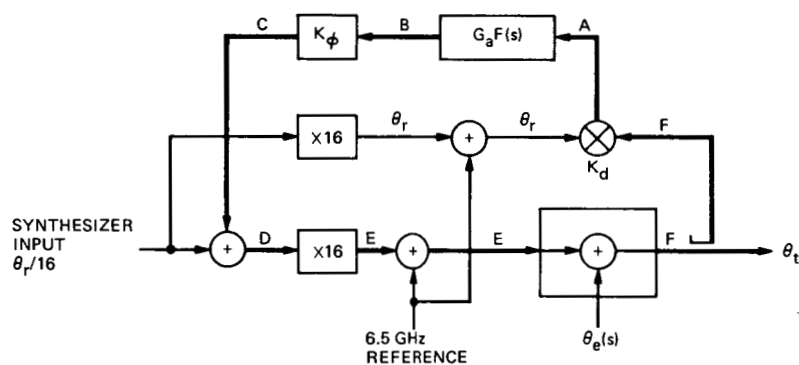
POINT	FUNCTION		DEFINITIONS
A	$(\theta_r - \theta_t) K_d$	θ_r	REFERENCE EXCITER PHASE
B	$(\theta_r - \theta_t) K_d G_a F(s)$	θ_t	TRANSMITTER OUTPUT PHASE
C	$(\theta_r - \theta_t) K_d G_a K_\phi F(s)$, $F(s) = 1/(RCs + 1)$	$\theta_e(s)$	TRANSMITTER PHASE PERTURBATIONS
D	$\theta_r/16 + (\theta_r - \theta_t) K_d G_a K_\phi F(s)$	K_d	PHASE DETECTOR GAIN, 0.0057 V/deg
E	$\theta_r + 16 (\theta_r - \theta_t) K_d G_a K_\phi F(s)$	G_a	DC AMPLIFIER GAIN, 3.85 V/V
F	$\theta_r + 16 (\theta_r - \theta_t) K_d G_a K_\phi F(s) + \theta_e = \theta_t$	K_ϕ	43 MHz VOLT. CONTROLLED PHASE SHIFTER GAIN, 285 deg/V

POINT F GIVES: $\theta_t = \theta_r + \theta_e$ (s) $(RCs + 1)/(RCs + 16 G_a K_d K_\phi + 1)$

THE EXTREME RIGHT TERM YIELDS THE LOOP TRANSFER FUNCTION:

$\theta_t/\theta_e(s) = H(s) = (RCs + 16 K_d G_a K_\phi + 1)$

F(s)	LOOP TRACKING FILTER, I/(RCs + 1), RC = 8 secs
s	LAPLACE COMPLEX FREQUENCY VARIABLE

Fig. 3. Exciter phase correcting loop, mathematical model

Fig. 4. Exciter phase control loop response
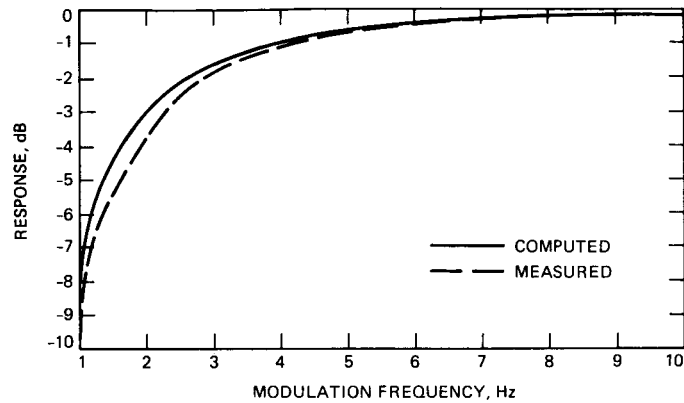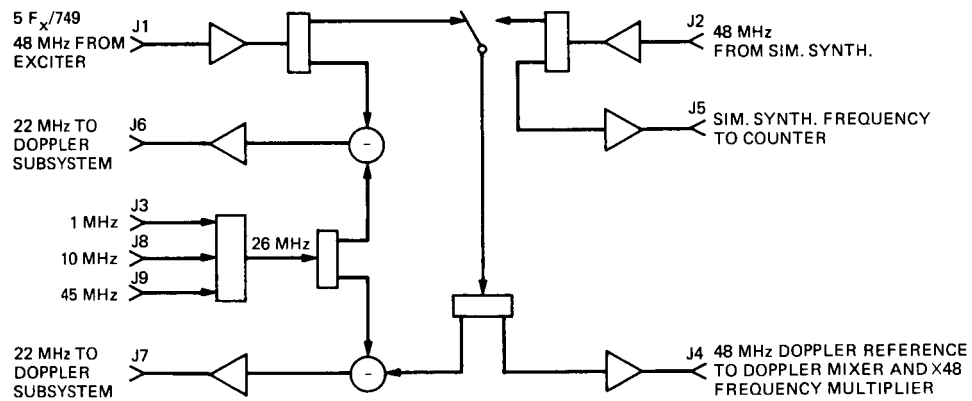

Fig. 5. Doppler reference distribution

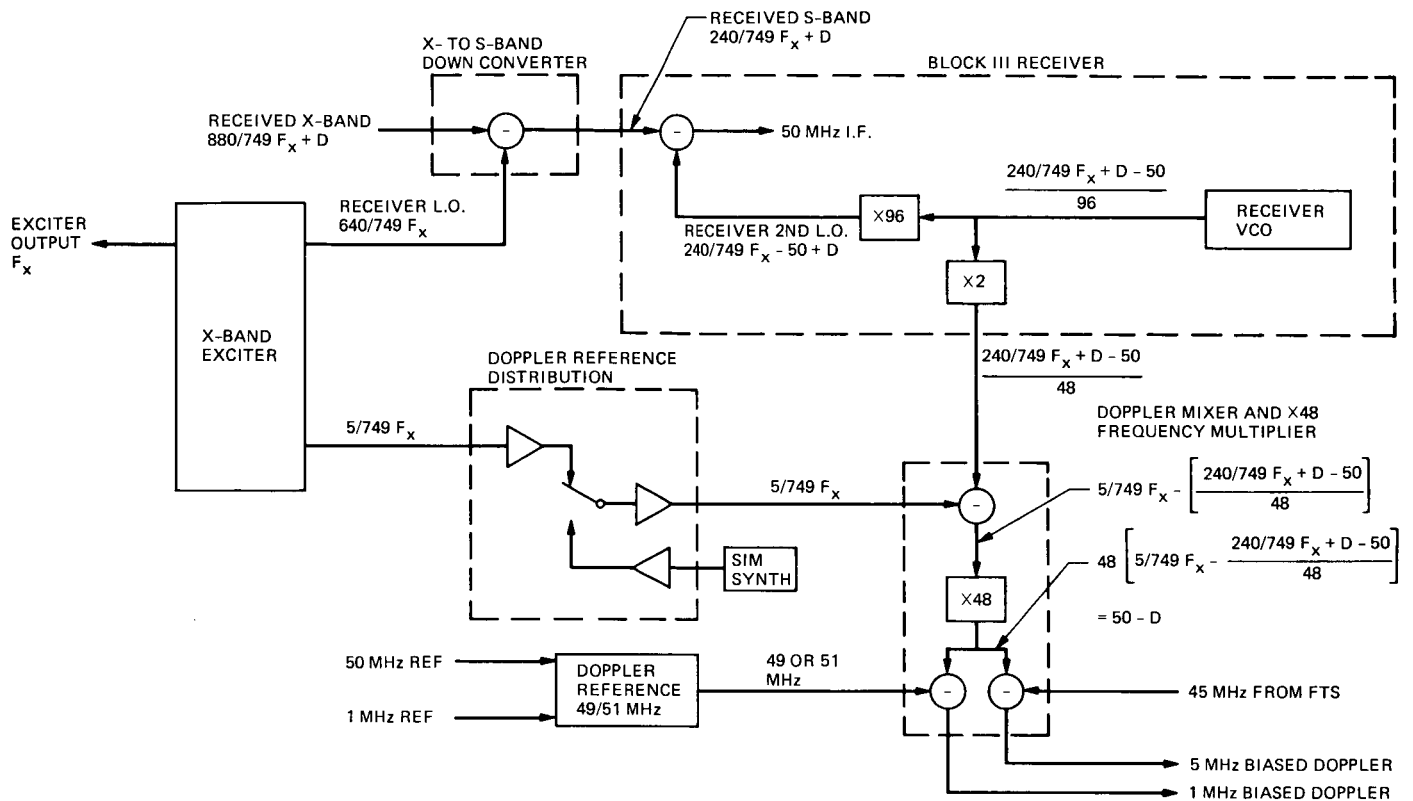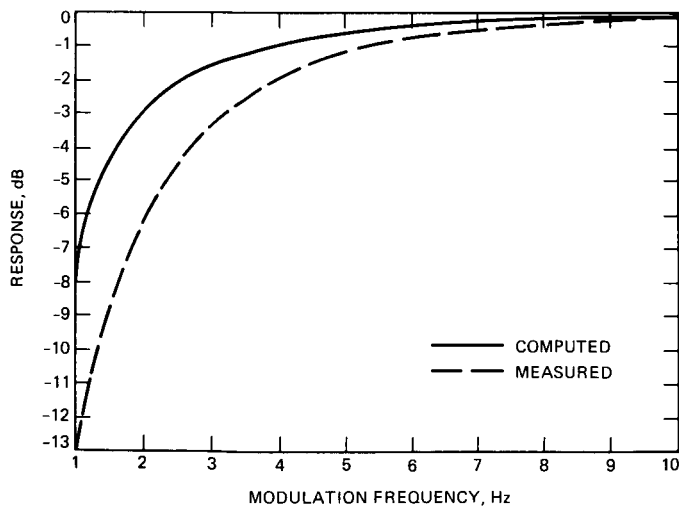**Fig. 6. Block III X-band doppler extraction**

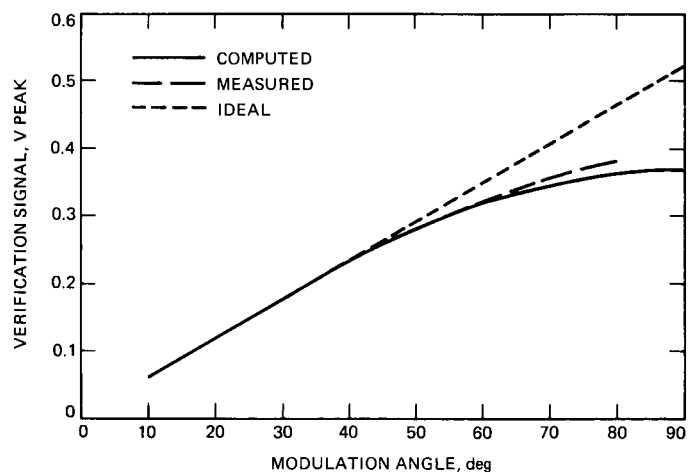**Fig. 7. Command verification loop response**

Fig. 8. Command verification level vs modulation voltage

Dual-Polarization 8.45 GHz Traveling-Wave Maser

R. B. Quinn

Radio Frequency and Microwave Subsystems Section

An 8.45 GHz dual-channel, dual-polarization traveling-wave maser (TWM) amplifier has been installed in the XKR solar system radar cone at DSS 14. The TWM is based on the Blk IIA 8.45 GHz maser structure, with two of the four maser stages being used for each channel, and each maser half then followed by a high-performance GaAs FET amplifier to achieve the desired net gain. A new shortened low-noise input waveguide and an orthogonal-mode junction which is cooled to 4.5 K feeds each amplifier chain. The rotation of an external polarizer permits the polarization of each channel to be defined as either linear or circular. A new circular waveguide switch was also developed to provide for noise calibration and to protect the maser from incident transmitter power.

I. Introduction

The need by radio astronomers to receive simultaneous 8.495 GHz radar signals of right- and left-hand circular polarization prompted the design and installation into the XKR cone at DSS 14 of an 8.45 GHz dual-channel, dual-polarization traveling-wave maser/closed-cycle refrigerator system (TWM/CCR) which replaced the original single channel TWM/CCR. The new system has the following characteristics: (1) two channels with a center frequency of 8.45 GHz, a net gain of ≥45 dB, and an instantaneous bandwidth of 100 MHz, (2) polarization of either channel selectable to right-circular polarization (RCP), left-circular polarization (LCP), or linear polarization, (3) system noise temperature of 20 K or less, and (4) use of the existing feedhorn and rotary polarizing section.

II. Description

The block diagram of the new TWM/CCR system developed for this project is shown in Fig. 1. It was determined that the requirements could be best met by dividing a Blk II 8.45 GHz maser into two channels of two maser channels each, and incorporating an orthomode junction into the cryogenic package, along with the maser amplifier structure. Therefore, only one waveguide input and vacuum window through the CCR interface would be required. The microwave feed system in the center position of the XKR cone provides separation of RCP and LCP by means of a rotating quarter-wave polarizing section and an orthomode junction. By indexing the polarizing section 90 degrees, the channel through which each signal (RCP or LCP) is amplified can be changed. A new and smaller orthomode junction was purchased from Altantic Microwave Corporation. Because of the reduced size of this device, it was possible to place it inside the CCR, where it would operate at 4.5 K, thus reducing its noise contribution. The existing feedhorn interface and polarizing section are 3.48 cm diameter circular waveguide. A smaller waveguide diameter was used in the design of the waveguide switch, vacuum window, and low-noise input structure in order to minimize the probability of RF mode conversion that might occur if the larger waveguide was used. An adapter was designed and supplied to join these two different size waveguides. The signal outputs come out through a pair of 0.36 cm diameter coaxial cables to hermetically sealed SMA connectors at the CCR vacuum interface. Two

other SMA connectors are available to couple noise calibration signals or test signals into the maser inputs via cryogenically cooled −30 dB directional couplers. A high-performance, low-noise GaAs FET post amplifier follows each maser channel to achieve the desired net gain.

A. Traveling Wave Maser Assembly

The Blk IIA maser structure [1] is made up of four independent stages operating in a single superconducting magnet assembly and joined in series by coaxial semirigid cables. It was thus possible to divide the maser into two separate maser channels of two adjacent stages each. The maser gain and bandwidth of each channel is adjusted as a single unit by shaping the applied magnetic field to achieve an average gain of 8 to 10 dB per stage and a −3 dB bandwidth of >100 MHz.

B. Closed-Cycle Refregerator Assembly

The entire maser/magnet assembly is cooled by 4.5 K by the same closed-cycle helium refrigerator (CCR) that is used in the Blk IIA systems. Modifications of the assembly were made to provide for maser output and noise calibration input signals and for the inclusion of the orthomode junction. The modification consisted of replacing the Blk IIA output waveguide and the 4–K station support with two tubular support assemblies, through which the four coaxes enter the CCR. The radiation shields were redesigned to provide room for the added components and a heat strap was added for conduction cooling of the orthomode junction to 4.5 K. As was the case for the Blk IIA maser, the radiation shields were nickel-plated to protect the copper surfaces and reduce the radiant heat load on the CCR. When the refrigeration capacity measured lower than expected on this dual-channel system, it was discovered that electroless nickel rather than electroplated nickel had been applied to the shields. The result was a surface having poor infrared reflectivity. The infrared reflectivity was improved and the refrigeration capacity increased by gold-plating the shields. Reserve capacity measurements were made before and after gold-plating and with and without the low-noise input waveguide structure and orthomode combination. The results are shown in Table 1.

Cryogenic temperature sensors from Lake Shore Cryotronics were installed in the CCR to measure the three refrigerator stage temperatures. Presently, there is no provision to monitor these sensors in the control rack, but the stage temperatures can be measured locally during maintenance.

C. FET Post-Amplifiers

Two high performance GaAs FET amplifiers were purchased from Berkshire Technologies, Inc. The FETs were opti-

mized for operation at room temperature and have an ambient noise temperature of <125 K. Each amplifier has an isolator on the input and output connectors to provide unconditional stability and to improve the VSWR. The amplifiers are mounted on the TWM/CCR mounting brackets on each side of the CCR. The power supplies for the amplifiers are built into a common enclosure that is mounted to the side of the maser package.

The original system design called for cryogenic cooling of the post-amplifiers, but the performance of the maser exceeded that of the average Blk IIA maser, making the use of post-amplifier cooling unnecessary. Placing the post-amplifiers outside the CCR resulted in a higher reserve refrigeration capacity and hence a more reliable maser system.

D. Orthomode Junction

A special orthomode junction was made for JPL by Atlantic Microwave Corporation since the DSN's primary frequency range of 8.4 GHz to 8.5 GHz fell between their standard catalog models. The assembly is copper-plated for low electrical loss. The device provides isolation between cross-polarized components of >40 dB and a VSWR of better than 1.15:1.

E. Low-Noise Input Waveguide Assembly

A new shortened input waveguide assembly was designed to allow for the added length of the orthomode junction within the same CCR vacuum housing. A cross-section diagram of the new assembly is shown in Fig. 2, and a photograph of the assembly with the cooled orthomode attached is shown in Fig. 3. Figure 3 also shows the existing Blk IIA low-noise input waveguide assembly for comparison. While the new design is shorter by >50%, it provides an improvement in thermal isolation over the low-noise input assembly in the Blk IIA maser. This was achieved by replacing stainless steel construction with G–10 CR fiberglass as a rigid structural material. The normally poor infrared reflectivity of the fiberglass material was improved by vacuum-depositing approximately 1500 angstroms of gold. This assembly is able to maintain precise axial relationships between waveguide sections and maintain correct spacing of the RF choke joint gaps while minimizing the heat leak into the CCR through the structural material. As seen in Table 1, this input waveguide assembly (and orthomode junction) contributed 100 mW of heat load to the CCR.

F. Output Coax/Support Assembly

A pair of special coax/support structures was designed and installed in the CCR. These structures furnish structural support for the maser/magnet assembly while providing an enclosure and feed through location for the four coaxial cables and connectors required for signal output and calibration signal

input. The 0.36 cm diameter coaxial cable used for output lines and noise source input lines was especially chosen for cryogenic applications. It has an outer conductor of stainless steel and an inner conductor of silver-plated beryllium copper. This type of coax is desirable in cryogenic applications because of its low microwave insertion loss and relatively low thermal conductivity.

G. Waveguide Switch Assembly

A waveguide switch is required between the feedhorn and the maser to protect the maser and receiver from incident transmitted power. The waveguide switch is also used to switch the maser to an ambient termination for system noise calibration. In a conventional waveguide switch, such as those used in DSN receiving systems, a rotating member is used between the waveguide ports. This type of switching mechanism was not usable because of the mechanical and microwave performance difficulties associated with circular waveguide bends in a switch rotor. Therefore, a new kind of linear waveguide switch for circular waveguide was designed and built (shown in Fig. 4). A DSN-type drive mechanism (for compatibility with DSN control wiring) is used to move a sliding shuttle on linear bearings. At one end of the 5.08-cm travel, a through-path exists, while at the other end, the shuttle contains a tapered circular ambient termination (looking toward the TWM), and a short circuit (looking toward the feedhorn).

H. Wide Tuning Range Pump Source

The new TWM replaced a Blk I 8.45 GHz maser that had been used on occasion at frequencies outside those normally used by the DSN. The tuning range of the maser within the particular structure bandpass is determined by the tuning range of the pump source, which is an electronically tunable klystron or Gunn effect oscillator. The source used to pump the Blk IIA TWM uses a pair of Gunn effect oscillaors designed to support maser operation from 8.4 GHz to 8.5 GHz. The oscillators are tuned by means of a negative biased varactor diode. The Radio Astronomy Group furnished funding for the purchase of specially designed Gunn effect oscillators that would allow the TWM to be tuned to the usual Blk IIA frequencies and also to 8.67 GHz. This higher frequency is re-quired for the Interstellar Microwave Spectroscopy task. The new oscillators, made by Central Microwave Corporation, are unlike the Blk IIA oscillators in that they require a positive tuning varactor voltage. The bias voltage change was accomplished by making wiring changes in the maser pump source and in the solid-state pump controller and by replacing the voltage protection/modulation assemblies in the pump source. Because of these changes, the pump source and controller for this TWM are now a matched pair and are not interchangeable with similar components in Blk IIA maser systems. This new pump source allows TWM operation from 8.4 GHz to 8.7 GHz, with approximately 100 MHz of bandwidth.

III. Performance

The gain/bandwidth curves and noise temperature measurements shown in Figs. 5 and 6 were measured in the laboratory prior to replacement of the cryogenically optimized post-amplifiers with those optimized for room temperature operation. The total gain is now about 4 dB less than shown, but the system noise temperature on the antenna was improved by 0.5 K, for a total system temperature of approximately 20 K.

The isolation between the two polarization channels was measured on the antenna with the use of a test probe mounted over the feedhorn. The isolation between RCP and LCP channels exceeded 17 dB.

IV. Conclusions

This new dual-channel, dual-polarization TWM system demonstrates the ability to incorporate more than one maser amplifier into one CCR and also to lower the total system temperature by the cryogenic cooling of components that had previously operated at room temperature. This accomplishment was due to improvements in FET post-amplifier noise performance, the availability of a compact orthomode junction, the design of a new cryogenic low noise input waveguide structure, and the development of a suitable waveguide switch in circular waveguide.

References

[1] D.L. Trowbridge, "Block IIA Traveling Wave Maser," *TDA Progress Report 42-87,* vol. July–September 1986, pp. 158–164, Jet Propulsion Laboratory, Pasadena, CA, Sept. 15, 1986.

Table 1. Reserve CCR heat capacity

	Without low-noise input assembly and orthomode junction	With low-noise input assembly and orthomode junction installed
Electroless nickel plating on copper radiation shields	444 MW	340 MW
After gold plating of radiation shields	690 MW	590 MW
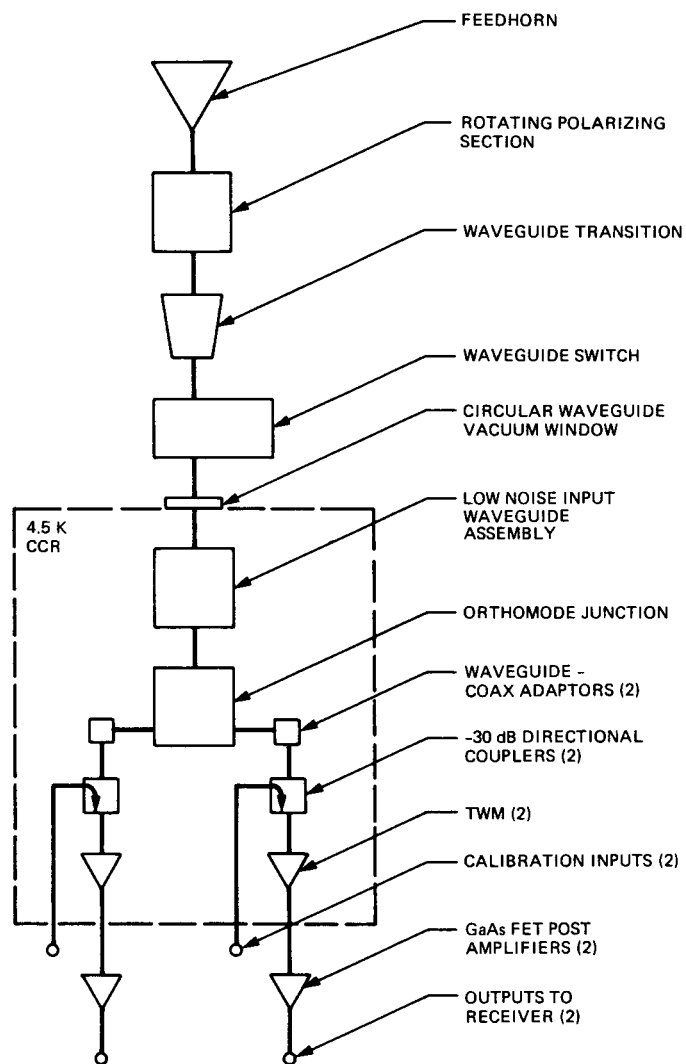
Fig. 1. Block diagram of 8.45 GHz dual polarization TWM/CCR

Labels in figure:
- FEEDHORN
- ROTATING POLARIZING SECTION
- WAVEGUIDE TRANSITION
- WAVEGUIDE SWITCH
- CIRCULAR WAVEGUIDE VACUUM WINDOW
- LOW NOISE INPUT WAVEGUIDE ASSEMBLY
- ORTHOMODE JUNCTION
- WAVEGUIDE - COAX ADAPTORS (2)
- -30 dB DIRECTIONAL COUPLERS (2)
- TWM (2)
- CALIBRATION INPUTS (2)
- GaAs FET POST AMPLIFIERS (2)
- OUTPUTS TO RECEIVER (2)
- 4.5 K CCR

MICA VACUUM WINDOW

STYROFOAM THERMAL
RADIATION BLOCKS (THREE PLACES)

VACUUM HOUSING FLANGE

300 KELVIN FLANGE

RF CHOKE GROOVE

G-10 FIBREGLASS TUBE SUPPORT STRUCTURE
FURNISHES THERMAL ISOLATION BETWEEN 300,
70, & 4.5 KELVIN WAVEGUIDE SECTIONS.
SURFACES ARE GOLD DEPOSITED TO IMPROVE
EMISSIVITY AND REDUCE THERMAL LOAD ON
CLOSED CYCLE REFRIGERATOR.

70 KELVIN WAVEGUIDE SECTION

70 KELVIN RADIATION SHIELD INTERFACE

4.5 KELVIN FLANGE

RF CHOKE GROOVE

ATLANTIC MICROWAVE POLARIZER,
CONDUCTION COOLED TO 4.5 KELVIN

Fig. 2. Cross section of low noise input waveguide assembly

Fig. 3. New low noise input waveguide assembly and orthomode compared with Blk IIA low noise input waveguide assembly

Fig. 5. Gain/bandwidth curves, TWM tuned to 8.495 GHZ

Fig. 4. Cross section of circular waveguide switch

Fig. 6. Equivalent input noise temperature vs frequency curves with TWM tuned to 8.45 GHz

p-1

An Interactive Wire-Wrap Board Layout Program

A. Schlutsmeyer

Communications Systems Research Section

This article presents an interactive computer-graphics-based tool for specifying the placement of electronic parts on a wire-wrap circuit board. Input is a data file (currently produc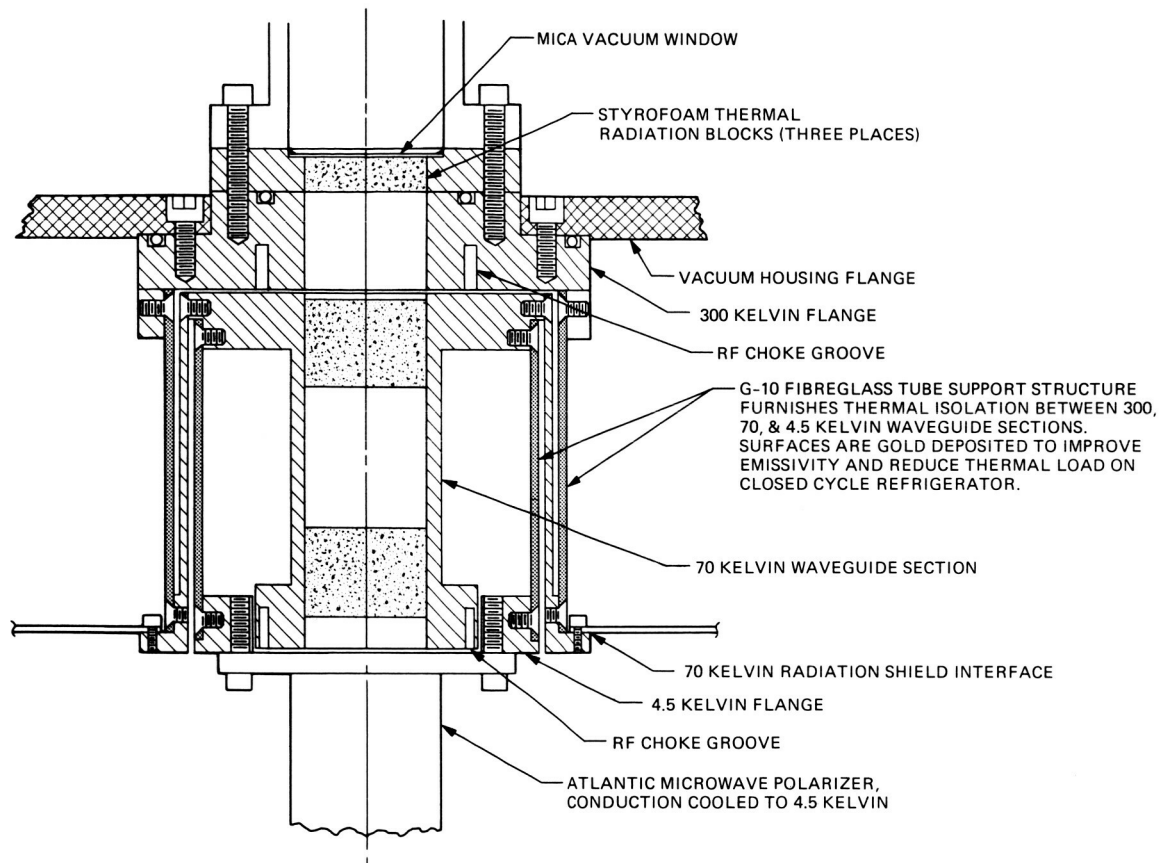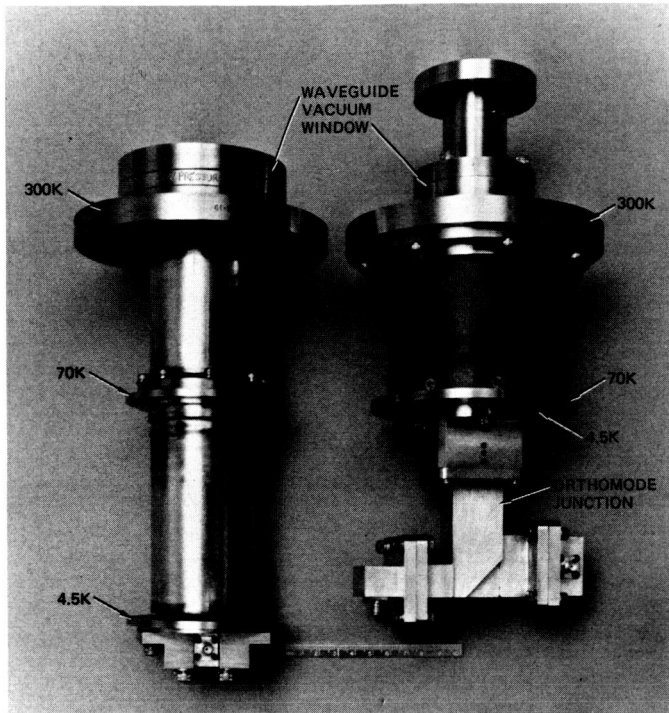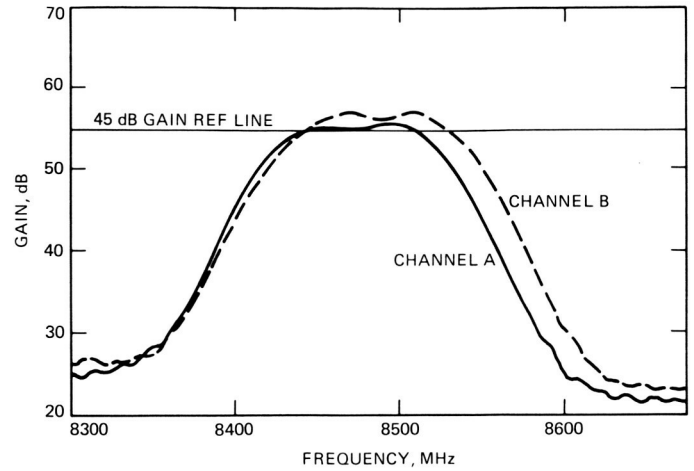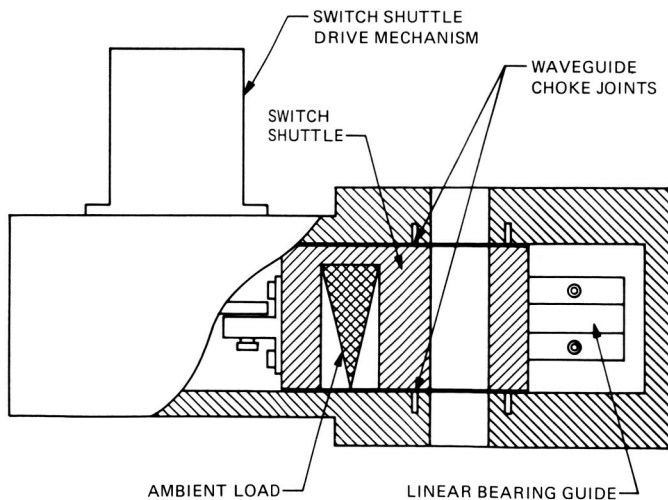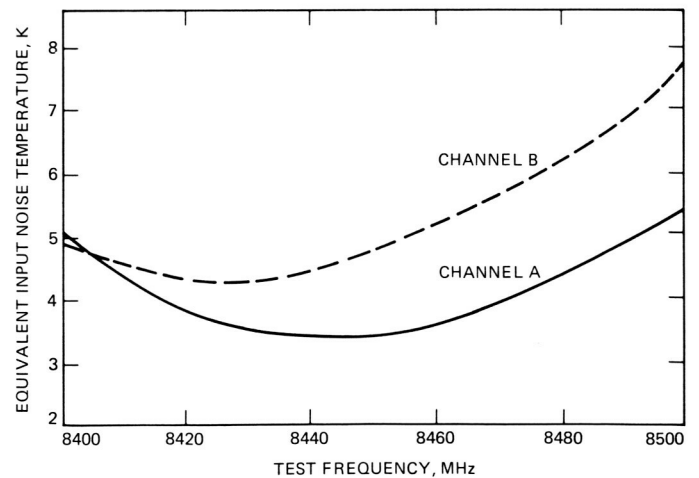ed by a commercial logic design system) which describes the parts used and their interconnections. Output includes printed reports describing the parts and wire paths, parts counts, placement list, board drawing, and a tape to send to the wire-wrap vendor. The program should reduce the engineer's layout time by a factor of 3 to 5 as compared to manual methods.

This program will benefit several projects at JPL, including the Advanced Digital SAR Processor and the Alaska SAR Processor. It is currently being used in the design of the DSN/SETI Spectrum Analyzer.

I. Introduction

The Communications Systems Research Section, Digital Projects Group (DPG), is currently designing several machines which will make extensive use of wire-wrap board technology. This technology allows a rapid turnaround time from design to production, and somewhat simplifies the design process. While printed circuit boards are cheaper to manufacture in quantity, the DPG's projects are mostly one-of-a-kind designs, and thus wire-wrap technology is more appropriate.

The DPG recently procured a Valid Logic Design computer system (a commercial product of Valid Logic Systems, Incorporated, of San Jose, California), which provides a tool for the computer-aided design of logic circuits. Several computer packages are available to turn such a design into a printed circuit board layout. However, no computer tool existed to turn the logic design data files into a physical layout of a wire-wrap board.

DPG engineers estimate that the manual layout of a board takes about 3 weeks. Computer-aided layout could reduce that time to 5 days or less. Since the DPG will design 30 or more boards in the next few years, a computer-based layout system will produce substantial cost and time benefits. Therefore, the decision was made to develop a system in-house.

II. System Description

Figure 1 shows a system block diagram of the logic design and layout system. The Valid Logic Design system and the file conversion program reside on an IBM 3270 AT/GX system. The rest of the system currently resides on a Masscomp

MC5600 system with an Aurora color graphics display. The programs written by the DPG include the file conversion program, the layout program, and the library editor program. These programs are written in the C programming language, and are machine independent and graphics-resolution independent.

The Valid Logic Design system produces files defining the parts used and the interconnections between them. The file conversion program reads these files and extracts the information needed by the layout system. The library editor program maintains the wire-wrap board descriptions and the physical-part description library.

The layout program reads the files provided by the file conversion and library editor programs, and then asks the engineer which wire-wrap board to use. Then the program displays a picture of the board; the designer can then select components from the logical design file and place them on the board graphically. The program optimizes wire routing, but the designer can manually override part or all of the routing. Several editing and display functions help the designer to accomplish these tasks. An intermediate file, called the layout data file, records the developing layout information while the design is in progress.

Once the layout is complete, the program prepares a wire-list tape to be sent to the wire-wrap vendor. Also, several reports are printed out to document the final design and to aid the engineer during debugging.

III. Wire Routing Optimization

One strong feature of the layout program is the ability to minimize wire path lengths. The basic problem is to minimize the wire length of an interconnected set of pins (a net). This is desirable for several reasons:

(1) Reduces cost.

(2) Reduces signal propagation delays.

(3) Reduces "ringing" effects and cross-coupling.

The wire routing optimization algorithm is an extension of the method described in [1]. The original algorithm treats all pins as identical. The extended algorithm recognizes special pins ("drivers" and "terminators") and groups these at the front and back of the net, respectively. While maintaining these groupings the entire net is minimized. This technique greatly reduces the need to manually override the results of the minimization process.

The time required to minimize a net increases rapidly with the number of pins in the net. To prevent long nets from taking

extremely long times, the algorithm automatically stops if the minimum has not been exhaustively determined after a certain number of iterations, and uses the best order found so far. This "partial minimum" is usually close to the real minimum.

IV. Layout Program Description

A. Display Areas

Figure 2 shows the menu and screen display of the layout program. There are five distinct display areas:

(1) Board display.

(2) Selected part/net display.

(3) Data display.

(4) Parts list.

(5) Function menu.

1. Board display. This area shows the wire-wrap board and those parts which have already been placed on the board. This area also shows individual signal paths or highlights parts of a certain type if requested.

2. Selected part/net display. This area shows an individual part outline, along with its physical part name and pin names. Alternatively, this area shows the list of parts/pins connected to a single net.

3. Data display. This area shows data related to the current editing function and context. Examples of data shown are: the location of pin 1 of the currently selected part, the number of pins connected to the currently selected net, and the total wire length of the currently selected net.

4. Parts list. This area shows an alphabetically arranged list of the logical names of all the parts in the design. The list scrolls up and down, and the name of the currently selected part is highlighted. When the "show part type" function is selected, this area instead displays a list of physical part names.

5. Function menu. This area shows the available editing and display functions. Currently chosen functions are high-lighted. The functions are:

a. Save and exit. This saves the current state of the layout design, and then exits to the operating system.

b. Abandon and exit. This exits to the operating system without saving the current design state. This takes less time than "save and exit," and is useful when you have experimented with the design but don't wish to save the results. If

any changes have been made, this function asks for confirmation before exiting.

c. Zoom out. This sets the board display area to view the entire board.

d. Zoom in. This sets the board display area to view a local area of the board, magnified by 3. The next pick on the board display area indicates the center of the area to be magnified. One of "zoom out" or "zoom in" will always be selected.

e. Show part. This shows the currently selected part outline, logical name, etc., in the selected part/net display area.

f. Show pin list. This shows the currently selected net (if any) in the selected part/net display area.

g. Replicate. This is similar to a "copy" operation. Each part in the currently selected group is deselected, and the next part in the logical parts list is selected in its place. Each new selected part is given the same initial location as its predecessor, so the new group is a "spatial replicate" of the old one. This new group may then be dragged around and placed as the old one was.

h. Suppress sorting. This prevents the program from performing net minimization each time a part is placed. If a part is connected to a particularly long net, sorting could slow down editing too much. Picking this function repeatedly toggles it on and off.

i. Group. This allows the user to specify, one at a time, a group of parts on the board display to be repositioned or removed. Each part picked on the board display is toggled between selected and deselected. Picking this function repeatedly toggles it on and off.

j. Group by box. This allows the user to specify, by corners of a rectangular area, a group of parts on the board display to be repositioned or removed. The next two picks on the board display define the rectangular selection area. Picking this function repeatedly toggles it on and off.

k. Show part type. This replaces the logical name list in the parts list area with a list of the physical part types used. Picking a physical part from this list causes all parts of that type to be highlighted in the board display area.

l. Show long nets. This highlights on the board display the wire path of the net with the greatest wire length. Picking this function repeatedly steps through successively shorter nets, displaying one at a time. Note that only already minimized nets are considered for this function.

Note that the functions "group", "group by box", "show part type," and "show long nets" are mutually exclusive, and that they set the selected part/net display as follows:

Function	Sets display to
Group	Nothing
Group by box	Nothing
Show part type	Show part
Show long nets	Show pin list

m. Undo. This reverses the effect of the last editing operation.

n. Long cursor. This changes the cursor to a full-screen crosshair. This is useful for aligning objects during placement. This option is toggled on and off by picking it repeatedly.

B. Editing Terms and Concepts

This section contains descriptions for performing most editing operations, using the Masscomp MC5600 system implementation of the layout program. This system uses a mouse for graphic input. In these descriptions, certain words have special meanings:

(1) "pick" means move the cursor over an object and press either outside button on the mouse.

(2) "place" occurs when you are dragging an object(s). When the object is located where desired, press either outside button on the mouse.

(3) "drop" means press the center button the mouse.

Note that you never need to hold a mouse button down (e.g., to drag an object). Always release the button immediately.

Placing, moving, swapping, and removing parts in the board display area, as well as displaying parts and net wires, overriding net minimization, and swapping pins are all accomplished by pointing the cursor at objects on the screen and pressing the mouse buttons. Certain keyboard keys have meaning as well.

The following concepts are basic to the editing philosophy.

1. Currently selected part. Normally, a single part is selected for editing operations. This part is highlighted both in the parts list and in the board display area. Also, the drawing of the part appears in the selected part/net display area. A

part may be selected either by picking its name from the parts list or by picking its outline from the board display.

When using the group functions, more than one part may be selected at once. All selected parts are highlighted, but no part drawing appears in the selected part/net display area.

2. **Placed vs dropped.** Each part is in one of two possible states: "placed" or "dropped." If it is placed, it has a fixed position on the board associated with it. If it is dropped it does not occupy a position on the board display.

3. **Currently selected net.** A net is selected by picking a signal name from the selected part display. When a net is selected, its net name, wire length, and number of pins appear in the data display, and if any pins from the net are in parts placed on the board display, these pins are highlighted as well.

C. How-to's

To place a new part, pick the part name from the parts list, then move to the board display and place the part in the desired position. The data display area helps by dynamically showing the pin location of pin 1 until the part is placed.

To move an already placed part, pick up the part by its outline in the board display, then move it to the new location and place it. Again you see the dynamic pin 1 location display.

To drop a part which is following the cursor, press the drop button on the mouse. The part outline will disappear and there will be no currently selected part.

To remove a part from the board, move the cursor to the part on the board display and press the drop button. The part will disappear from the board. Any currently selected parts (if not the one just removed) will remain selected.

To move a block of parts, first use the "group" or "group by box" function to select the desired parts. Next turn the group function off. Then move the cursor to the board display area and pick up the group, move it to the new location, and place it again.

To remove a block of parts, first select the group as described just above, then press the drop button.

To replicate a block of parts, first select the group as described above, then select the replicate function from the function menu. Each item in the current group is deselected, and the next item in the list is selected in its place. Then move the cursor to the board display area, pick up the new group, move it to its new location and place it again.

To select a part for display, pick the part name from the parts list. The part display will appear. Alternatively, pick the part outline in the board display, then place it immediately without first moving the mouse. The part display will appear, and the part will still be in place.

To display a net, first select a part which has at least one pin connected to the desired net. Then pick the connected pin from the part display in the selected part/net display area. The net name, length, and number of pins will appear in the data display area, and any pins connected to the net will be highlighted on the board display area.

D. Keyboard Commands

In certain contexts various keyboard keys are interpreted as commands. The keypresses are not echoed to the screen; the effect of each command is visually apparent on the screen. If a key has no meaning in the current context, pressing that key will merely result in a beep.

Pressing any cursor arrow key causes all currently selected parts to move to the next unoccupied pin position in the arrow direction. If there is no unoccupied position left in the indicated direction, the program beeps.

Typing the "/" key drops each currently selected part and selects the next part in the parts list. If the previously selected part was "placed," it stays where it was. Typing the "\" key selects the previous part in the same manner.

Typing any alphabetic character or numeric digit causes the parts list display to move to part names starting with that character or greater.

Typing the "+" key advances the parts list display by 3/4 page. Typing the "−" key backs up the parts list display by the same amount.

Typing a carriage return is the equivalent of pressing the mouse "place" or "pick" button.

Typing the DEL key is the equivalent of pressing the mouse "drop" button.

By combining the above key commands it is possible to rapidly place arrays of parts whose names are alphabetically close together.

V. Conclusions

The DPG has used manual and semiautomatic wire-wrap board layout methods for many years. This in-depth applica-

tions knowledge, combined with graphics expertise, has produced a very useful computer tool. Layout program features are confined to those operations which are truly useful to a design engineer. Output reports are organized to aid circuit testing. The input file format is simple and generalized, easing the process of interfacing to any design system.

The layout program has taken about 3 workmonths to produce. The DPG alone will lay out more than 30 board designs using this system, thus saving at least 1 workyear of effort on the DSN SETI spectrum analyzer. This same technique could be used widely throughout NASA to improve the digital systems design process.

Reference

[1] M. J. Grimm, "A simple algorithm for the metric traveling salesman problem," in the *TDA Progress Report 42-78*, pp. 108-114, Pasadena, California: Jet Propulsion Laboratory, August 1984.
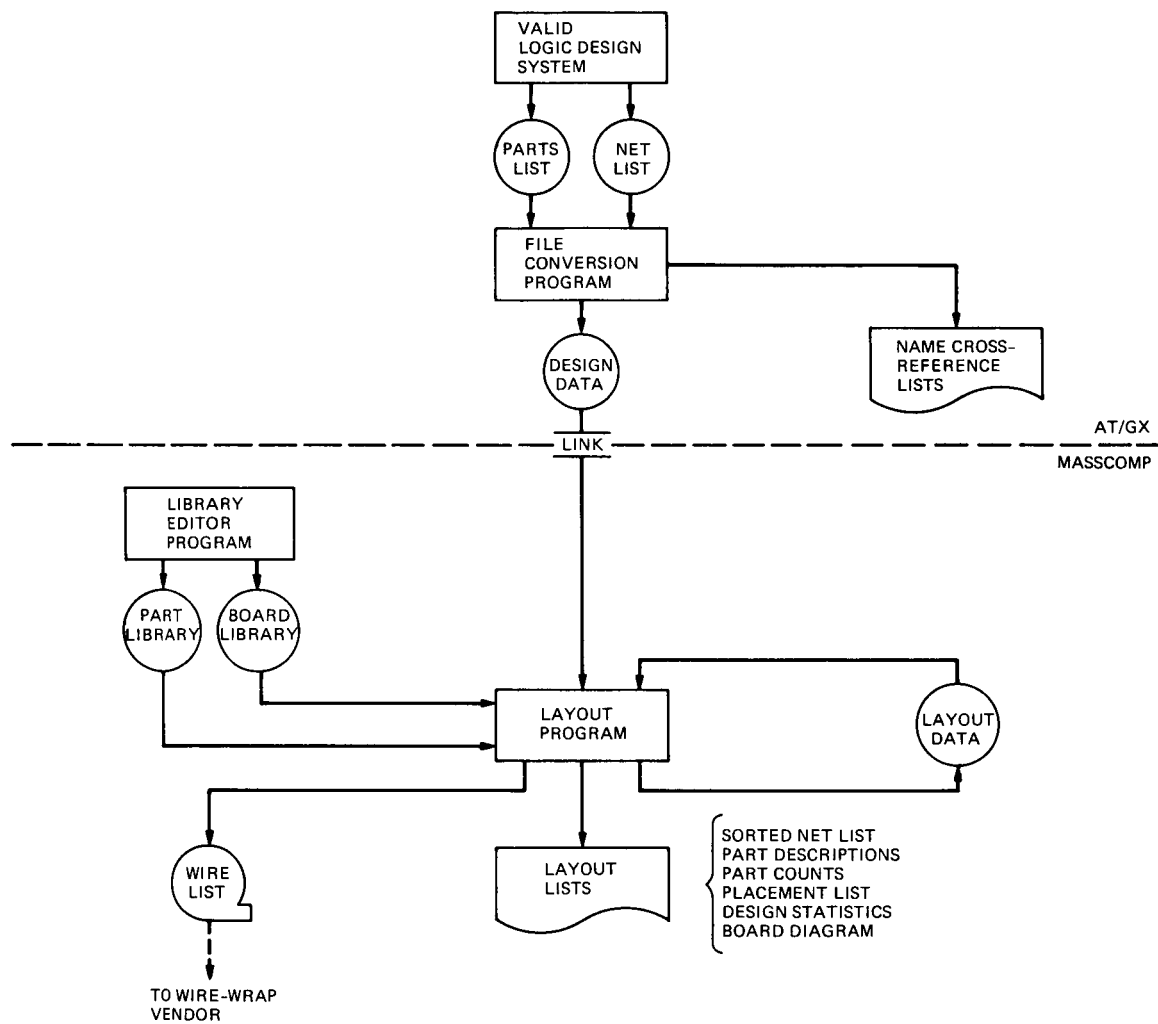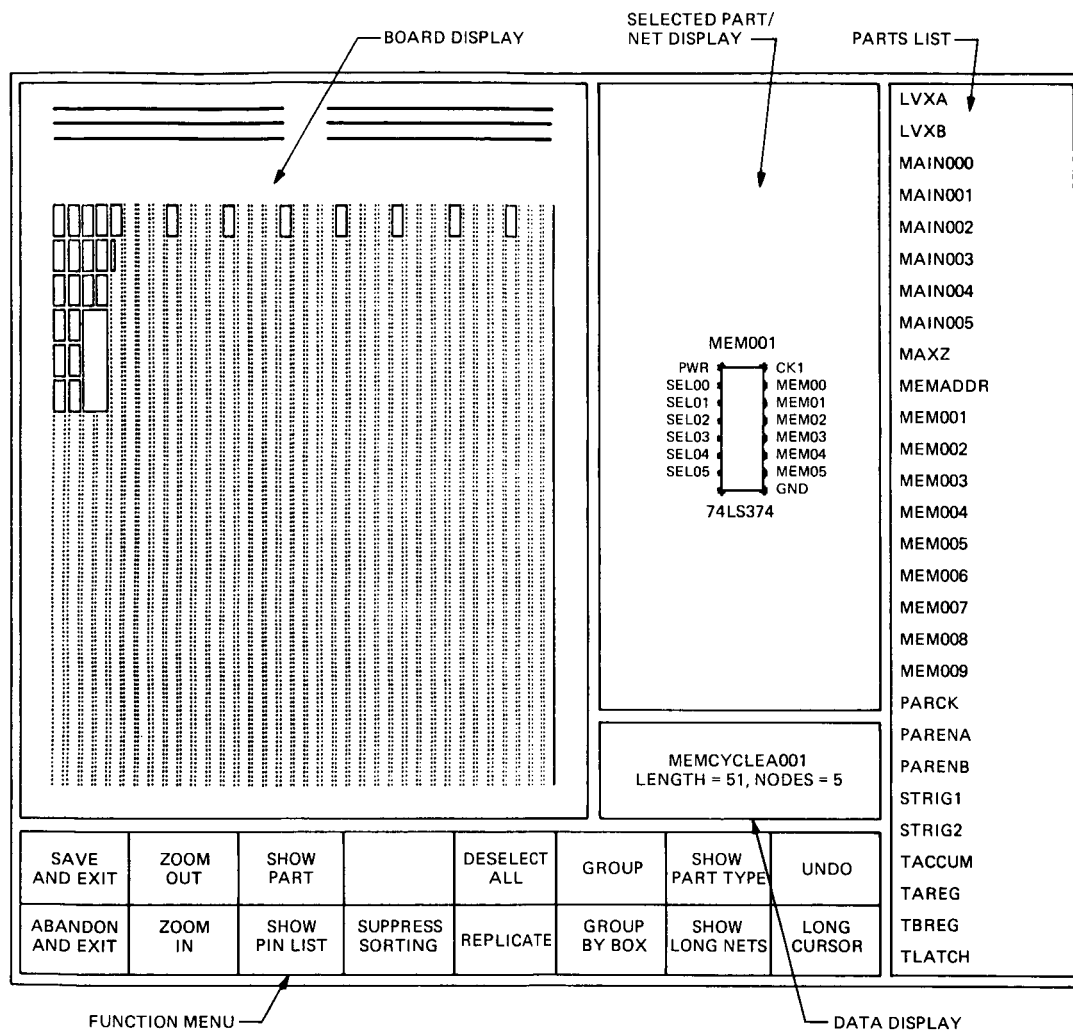
Fig. 1. Layout system

Fig. 2. Layout program screen display

p/p

An Evaluation of the Communication System for the TAU Mission Study

B. D. Metscher

Communications Systems Research Section

The requirements for possible microwave and optical frequency communication systems to return 20 kbps from 1000 AU are compared and sample telemetry links are calculated. Microwave systems were found to have impractical parameter requirements, while the required optical system parameters are much more feasible. A first-level design of an optical communication link is presented; this design can be implemented with conservatively projected technology development. Optical background noise can be either tolerated or eliminated and it was found that TAU could detect a laser beacon from Earth even if Earth were in front of the sun.

I. Introduction

TAU is a proposed mission currently under study at JPL to send a probe to a distance of one thousand astonomical units (AU). Among the possible science objectives for this mission are high-precision astrometry using a 1000-AU baseline, low-frequency radio astronomy, measurements of the interstellar medium, and imaging of our solar system from the outside. These and other science experiments on TAU will require a communication system capable of returning data to Earth from 1000 AU at rates of up to 20 kilobits per second (kbps). In this study, possible radio-frequency (Ka–band, 32 GHz) and optical-frequency (532 nm) communications systems were examined and their requirements and capabilities assessed.

The radio-frequency technology currently used for deep space communications has several advantages over the less mature optical technology. A microwave communication system for TAU would require less developmental work. A microwave transmission beam need not be pointed as accurately as a more tightly focused optical beam and power conversion efficiencies are generally higher for radio transmitters than for lasers. Microwave communication links can use ground based receiving antennas, whereas optical frequencies are attenuated far more by the atmosphere and will probably require space-based receiving telescopes for deep-space links.

However, in order to return the 20 kbps required for TAU mission science from a 1000 AU, a microwave system would require transmitting and receiving antennas that are too large to be practical, as well as more power than would be required by an optical system. Given a sufficient power supply, TAU would still require a microwave transmitting antenna at least 10 to 15 meters in diameter and a receiving antenna 200 meters in diameter (or an equivalent receiver array).

Advantages of using an optical communication system for the TAU mission include much lower diffraction limited beam

divergence, much smaller and lighter transmitting and receiving antennas, and the ability to support high data rates.

Design control tables for these two options are presented and the requirements and performance of each is discussed. The design of an optical communications link for TAU is considered further, with an assessment of noise sources, a design table for the uplink, and a brief look at acquisition and tracking.

II. Comparison of Microwave and Optical Communications Links

A. Requirements for a Radio Frequency Link

A Ka-band communications link for TAU would need a transmitter antenna 10 to 15 meters in diameter. Antennas larger than 4.5 m either must be deployable or must be constructed in space. Deployable antennas have more than twice the mass of solid-construction antennas. A 32 GHz (Ka-band) antenna will probably require a surface tolerance of 0.5 mm rms or better.[1] This requirement will increase both the mass and the fabrication cost of the antenna.

Designs for a 15-meter radio antenna have been studied for the QUASAT mission. The surface tolerances of these designs are about 0.5 to 0.8 mm rms and their masses range from 198 kg to 300 kg.[2] The mass of a 10-meter Ka-band antenna has been estimated at 230 kg [1]. The useful ranges of mass models for microwave antennas do not usually extend to 200-meter antennas.

A design control table (DCT) for a TAU Ka-band telemetry link is given in Table 1. This table is based on a DCT for a 1000-AU X-band link given by Jaffe [2] and on a Ka-band link for Cassini given by Dickinson [1], Table 9). Jaffe's link uses a 15-meter transmitting antenna, 40 watts of transmitted power, and a 100-m receiving dish. Assuming a coherent system, his link provides a data rate of 100 bps with a performance margin of 2 dB.

The link in Table 1 assumes a 15 meter transmitting antenna and a 200-meter receiver. "Transmitter losses" (Table 1) include all the antenna efficiency, obscuration, pointing, and line loss factors, taken from Dickinson's link. The transmitter gain was calculated using an antenna efficiency factor of 0.548 (transmitter losses in Table 1), and the space loss was calculated from the usual definition [3].

[1] R. E. Freeland, JPL Applied Technologies Section, private communication, October 1986.

[2] R. E. Freeland, "QUASAT Antenna Technology Study," JPL Internal Document, Jet Propulsion Laboratory, Pasadena, CA, D-3292, Sept. 1986.

The receiver efficiencies and gain were obtained similarly; however, no atmospheric effects were included. These effects would change the "mechanical and other" efficiency factor from 0.769 to 0.677 ([1], Table 9), requiring 130 W of power to maintain a performance margin of 3 dB. This link assumes either that a 200-meter antenna with the efficiencies estimated by Dickinson for improved DSN receiving antennas can be built in orbit, or that a ground-based array of Ka-band receiving antennas is used.

The noise spectral density was taken from Jaffe's paper and assumes an effective noise temperature of 25 K. It may be possible to lower the thermal noise further by using cryogenic amplifiers on a space-based receiver ([2] p. 16).

The total received power is the product of RF output power, transmitter gain, space loss and receiver antenna gain in the table.

Jaffe gives the threshold ST/N_0 (a measure of the required signal-to-noise ratio) for his link based on a bit error rate of 10^{-4} and he computes the ratio of data power to total power received (data power/total power, Table 1) from $(2R_D/(100B_L + 2R_D))$, where R_D is the data rate and B_L is the loop bandwidth ([2], p. 16). A similar calculation was used in Table 1. The threshold data power is the sum of noise spectral density, data rate, and threshold, and the performance margin is then the difference between received data power and threshold data power.

Given a 15-meter transmitter and a 200-meter receiver, 115 watts of DC transmitter power are required to support a data rate of 20 kbps. With a 10-meter transmitter 260 W would be required.

B. Requirements for an Optical Telemetry Link

A DCT for an optical-frequency TAU telemetry link is given in Table 2. This table was calculated using an optical communications link analysis program written by W. Marshall and B. Burk [4]. The input parameters and the results of the calculations appear in Table 2.

The transmitter for this link uses a 1-meter-diameter telescope and a frequency-doubled Nd:YAG laser emitting at 532 nm. A DC-to-optical power efficiency of 8.5% has been demonstrated for a Nd:YAG, and higher efficiencies should be possible with this or other solid-state laser technologies [10]. At an efficiency of 10% the 10-watt laser in this link would require 100 W of DC power.

The receiver for the link in Table 2 is assumed to be a 10-meter-diameter "photon bucket," a non-diffraction-limited

telescope mirror placed in Earth orbit. It is assumed to focus ten times less accurately than would a diffraction limited telescope with the same aperture i.e., the angular diameter of the field of view of a detector at its focus is $10 \times (2.44 \lambda/D)$. An increased field of view allows the detector to receive more light from extended noise sources and perhaps from more stars, but otherwise has little effect on link performance aside from requiring a larger detector area to collect more light from a larger blur spot.

The detector is assumed to be a cooled avalanche photodiode whose single-photon detection probability ("Detector Quantum Efficiency" in Table 2) is 40%. Such sensitivities for these devices have been demonstrated in the laboratory, but their internal noise increases with sensitivity and may become important for probabilities above about 30% [5]. However, the number of noise photoelectrons generated in the detector will probably not exceed a few hundred to a thousand per second, which is less than 10^{-5} electrons per signal pulse. This will have only a small effect on the receiver's performance (see Table 2).

If the transmitter telescope mirror is assumed to be made of beryllium, then its mass may be computed from a model studied by Hughes Aircraft [6]:

$$\text{mass (kg)} = 0.034 \, D^{2.7}$$

where D is the mirror's diameter in centimeters. For the 1-meter mirror, this model gives a mass of 55 kg. The validity of this model for mirrors as large as 10 m is not discussed in the Hughes report.

The optics in both the transmitting and receiving systems are assumed to be 65% transmission efficient *in toto*. This does not include a narrow-band interference filter in the receiving optics. Interference filters with a 10-angstrom bandwidth and 65% peak transmittance are presently available.

The telemetry link uses pulse position modulation (PPM) with a word size of 1024, a data rate of 20 kbps, and a bit error rate of 10^{-4}. A Reed–Solomon code with a coding fraction of 1/2 is assumed and the data rate and error rate values in the table have been adjusted for coding.[3]

Using the input parameters in Table 2, Marshall and Burk's link analysis program calculated a performance margin of 3.1 dB. The expected primary noise sources have been included and are discussed in the next section.

---

[3]W. K. Marshall, JPL Internal Document, Jet Propulsion Laboratory, Pasadena, CA, Interoffice Memorandum 331-86.6-202, August 1, 1986.

III. Optical Communication Link Design Considerations

A. Sources of Optical Noise

The most significant noise source for both the uplink and downlink of a TAU communications system will be sunlight. A useful data rate cannot be maintained if the sun is in the field of view of either the detector on TAU or the receiver at Earth. If TAU remains in the plane of the ecliptic, direct sunlight will interfere with the both links when the earth is in occultation with the sun. However, the earth and sun will be in occultation only 0.5% of the time, and the sun's disk can be in TAU's detector field of view only if the spacecraft trajectory lies within about an arc second of the plane of the ecliptic.

Stray light, light received by the detector from off the optical axis of the receiver telescope, may be a problem when the solar disk lies near, but not in the detector field of view. A telescope's ability to reject off-axis light is strongly dependent on its particular design. Analyses of existing designs which may be similar to the TAU communications telescope will be useful in evaluating the importance of stray light in detail.

Light from discrete stars was not found to be a significant noise problem for stars dimmer than 7th magnitude. The irradiance of the star included in the optical link DCTs was calculated using a brightness temperature close to that of the sun; thus, the bolometric magnitude of this star is little different from its visual magnitude. With a 7th magnitude star in the detector's field of view, a link performance margin of over 2 dB was still possible. A margin of 3 dB or more was obtained in links with stars of 8th magnitude or dimmer.

The mean number density of stars brighter than magnitude 8.0 is 0.56 stars per square degree. The mean density is about 1.1 for low galactic latitudes (averaged over all galactic longitudes) [7]. It should not be difficult to avoid these brightest stars when choosing the exact trajectory for TAU.

The zodiacal light (or "zodi"), sunlight scattered from interplanetary matter in the solar system, was also found not to represent an important noise source. However, if TAU's trajectory lies in or near the plane of the ecliptic, the zodi will appear at or near its maximum brightness in the field of view of the downlink receiver whenever the receiver must be pointed toward the sun to receive signals from TAU. The zodi has therefore been included in the link noise calculations near its maximum brightness. A plot of the spatial distribution of the zodiacal light within the ecliptic is shown in Fig. 1 [8].

Background noise from integrated starlight (ISL) was not found to be a problem for the telemetry link, even when taken at its maximum brightness in the galactic plane. The approximate maximum brightness of the integrated starlight is indicated on the graph in Fig. 1 [9].

Zodi and ISL were not both included in the noise calculations because only the least likely trajectory for TAU would allow a large contribution from both sources. The plane of the ecliptic intersects the galactic plane at about 60° and the line of intersection of the two planes lies close to a vector from the sun to the center of the galaxy. Thus the only TAU trajectory along which both planes could be viewed is one toward or away from the galactic center. But the best trajectories for astrometry are those normal to a vector from the sun to the galactic center, and TAU will probably fly along one of these.

Cherenkov radiation resulting from the interaction of cosmic rays with TAU's receiving optics should produce only negligible noise in the receiver on TAU, since all internal components must be shielded from cosmic rays for other reasons, and the detector and optics will not be exposed. Only a few photons per second (or less) will reach the detector from cosmic ray interactions in the primary mirror of the receiver telescope.

In the uplink, the sunlit earth will always be in the field of view of TAU's detector. (The earth and GEO are only about 0.24 microrad apart as seen from 1000 AU and TAU's detector field of view is 1.3 microrad.) If TAU stays in the ecliptic, the received noise power from the sunlit earth will vary between zero and its maximum value (Earth at inferior conjunction), which was used in Table 3. If TAU stays in the galactic plane (60° out of the ecliptic) the noise will vary between 1/3 and 2/3 of its maximum.

The noise power given in Tables 2 and 3 should not be compared directly with the value of the average received signal power shown on the line above it. The signal power is concentrated in very short pulses whereas the background power is distributed randomly in time.

B. Optical Uplink

The system requirements for an optical command link for TAU are less stringent than those for a telemetry link, primarily because the required command data rate is less than 1 kbps and because mass and power budgets should allow a more powerful laser and a larger telescope for sending command data.

A DCT for a TAU optical uplink is shown in Table 3. The TAU spacecraft will use the same telescope for reception and transmission. Note that the same wavelength was used in these calculations as was used for the downlink, though this is not necessarily a requirement and may even be undesirable. The Earth orbiting communication station is assumed to transmit from a 1.5 meter telescope (diffraction limited) using a 16-watt laser. The efficiencies of the optics and the detector are assumed to be identical to those used in the downlink calculations, and the expected major noise sources are included at their maximum magnitudes.

This link assumes a PPM word size of 128, a bit error rate of 10^{-4}, and a command data rate of 500 bps. Reed–Solomon coding is assumed, with a coding fraction of 7/8; the adjusted data rate and error rate values are shown in the tables. The operational parameters were selected to give a performance margin of about 3 dB. Different parameters e.g., a larger word size, can provide a greater margin and would allow a less powerful laser or smaller transmitter aperture. A data rate of 500 bps is probably not necessary for transmission of command data to TAU; 32 bps has been given as a command data rate for Galileo [3]. Such a reduction in data rate would reduce considerably the command link parameter requirements.

C. Acquisition and Tracking

From 1000 AU the earth and sun are separated by 1 millirad (maximum) and TAU's communication telescope will have an angular limit of resolution of less than 1 microrad. However, an imaging detector (e.g., a CCD array) with a dynamic range of 90 dB or more would be required to image both objects simultaneously. The difference in brightness will be even greater when the sunlit earth is seen at less than its maximum brightness.

A more suitable beacon than the sunlit earth would be the uplink communication laser itself. The peak power received by the spacecraft from a 16-watt pulsed laser is greater than the received background power from the sun, even when the sun fills the detector's field of view behind the beacon. The laser energy received by TAU from a 16-watt laser operating with a duty cycle of 270×10^{-6} ("on" for 270 μsec each second) would be approximately equal to the solar background received through a narrow-band filter in the same time interval, about 3 picojoules. Much smaller duty cycles, and therefore higher peak powers, are easily attainable.

This calculation assumed a small nonimaging detector (as did the communications link calculations), but a CCD detector should be able to image both the laser beacon and the sun in the background through a neutral density filter.

IV. Conclusion

The TAU mission would provide an opportunity for a number of astronomical and space science experiments that could not be carried out inside the solar system. This study examined the problem of returning to Earth the data obtained by TAU and found a communications system based on optical frequencies to be more practical for the TAU mission than one based on radio frequencies. Although the technology for optical communications is still much less mature than radio frequency communications technology, an optical system can meet the requirements of TAU without any technological breakthroughs — the necessary development can be reasonably expected before the time TAU is to be launched.

References

[1] R. M. Dickinson, "A Comparison of 8.415-, 32.0-, and 565646-GHz Deep Space Telemetry Links," *JPL Publication 85-71*, Jet Propulsion Laboratory, Pasadena, CA, pp. 20, Oct. 15, 1985.

[2] L. D. Jaffe, et al., "An Interstellar Precursor Mission," *J. British Interplanetary Soc.*, vol. 33, pp. 3-26, 1980.

[3] J. H. Yuen, "Telecommunications Systems Design," *Deep Space Telecommunications Systems Engineering*, J. Yuen, ed., pp. 1-22. Plenum Press, NY, 1983.

[4] W. K. Marshall and B. D. Burk, "Received Optical Power Calculations for Optical Communications Link Performance Analysis," *TDA Progress Report 42-87*, vol. July-September 1986, Jet Propulsion Laboratory, Pasadena, CA, pp. 32-40, Nov. 15, 1986.

[5] D. L. Robinson and B. D. Metscher, B. D. "A Cooled Avalanche Photodiode with High Photon Detection Probability," *TDA Progress Report 42-87*, vol. July-September 1986, Jet Propulsion Laboratory, Pasadena, CA, pp. 41-47, Nov. 15, 1986.

[6] Hughes Aircraft Co., Final Report of A Study to Determine the Impact of Laser Communication Systems on Their Host Spacecraft, prepared for NASA Goddard Space Flight Center under Contract NAS 5-27139, April 1984, Section 9.

[7] C. W. Allen, *Astrophysical Quantities*, 3rd edition, The Athlone Press, University of London, p.243, 1981.

[8] C. Leinert, C. " Zodiacal Light — A Measure of the Interplanetary Environment," *Space Sci. Rev.* vol. 18, pp. 281-339, 1975.

[9] F. E. Roach and R. R. Megill, "Integrated Starlight Across the Sky," *Ap. J.*, vol. 133, p. 128, 1961.

[10] D. L. Sipes, "Nd:YAG End Pumped by Semiconductor Laser Arrays for Free Space Optical Communication," *IEEE Military Communications Conference*, Boston, MA, pp. 104-108, Oct. 20-23, 1985.

Table 1. TAU Ka-band telemetry link.

Wavelength (m) 0.009369 (32 GHz)
Range (AU, m) 1000   1.49e14

Transmitter		dB	Ref.
Antenna diameter, m	15		(1)
DC power, W, dBm	115	50.6	
DC-to-RF conv. efficiency	0.21	–6.8	(2)
RF output power, W, dBm	24.15	43.8	
Losses	0.548	–2.6	(2)
Gain, dB	1.385e7	71.4	
Space loss, 1000 AU	2.5e–35	–346.0	

Receiver			
Antenna diameter, m	200		
RF efficiency fraction, dB	0.871	–0.6	(2)
Mechanical and other efficiencies	0.769	–1.1	(2)
Antenna gain	3.009e9	94.8	
Noise spectral density, dBm/Hz		–185.0	(1)
Total received power, W, dBm	2.5e–17	–136.0	

Data channel			
Data rate, BPS, dB BPS	20000	43.0	
Bit error rate	0.0001	–40.0	(1)
Data power/total power		–0.01	(1)
Received data power		–136.0	
Threshold ST/No		3.0	(1)
Threshold data power		–139.0	(1)
Performance margin	1.99	3.0	

Table 2. Optical communications link analysis

		TAU Downlink	Factor	dB
Wavelength, micrometers	=	0.53200		
PPM Parameters (Coded)				
Alphabet size, M	=	1024.0		
Data rate, Kbits/sec	=	40.039		
Dead time, microseconds	=	239.52		
Slot width, nanoseconds	=	10.000		
Required link bit error rate	=	0.15000		
Laser output power, watts			10.0	40.0 dBm
Min Req'd peak power, watts	=	0.25E+06		
Transmitter antenna gain			0.247E+14	133.9
Antenna dia., meters	=	1.000		
Obscuration dia., meters	=	0.200		
Beam width, microrad	=	0.920		
Transmitter optics efficiency			0.650	–1.9
Transmitter pointing efficiency			0.946	–0.2
Bias error, microrad	=	0.050		
RMS jitter, microrad	=	0.050		
Space loss, 1000.00 AU			0.801E–43	–431.0
Atmospheric transmission factor			1.00	0.0
Receiver antenna gain			0.335E+16	155.2
Antenna dia., meters	=	10.000		
Obscuration dia., meters	=	2.000		
Field of view, microrad.	=	1.298		
Receiver optics efficiency			0.650	–1.9
Narrowband filter transmission			0.650	–1.9
Bandwidth, angstroms	=	10.000		
Received signal power, watts			0.172E–13	–107.6 dBm
Noise sources				
Zodi, radiance, W/m^2 Sr A	=	0.10000E-07		
8th mag. star irradiance, W/m^2 A	=	0.15000E-14		
Recv'd background power, watts	=	0.478E-12		

	TAU Downlink	Factor	dB
Detector Quantum efficiency		0.400	-4.0
Photons/joule		0.268E+19	154.3 dB/mJ
Detected signal PE/second		0.184E+05	42.7 dB/Hz
Symbol time, seconds		0.250E-03	-36.0 dB/Hz
Detected signal PE/symbol		4.61	6.6
Required signal PE/symbol		2.25	3.5
Detected background PE/slot	= 0.512E-02		
Margin		2.05	3.1

Table 3. Optical communications link analysis

	TAU Uplink	Factor	dB
Wavelength, micrometers	= 0.53200		
PPM parameters (coded)			
Alphabet size, M	= 128.00		
Data rate, Kbits/sec	= 0.57200		
Dead time, microseconds	= 12225.0		
Slot width, nanoseconds	= 100.00		
Required link bit error rate	= 0.12000E-01		
Laser output power, watts		16.0	42.0 dBm
Min Req'd peak power, watts	= 0.20E+07		
Transmitter antenna gain		0.556E+14	137.5
Antenna dia., meters	= 1.500		
Obscuration dia., meters	= 0.300		
Beam width, microrad	= 0.614		
Transmitter optics efficiency		0.650	-1.9
Transmitter pointing efficiency		0.885	-0.5
Bias error, microrad	= 0.050		
RMS jitter, microrad	= 0.050		
Space loss, 1000.00 AU		0.801E-43	-431.0
Atmospheric transmission factor		1.00	0.0
Receiver antenna gain		0.335E+14	135.2
Antenna dia., meters	= 1.000		
Obscuration dia., meters	= 0.200		
Field of view, microrad.	= 1.298		
Receiver optics efficiency		0.650	-1.9

Table 3. (contd)

|	TAU Uplink	Factor	dB
Narrowband filter transmission		0.650	–1.9
Bandwidth, angstroms	= 10.000		
Received signal power, watts		0.580E-15	–122.4 dBm
Noise sources			
Sunlit Earth at 1000 AU			
Zodi, radiance, W/m^2 Sr A	= 0.10000E-07		
8th mag. star, irradiance, W/m^2 A	= 0.15000E-14		
Recv'd background power, watts	= 0.510E-14		
Detector Quantum efficiency		0.400	–4.0
Photons/joule		0.268E+19	154.3 dB/mJ
Detected signal PE/second		621.0	27.9 dB/Hz
Symbol time, seconds		0.122E–01	–19.1 dB/Hz
Detected signal PE/symbol		7.60	8.8
Required signal PE/symbol		3.85	5.9
Detected background PE/slot	= 0.546E–03		
Margin		1.97	3.0
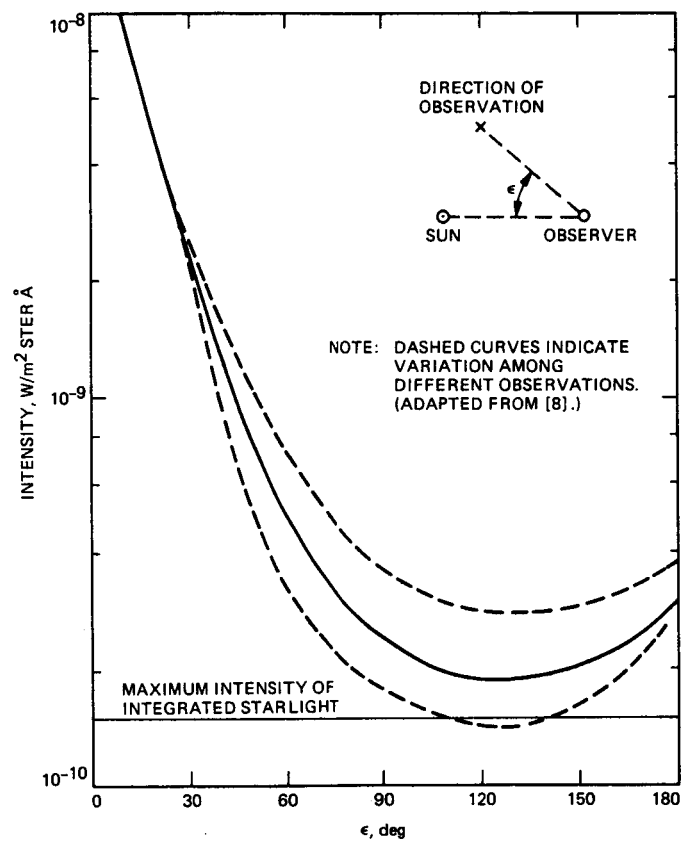
Fig. 1. Intensity of the zodiacal light in the ecliptic